Quantum Tuning of Plasmons in Ultrathin Metal Films

A Dissertation Presented for the

Doctor of Philosophy

Degree

The University of Tennessee, Knoxville

Ao Teng

August 2014

© by Ao Teng, 2014
All Rights Reserved.

To my family and friends

Acknowledgements

First, I would like to express my sincere gratitude to my advisor, Professor Hanno Weitering, who guided me through all the ups and downs of research. He always kept the door open to students, even after he took the role of department head. I especially respect his insistence of the traditional values in scientific culture.

I am very grateful to Dr. Mustafa Özer and Dr. Paul Snijders. They spent a lot of effort to help me "grow up"over the years and my indebtedness to them is beyond words.

Special thanks go to Prof. Geunseop Lee for sharing his knowledge and expertise on electron energy loss spectroscopy (EELS).

I would like to express my appreciation to our theoretical collaborators: Prof. Krzysztof Kempa, Prof. Adolfo Eguiluz, Dr. Xiaoguang Li, and Mr. Robert Van Wesep, for their insights and advice.

Last but not the least, my gratitude extends to current and former group members: Prof. Norman Mannella, Dr. Paolo Vilmercati, Dr. Violeta Iancu, Dr. Eun Ju Moon, Dr. Daniel Mulugeta, Dr. Christine Cheney, Dr. Fangfei Ming, Mr. Randal McMillan, Mr. Saban Hus, Mr. Hao Hu, Mr. Xiangshi Yin, Mr. Michael McConnell, Mr. Weisong Tu, Mr. Nicholas Sirica, Ms. Xiaoqian Hu, and Mr. Shuaicheng Lu.

"Deus sive Natura"— Baruch Spinoza

Abstract

The surface plasmon is a coherent charge density oscillation localized at a metal surface. It can couple with light and the resulting plasmon-polariton hybrid mode is confined to volumes that are much smaller than the classical diffraction limit of light. Nano-plasmonics is a rapidly evolving field where light manipulation at the nanoscale may lead to novel applications. However, as the size of plasmonic devices approaches the quantum-size regime, the macroscopic picture of plasmon may no longer be valid. To elucidate the influence of the discretization of the single particle spectrum on the collective plasmon response, we performed a systematic study of plasmons in ultrathin metal films, using reflection electron energy loss spectroscopy (REELS). We selected two metal systems, Mg(0001) and Pb(111), grown epitaxially on Si(111) and Ge(111) substrates, respectively. The plasmon response of bulk Mg can be captured within jellium theory, while that of bulk Pb is dominated by band structure effects. Surprisingly, the plasmon response of a 4.5 monolayer (ML) thick epitaxial Mg(0001) film on Si(111)-(7 $\times$ 7) already resembles that of the semi-infinite jellium model. However, we unveil a direct correlation between the thickness-dependent oscillatory charge spilling of the quantum well states and the linear dispersion coefficient of the monopole surface plasmon. In addition, the spectral intensities of photoemission threshold excitation and multipole surface plasmon follow a similar quantum oscillatory pattern. These results are attributed to the quantum size effects on the surface charge density profile. The 2 eV excitation associated with an interband transition in bulk Pb redshifts to 0.3 eV in ultrathin films. This

excitation is attributed to the symmetric surface plasmon branch, which is rarely seen in metallic films. Its appearance may be related to the perfect interfaces in our studies, in conjunction with the quasi one-dimensional nature of the screening response in Pb(111) films. Both the multipole mode in Mg films and the interface mode in Pb films are highly relevant for plasmonics. The fundamental insight gleaned from these studies may thus have practical relevance as nano-plasmonic feature sizes enter the realm of quantum size physics.

Table of Contents

1 Background and Scope **1**

1.1 Plasmons and plasmonics 1

1.2 Non-local dielectric response 4

1.3 Ultrathin metals films and the quantum size effect 5

1.4 Context and scope of the thesis 9

1.5 Outline of the thesis 10

2 Theory of Collective Plasmon Excitations **12**

2.1 Classical picture and hydrodynamic model 13

2.1.1 The plasmon condition from Maxwell's equations 13

2.1.2 Local dielectric function: Drude-Lorentz model 16

2.1.3 Non-local effects: hydrodynamic model 18

2.1.4 Plasmons in thin films 20

2.2 Density functional theory: jellium model 22

2.2.1 Ground state properties 23

2.2.2 Time-dependent response properties 27

2.2.3 d-function formalism 29

2.2.4 Plasmons in thin films 31

2.3 Density functional theory: beyond the jellium model 35

2.3.1 Ground-state properties 36

2.3.2 Time-dependent response properties 39

2.3.3 Plasmons in thin films 41
2.4 Inelastic electron scattering 41

3 Experimental Techniques **45**
3.1 Ultrahigh vacuum system 45
3.2 Low energy electron diffraction and Auger electron spectroscopy . . . 49
3.3 Deposition rate calibration with Auger electron spectroscopy 53
3.4 High resolution electron energy loss spectroscopy 57

4 Quantum Oscillations in the Surface Excitations of Ultrathin Mg(0001) Films **59**
4.1 Experimental Procedures 60
4.2 Plasmon excitations in ultrathin Mg(0001) films 61
4.3 Phenomenological model 71
4.4 Conclusion 74

5 Plasmon Excitations in Ultrathin Pb(111) Films **76**
5.1 Plasmon excitations in bulk Pb(111) 77
5.2 Plasmon excitations in ultrathin Pb(111) films 80
5.3 Phenomenological model 81
5.4 Discussion and Conclusion 86

6 Outlook: Quantum Plasmonics **89**

Bibliography **92**

Vita **105**

List of Figures

1.1 Characteristic electron energy losses when a beam of fast electrons passes through a thin Mg foil [72]. Bulk plasmon losses are highlighted by blue circles, and surface plasmon losses are highlighted by red circles. 2

1.2 A plasmon is a self-sustained collective charge density oscillation. The Coulomb force acts as the restoring force. In the jellium model, the positive ions are approximated by uniform background charge. 3

1.3 Electric field and charge density oscillation associated with the surface plasmon [11]. (a) The longitudinal charge density oscillation at a metal-dielectric interface is the surface plasmon. (b) Exponential decay of the electric field amplitude. The normal component of the electric field is discontinuous and this gives rise to a sheet of charge localized at the metal surface. 3

1.4 Quantum size effect on the electronic structure and charge spillage of Mg films. (a) The charge spillage length is determined by the energy barrier between the highest occupied quantum well state and the vacuum level. When half the Fermi wavelength is commensurate with the lattice spacing, a quantum well state will be located at Fermi level. This gives rise to a maximum in charge spillage. For Mg films, the period is about 8 ML. (b) The energy levels of subbands. (To simplify, the work function is assumed to be the same for different film thickness. Thickness dependent work function for Mg films has been calculated, see [92]) 6

2.1 Dielectric function of Drude-Lorentz model. It can be viewed as the sum of intraband (Drude) and interband (Lorentz) contributions. See Equations (2.15) and (2.19). 16

2.2 Bennett[10] calculated the plasmon dispersions (left panel) for non-abrupt electronic density profile (right panel). The numbers on the curves in the left panel correspond to the values of $a(\AA)$ in the right panel. The points and error bars are from experimental result [45]. Note the mode between bulk plasmon and ordinary surface plasmon originates from the diffuseness of the surface charge density profile. It's called multipole surface plasmon due to its dipole-like distribution of the induced charge density. 18

2.3 (a) The "breathing"(or symmetric) and "sloshing"(or antisymmetric) plasmon modes are split for small $q_{\parallel}$, which is due to the coupling between the top and bottom interfaces of the free standing slab. (b) The coupling between surface and interface plasmon modes is affected by the dielectric substrate. The symmetric and antisymmetric modes do not merge at surface plasmon energy. Instead, the symmetric mode saturates at interface plasmon energy. 21

2.4 The ground state electronic charge density profiles near the jellium edge for different r_s values [47]. Distances are in atomic units. Electronic charge densities are normalized to the bulk values. 25

2.5 (a) The relationship between induced charge centroid and negative initial dispersion of surface plasmon. Surface plasmon energy is a function of average electronic density that "feels"the induced potential φ. When the centroid of induced charge density is located outside the jellium edge, the average electronic density $n_{av} = \int dz n(z)\varphi(z) / \int dz \varphi(z)$ which "feels"the induced potential decreases if the wavelength of induced potential decreases (from φ to φ'), thus gives rise to the negative initial dispersion coefficient for surface plasmon in jellium system [89]. (b) The real (left) and imaginary (right) components of d-function for different r_s [54] 30

2.6 Calculated surface response of (a) a thinner jellium slab ($L = 0.5\lambda_F$) and (b) a thicker jellium slab ($L = 5\lambda_F$) with $r_s = 3$ [101]. The results are qualitatively consistent with classical model except the negative initial dispersion of the surface plasmon (due to the non-local effect) and the extra features in the energy range of 7-8 eV (due to the interaction between the multipole plasmon and antisymmetric mode). Note most of the spectral weight is on the symmetric mode. 32

2.7 Induced charge density at the frequencies of the symmetric and antisymmetric plasmon modes. Dashed lines indicate the jellium edges [101]. 33

2.8 The surface response functions for free-standing and substrate-supported jellium films [102]. The symmetric mode is strongly damped in the presence of a dielectric substrate. 35

2.9 Illustration of the pseudopotential construction [80]. 37

2.10 Illustration of the partitioning in LAPW method. The unit cell is divided into atomic spheres and interstitial region. 38

2.11 Illustration of the inelastic scattering process: loss after (left top) or before (left bottom) elastic scattering. Wave vector diagram for incident and scattered electrons is shown on the right. [54] 42

3.1 Schematic diagram of the UHV chamber. 46
3.2 Schematic diagram of 4-grid LEED-AES optics (produced by the Surface Science Laboratory at Universidad Autónoma de Madrid). . . 49
3.3 Theoretical and experimental values of the inelastic mean free path as a function of electron's kinetic energy. [56] 50
3.4 Schematic diagram of Auger transition process. 51
3.5 Direct Auger spectrum (upper panel) and differential Auger spectrum (lower panel). 52
3.6 (a) Attenuation of the differential Si LVV Auger spectra as a function of deposition time. (b) Characteristic linear segment plot used to determine the Mg deposition rate. 53
3.7 The surface reconstruction of Pb on Ge(111) substrate at 4/3 ML coverage [84]. Note in the lower unit cell, there are 4 Pb atoms in the overlayer *vs.* 3 Ge atoms in the substrate. The surface atomic density of Pb(111) is about 4/3 times of Ge(111). 55
3.8 (a)Intensification of Pb Auger NOO signal at 94 eV. (b) The "kink"that marks the completion of first monolayer. 56
3.9 Schematic diagram of the HREEL spectrometer with double-pass 127° monochromator and kinetic energy analyzer. 56

4.1 (a) LEED pattern and (b) STM image of a 6 ML Mg film after annealing to 200 K. 60
4.2 Spectra of (a) 4.5 ML, (b) 7.5 ML and (c) 12 ML Mg films before (black circle) and after (red circle) linear background subtraction. Incident/scattering angle is represented by "θ_{in}/θ_{sc}". 62

4.3 (a) EEL spectra of a nominally 4.5 ML thick Mg film at different scattering angles and 50° incident angle. The apparent broadening of the elastic tail at 50° scattering angle is due to the fact that the scattering is specular in this particular geometry. (b) Fitting of the 4.5 ML Mg film spectrum at one specific scattering angle (corresponding to $q_{\parallel} \approx 0$ for the surface plasmon), after subtraction of a linear background. Components TE, SP, MP and BP correspond to threshold excitation, monopole surface plasmon, multipole surface plasmon, and bulk plasmon, respectively. 63

4.4 Fitted spectra of 4.5 ML, 7.5 ML and 12 ML Mg films at $\theta_{in}/\theta_{sc} = 50°/62°$. 66

4.5 Loss energies of 4 components as a function of $q_{\parallel}$. 67

4.6 Dispersions of monopole surface plasmons in 4.5 ML, 7.5 ML and 12 ML Mg films. Dashed lines are the result of polynomial fitting. The initial dispersion slopes are indicated by solid lines. 67

4.7 Thickness dependence of (a) the real part of $d(\omega_s)$; (b) the multipole mode intensity; and (c) the threshold excitation intensity. The intensities of the spectra in (b) and (c) are normalized by the total loss intensity; (d) Photoemission intensity at E_F in normal emission, or DOS(E_F), from Ref. [1]; (e) DOS(E_F) and initial oxidation rate of ultrathin Mg(0001) films on W(110) from Ref. [3]; (f) Charge spilling parameter λ from first-principles calculations for Mg(0001) on W(110) [13]. 69

4.8 Surface plasmon linewidths as a function of $q_{\parallel}$ for Mg single crystal [82] (left panel) and films (right panel). 70

4.9 (a) Imaginary parts of calculated surface reflection coefficients for r_s=2 (green) and r_s=4 (red) with $q_{\|} = 0.12\mathring{A}^{-1}$ and $\gamma = 0.1\omega_p$. The TE and MP contributions, determined via a least-squares fit of the calculated loss spectra, are indicated by the dotted lines. Note the relative redshift of the SP peak for r_s=4, consistent with Figure 4.6; (b) Real and imaginary parts of surface dielectric d-functions for r_s=2 (green) and r_s=4 (red), adopted from [52]. Vertical lines mark the SP energy of bulk Mg, $\omega_s = \omega_p/\sqrt{2}$. 72

4.10 Quantum-size effects on collective plasmon excitations in ultrathin Mg(0001) films are related to the thickness-dependent charge spilling at ground state. 75

5.1 The HREEL spectra, dielectric functions and loss functions for thick Pb(111) films along Γ-K (upper panels) and Γ-M (lower panels) directions. Distinct energy loss features at 2, 7, and 10 eV are circled in red [unpublished, A. Teng, R. Van Wesep *et al.*]. The loss intensities recorded along the Γ-K and Γ-M direction are quite different. This is not captured by TDDFT calculations within the framework of LAPW. The middle panel shows two features near 2 eV and 8 eV in the imaginary part of the dielectric function. Those are "absorption bands"associated with interband transitions. Note the relatively strong intensity of the 2 eV excitation in EELS is not reproduced in the RPA response calculation. 78

5.2 The HREEL spectra of the 2 eV peak (left panel); The calculated band structure of bulk Pb(111) (right panel).[unpublished, A. Teng, R. Van Wesep *et al.*] The arrows mark the regions in momentum space where the energy separation between the initial and final state bands amounts to roughly 2 eV. 79

5.3 (a) Dispersion of the low energy excitation in 8 ML Pb(111) film; (b) Dispersion of the low energy excitation as a function of film thickness; (c) Survey spectrum of 8 ML Pb(111) film. The low energy (2 eV) excitation shifts to 0.3 eV and exhibits positive linear momentum dispersion for the 8 ML film. 81

5.4 Calculated dielectric functions for Pb bulk and 10 ML Pb film.[unpublished, A. Teng, R. Van Wesep *et al.*] There is no significant shift of absorption peak in 10 ML Pb film. 82

5.5 Dispersion of low energy excitations in 10 ML Pb(111) film along Γ-K direction. In the right panel, a new feature emerges at 4 eV and takes over the spectral weight at larger $q_{\|}$. 83

5.6 The dispersions of the low energy excitation almost collapse when plotted as a function of $q_{\|}L$. 84

5.7 Modeled spectra of the sandwich structure: (a) 0-20 eV scale; (b) 0-6 eV scale. Note the "anticrossing"when the slab plasmon (sharp peak on the low energy side of the spectrum) "walks"through the weak loss feature at 2 eV, its oscillator strength diminishes while its dispersion flattens, but the other (3 eV) peak takes over the spectral weight and acquires dispersion. 85

5.8 Comparison between REELS data (left panel) and the phenomenological model (right panel). The scattered data points are generated from the phenomenological model of the vacuum-metal-dielectric structure. The solid lines represent the classical symmetric and antisymmetric modes of a free standing film. The "gap opening"is due to the presence of a semiconductor substrate. 86

5.9 Plasmon responses of Pb(111) films are strongly affected by the interband excitations. This energy shift of the low energy excitation is attributed to the strong coupling between the two interface plasmons. 88

Chapter 1

Background and Scope

1.1 Plasmons and plasmonics

In the Universe, more than 99% of the observable mass is present in the form of an ionized gas, or plasma. Plasma-related phenomena, such as lightning and Polar Aurora, were observed and recorded long ago. It was not until the 1920s that Tonks and Langmuir introduced the concept of plasma oscillations to analyze these discharge phenomena [87]. Pines *et al.* [67] pointed out that the long range part of the Coulomb interactions between valence electrons in a metal gives rise to self-organized oscillations of the entire electron system. These plasma oscillations gain or lose energy in the form of discrete energy quanta, and the corresponding quasi particle is referred to as the bulk "plasmon". For simple metals, such as the alkali and alkaline-earth metals, the plasmon energy scales with the square root of the electron density [43].

Ritchie [77] studied the impact of film boundaries on the plasmon oscillations of a metal and predicted the existence of the surface plasmon, a charge fluctuation with greatly enhanced amplitude at the surface or interface boundaries. The surface plasmon energy is lower than the bulk plasmon energy by roughly a factor of $\sqrt{2}$ for nearly free electron metals. Both the bulk and surface plasmon modes show up as characteristic energy losses when a beam of fast electrons ($\sim keV$) passes through

a thin metal foil, as shown in Figure 1.1. For a thin magnesium film, these losses are of the order of 10 eV (10.6 eV and 7.1 eV, respectively). Higher order replicas correspond to the excitation of multiple quanta and clearly confirm the bosonic nature of the plasmon quasi particle. A simple picture of a plasmon oscillation is as follows [43]. When the electron cloud in a metal becomes polarized relative to the positive ionic background, then the resulting Coulomb force will act as the restoring force, much like Hooke's law in a mass-spring system (see Figure 1.2). The Coulomb force is what makes the system oscillate. The natural frequency of this harmonic oscillator system is the plasmon frequency. Plasmons may decay into electron hole pairs, due to *e.g.* impurity scattering and/or Landau damping, as will be discussed later. We

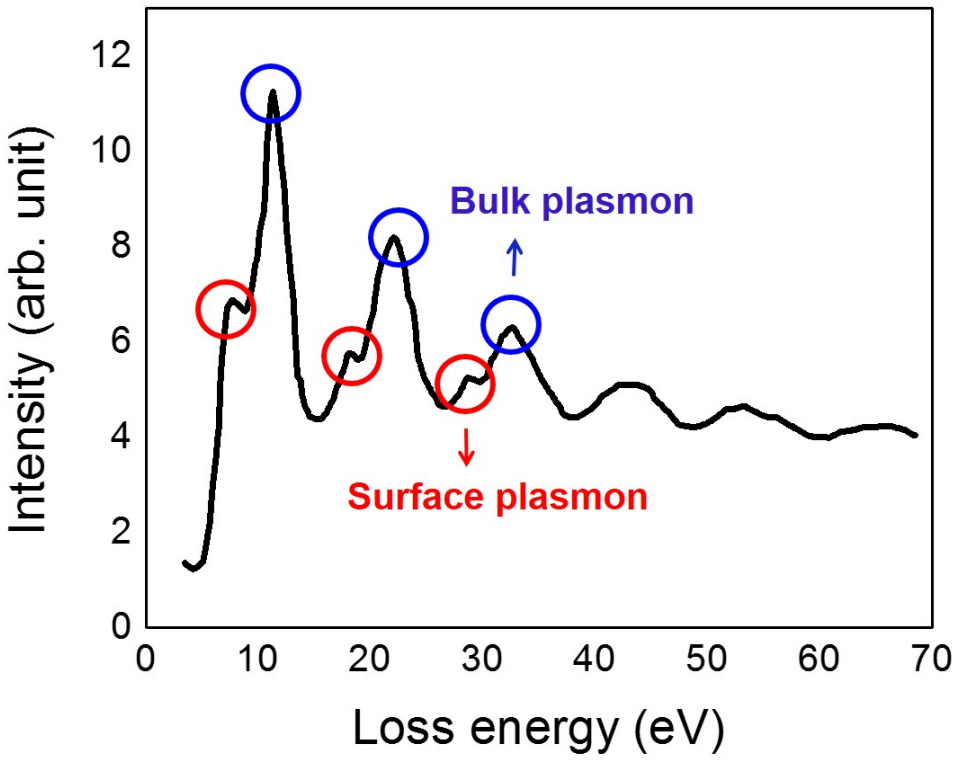


Figure 1.1: Characteristic electron energy losses when a beam of fast electrons passes through a thin Mg foil [72]. Bulk plasmon losses are highlighted by blue circles, and surface plasmon losses are highlighted by red circles.

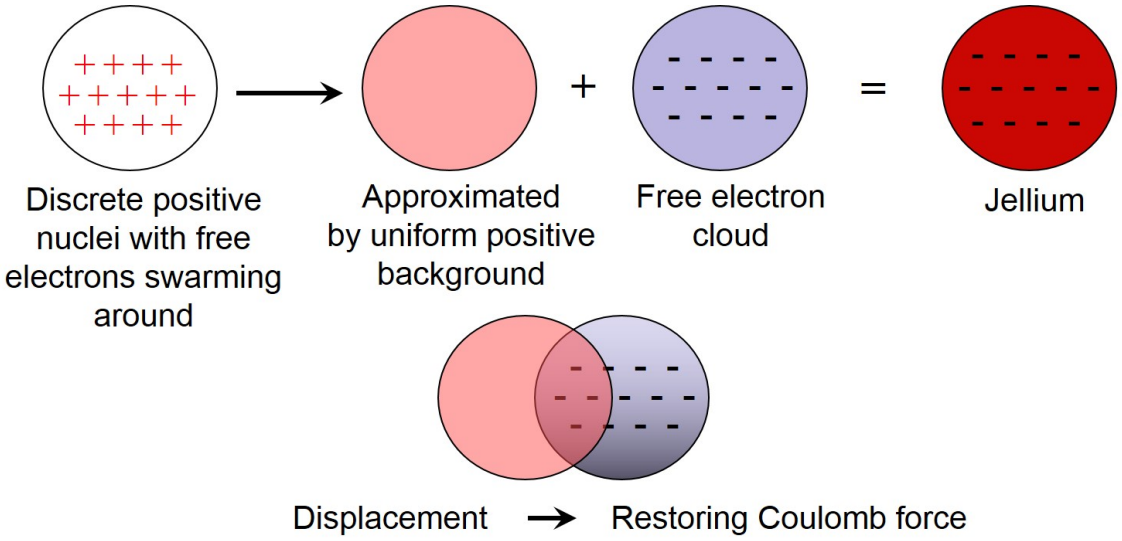
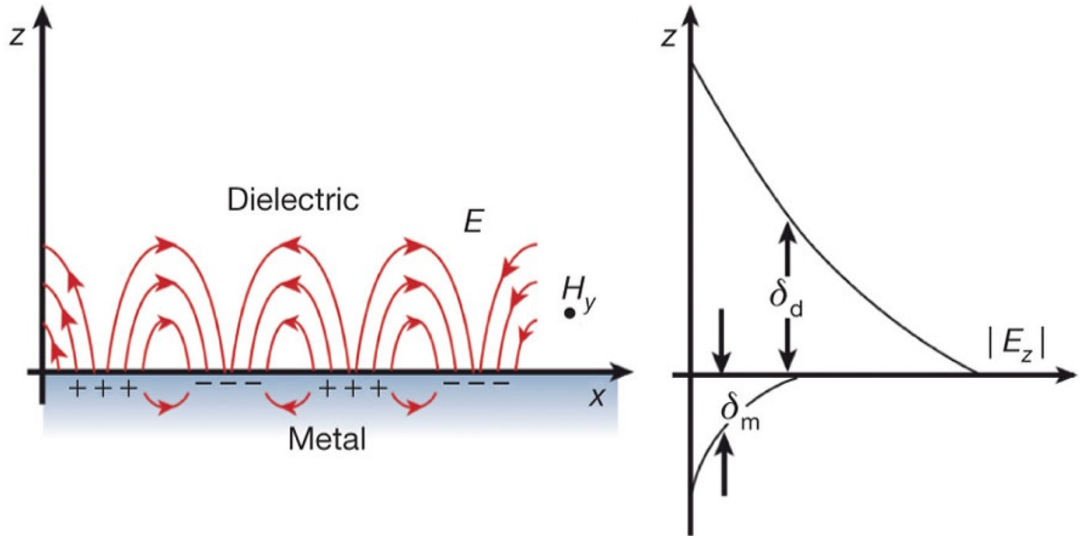


Figure 1.2: A plasmon is a self-sustained collective charge density oscillation. The Coulomb force acts as the restoring force. In the jellium model, the positive ions are approximated by uniform background charge.



(a) **(b)**

Figure 1.3: Electric field and charge density oscillation associated with the surface plasmon [11]. (a) The longitudinal charge density oscillation at a metal-dielectric interface is the surface plasmon. (b) Exponential decay of the electric field amplitude. The normal component of the electric field is discontinuous and this gives rise to a sheet of charge localized at the metal surface.

will also show that the oscillations need not be induced by an external perturbation. Instead, they can be self-induced when the dielectric constant becomes zero at the plasmon frequency. The latter implies that the corresponding charge fluctuations are longitudinal oscillations. A surface plasmon is a longitudinal charge density oscillation at the metal-vacuum interface which propagates like ripples in a pond. The associated electric field decays exponentially away from the surface (Figure 1.3). Because of a momentum mismatch, the surface plasmon cannot couple with light. Photons in free space simply do not carry enough momentum to excite a surface plasmon wave. However, this problem can be overcome by using a prism, grating coupler, or other surface structures which can impart the necessary momentum [74, 75]. The resulting hybrid excitation, or plasmon-photon coupled state, is called a surface plasmon-polariton. Because the resulting electromagnetic wavefields are strongly confined to the surface region, surface plasmons offer a unique avenue for deep subwavelength manipulation of light propagation in nanostructured materials. Indeed, "nano-plasmonics" bridges optics and electronics and may facilitate compact and ultrafast information processing [59]. Moreover, surface plasmons can serve as the basis for subwavelength waveguide design and other applications in nanotechnology such as solar energy harvesting and biomedical imaging [14].

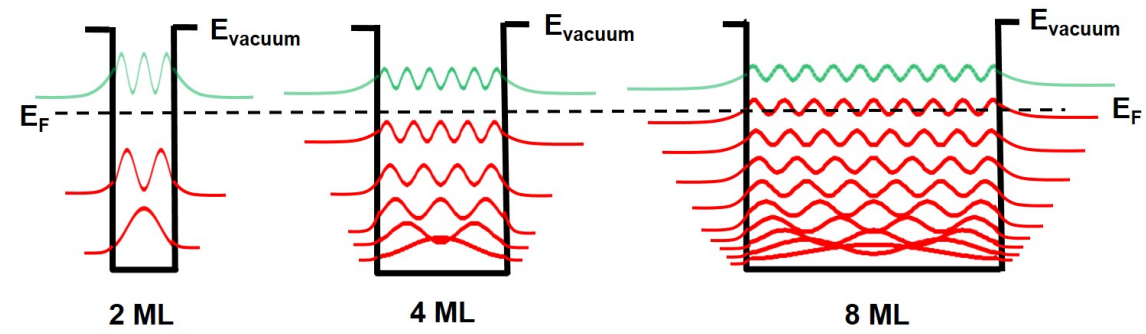
1.2 Non-local dielectric response

The plasmonic response of a metal is contained in the frequency dependent dielectric function ε which relates the potential inside the metal to the externally applied potential [8]. In the classical Drude theory of metals, ε is assumed to be spatially uniform and the surface plasmon frequency, as derived from the continuity equations of the Maxwell fields at the surface, only depends on the bulk electron density. However, a full quantum mechanical calculation is needed to adequately capture the non-local dielectric properties of an electronically diffuse surface or interface [24, 38]. Moreover, in strongly confined nanostructures such as ultrathin metallic

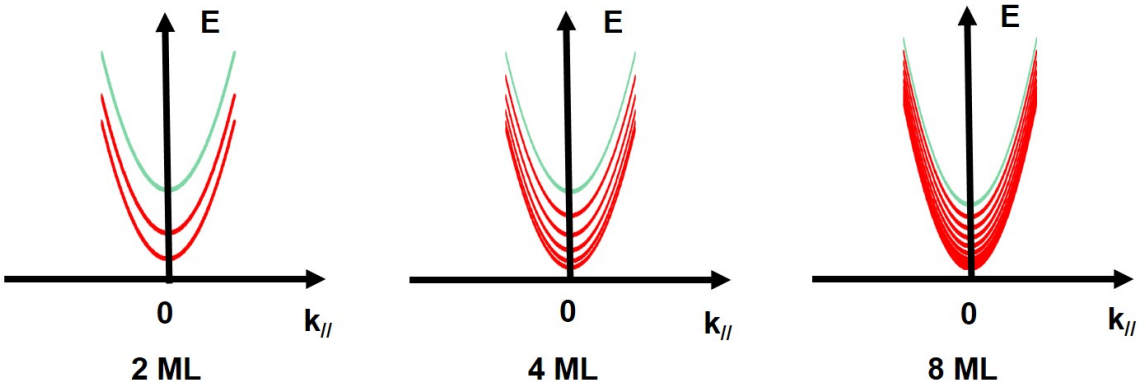
films, the quantization of the single particle spectrum into two-dimensional (2D) subbands is expected to produce a rich spectrum of collective excitations involving both intrasubband and intersubband plasmon modes. The former can be viewed as a 2D plasmon mode whose excitation energy depends on the areal electron density summed over all 2D subbands, while the latter represents a quantum mechanical hybrid of a single particle excitation between the subbands and the corresponding collective mode [94]. For increasing film thickness, one might expect the number of intersubband modes to increase, but their spectral weights should ultimately evolve towards the classical surface and bulk plasmon modes as the intersubband modes become increasingly collective in nature. The observation of the classical Mie resonance in ultrasmall *metallic* atom clusters [16] suggests that this crossover toward the bulk limit may happen very quickly, making it extremely difficult to elucidate quantum size effects in the plasmon response of metallic nanostructures. The goal of this thesis is to elucidate the role of quantum size effects on the collective plasmon response by means of EELS on atomically smooth metal films with thicknesses that can be controlled with atomic precision.

1.3 Ultrathin metals films and the quantum size effect

Plasmon-Photon coupling is normally realized in the retarded regime (near the light line). However, plasmon modes close to the light line usually suffer from heavy radiation losses and other loss mechanisms related to Landau damping and surface imperfections, thus resulting in short propagation lengths. It has been shown that the use of a very thin single crystal metal films on a dielectric substrate significantly extends the propagation length of surface plasmons, up to several centimeters in a 10 nm thick metal film [71]. Here, surface plasmons on both sides of the metal film strongly couple to one another which gives rise to a symmetric and an antisymmetric



(a)



(b)

Figure 1.4: Quantum size effect on the electronic structure and charge spillage of Mg films. (a) The charge spillage length is determined by the energy barrier between the highest occupied quantum well state and the vacuum level. When half the Fermi wavelength is commensurate with the lattice spacing, a quantum well state will be located at Fermi level. This gives rise to a maximum in charge spillage. For Mg films, the period is about 8 ML. (b) The energy levels of subbands. (To simplify, the work function is assumed to be the same for different film thickness. Thickness dependent work function for Mg films has been calculated, see [92])

field distributions (see Chapter 2). The symmetric mode turns out to be less lossy and thus has a longer propagation length [15]. Generally speaking, because of its almost linear dispersion up to high q-values *, frequency tuning is no longer limited to the retarded limit of the plasmon spectrum. Hence, transmission lines based on symmetric mode coupling are expected to have longer propagation ranges. Similarly, resonators would have larger quality factor, or Q-factor [94].

*$\hbar$q is the momentum of plasmon.

When plasmonic feature sizes approach the wavelength of the conduction electrons in a metal (typical Fermi wavelengths are of the order of sub-nanometer) quantum size effects become significant and cannot be neglected in the description of the dielectric response. Metal films consisting of several atomic layers (one atomic layer is about 0.3 nm thick) satisfy this condition. As the ground state electronic properties are strongly modified by the quantum size effect due to the discretization of the single particle spectrum, the excited state electronic properties and collective plasmon response are expected to be modified as well.

For an ultrathin metal film in the quantum size regime, the normal component of the electron momentum k_z is quantized according to

$$k_z = n * \pi / L, \tag{1.1}$$

where L is the film thickness and n is integer. The parallel momentum is continuous, and the single particle energy spectrum for nearly-free electrons is given by

$$E = E_n + \frac{\hbar^2(k_x^2 + k_y^2)}{2m^*}, \tag{1.2}$$

where m^* represents the effective mass of electron. The spectrum is discretized in a series of two-dimensional subbands where the subband minima correspond to the energy levels of a quantum particle confined to a one-dimensional potential well, as discussed in introductory level quantum mechanics textbooks. In particular, for symmetric finite square well,

$$V(z) = \begin{cases} -V_0, & |z| < L/2 \\ 0, & |z| > L/2 \end{cases}. \tag{1.3}$$

The wave functions of bound electrons ($-V_0 < E < 0$) assume the following form,

$$\Psi^E_{n,k_x,k_y}(x, y, z) \sim \phi_n(z) e^{i(k_x \cdot x + k_y \cdot y)}, \tag{1.4}$$

with

$$\phi_n(z) \sim \begin{cases} e^{-(\sqrt{-2m^*E_n}/\hbar)\cdot|z|}, & |z| > L/2 \\ \sin(\sqrt{2m(V_0+E_n)}\cdot z/\hbar) \ (odd\ parity) & \\ \quad or & |z| < L/2 \\ \cos(\sqrt{2m(V_0+E_n)}\cdot z/\hbar) \ (even\ parity) & \end{cases} . \tag{1.5}$$

Here, $E_n = -V_0 + \frac{\hbar^2\pi^2}{2m^*L^2}n^2$ $(n = 1, 2, 3, ...)$ is measured relative to the vacuum level. This situation is sketched in Figure 1.4 (to simplify, the work function is assumed to be the same for different film thickness; thickness dependent work functions for Mg have been calculated, see [92]). A direct inference of the quantum well model is that as the well width L increases, all the quantum well states "sink"deeper in energy. Also, additional quantum well states appear below the Fermi level. When the barriers are finite, the quantum well wavefunction penetrates into the vacuum region. The penetration length or wavefunction tails are largest for the highest occupied quantum level. In particular, the corresponding charge spillage is largest when the quantum well level appears at the Fermi energy. This happens when half the Fermi wave length and lattice spacing are commensurate,*i.e.*,

$$L = md = n * \lambda_F/2 \tag{1.6}$$

for integer values of m and n (d is monolayer thickness). In the case of Mg(0001) films, this happens every eight monolayers. Accordingly, one would expect to see quantum oscillations in the charge spilling length which, as we will see, have indeed been observed. In this thesis, we will demonstrate that the oscillatory charge spilling associated with the ground state electronic structure of the films also leads to a thickness-dependent oscillatory plasmon response, which, as we discussed, represents the collective excitations of the system. Note that if the metal layer is deposited on a semiconductor substrate, the confinement potential and boundary conditions are asymmetric. While the role of the substrate is difficult to discern in reflection EELS

experiments, which only probe the vacuum side, we have strong indications that the substrate heavily influences the plasmon response in ultrathin Pb films.

1.4 Context and scope of the thesis

Quantum confinement significantly affects the physical and chemical properties of nanoscale objects. In recent years, many studies have focused on the physical and chemical properties of ultrathin metal films, and the possibility of tuning these properties by varying the size and quantum-size boundary conditions. These include studies of the work function [63, 42], chemical reactivity [2, 57], thin film conductance [36], magnetic coupling [65], electron-phonon coupling [28], and superconductivity [28, 9]. Many of these properties exhibit quantum size effect oscillations. The quantum size effect may even dominate the thermodynamics and kinetics of thin film growth, and may lead to the existence of "magically stable"film thicknesses [81, 103, 30]. With the exception of magnetism and superconductivity, none of these phenomena are collective in nature, meaning that a mean field single particle picture, or band structure picture, is a good starting point for the theoretical analysis of these properties. In this thesis, we will focus entirely on the role of quantum confinement on the collective excitations.

We do note that similar studies in the literature focus almost exclusively on semiconductor heterostructures [97, 91, 49, 50]. However, the carrier density in these systems is very low and these electrons usually occupy very few subbands. The screening response of these systems is fundamentally different from the systems studied in this thesis, which have metallic densities and involve many occupied 2D subbands. Alternatively, many researchers have studied (sub)monolayer metal films on both metal [88, 53, 55] and semiconductor substrates [58, 34]. In the former case, the plasmon physics is still primarily dominated by that of the semi-infinite bulk, modified by an intriguing hybridization of the collective surface and bulk modes. The latter case deals with gapless two-dimensional or quasi one-dimensional

plasmon modes. Our work is different in that we explore the transition from the 2D quantum limit to the 3D bulk limit through atomic-scale control of the thickness and morphology of dense metallic films.

1.5 Outline of the thesis

The remainder of the thesis is organized as follows:

Chapter 2 provides a theoretical introduction of plasmon oscillations, starting with the classical Maxwell equations and ultimately referring to a full quantum mechanical treatment of the plasmon problem at the level of time-dependent density functional theory (TDDFT). This chapter concludes with a discussion of inelastic electron scattering in reflection electron energy loss spectroscopy (REELS). Chapter 3 introduces the experimental methods. Chapters 4 and 5 represent the core of the thesis and describe the plasmon response of quantum confined Mg(0001) films on Si(111) and Pb(111) films on Ge(111). The motivation for studying Mg is that bulk Mg closely resembles a jellium metal. Its plasmon response is well known [82], which provides an important benchmark for elucidating the role of quantum size effects on the plasmon response. Pb was chosen because Pb(111) is known to exhibit very strong quantum size effects in a variety of physical phenomena [95, 99, 17, 37], including superconductivity [60]. Here, it should be noted that very little is known about the plasmon response of bulk Pb in EELS experiments [96, 33]. Our study shows that Pb is very different from a jellium metal and that its collective response is dominated by band structure effects. While the results on Mg(0001) films highlight the importance of charge spillage and the corresponding quantum size effect oscillations of the plasmon response, the Pb results reveal very different features. Most importantly, they indicate the existence of a gapless slab plasmon. Normally, the slab plasmon is very difficult to observe in dense metallic systems, and we speculate that its appearance may be related to the perfect interfaces in our studies, in conjunction

with the quasi one-dimensional nature of the screening response in Pb(111) films [37]. The conclusions and outlook of our work will be summarized in the final Chapter 6.

Chapter 2

Theory of Collective Plasmon Excitations

There have been extensive theoretical studies of plasmon excitations in condensed matter systems, both classically and quantum mechanically. Classically, the existence of a plasmon, *i.e.*, the self-sustained charge density polarization wave, is an inference from Maxwell's equations, given the specific boundary conditions of the system. For longitudinal plasmons, this condition is met when the dielectric constant is zero. The simplest model for the local dielectric function (the local displacement current only depends on the local electric field) of a uniform electron gas is derived from the Drude model for a single electronic band. In a more sophisticated treatment, Lorentz oscillators are incorporated into the Drude model to account for interband transitions. Non-local effects, as well as the non-abrupt electron charge density profile at a metal surface, can be treated qualitatively within the classical hydrodynamic model. A more sophisticated quantum mechanical description starts with a calculation of the ground state electronic structure using density functional theory (DFT), and the subsequent calculation of the electronic excitations of the system using TDDFT. These quantum mechanical methods were initially applied to study plasmon excitations of a jellium metal. Nowadays, it is possible to calculate the dielectric response of real materials

from first principles, starting from an all-electron linearized augmented plane wave (LAPW) calculation of the ground state properties. This chapter provides an overview of the various theoretical methods used in this field of study. To make a connection with experiment, we will also discuss the role of the substrate on the plasmon modes in a thin film, and the various contributions to the scattering intensities in EELS.

2.1 Classical picture and hydrodynamic model

2.1.1 The plasmon condition from Maxwell's equations

The microscopic theory of electromagnetic wave-matter interaction is based on Maxwell's equations (for a non-magnetic system without external source)

$$\begin{aligned} \vec{\nabla} \cdot \vec{D} &= \rho, \\ \vec{\nabla} \cdot \vec{B} &= 0, \\ \vec{\nabla} \times \vec{E} &= -\frac{\partial \vec{B}}{\partial t}, \\ \vec{\nabla} \times \vec{H} &= \frac{\partial \vec{D}}{\partial t} + \vec{j}, \end{aligned} \tag{2.1}$$

where ρ is the total free electric charge density and $\vec{j}$ is the induced current density. For a uniform medium, $\rho = 0$, $\vec{j} = 0$. Furthermore, in vacuum,

$$\begin{aligned} \vec{D} &= \varepsilon_0 \vec{E}, \\ \vec{B} &= \mu_0 \vec{H}. \end{aligned} \tag{2.2}$$

Taking the time derivative of the third and fourth Maxwell equation in Equation 2.1, we obtain

$$\begin{aligned} \vec{\nabla}^2 \vec{E} - \mu_0 \varepsilon_0 \frac{\partial^2 \vec{E}}{\partial t^2} &= \vec{\nabla}^2 \vec{E} - \frac{1}{c^2} \frac{\partial^2 \vec{E}}{\partial t^2} = 0, \\ \vec{\nabla}^2 \vec{B} - \mu_0 \varepsilon_0 \frac{\partial^2 \vec{B}}{\partial t^2} &= \vec{\nabla}^2 \vec{B} - \frac{1}{c^2} \frac{\partial^2 \vec{B}}{\partial t^2} = 0. \end{aligned} \tag{2.3}$$

In linear dielectric materials,

$$\begin{aligned} \vec{D}(\omega) &= \varepsilon(\omega)\vec{E}(\omega), \\ \vec{B}(\omega) &= \mu(\omega)\vec{H}(\omega). \end{aligned} \tag{2.4}$$

Here, $\varepsilon(\omega)$ and $\mu(\omega)$ depend on frequency. Note that $\vec{D}(t) = \varepsilon\vec{E}(t)$ is generally incorrect, except when the electromagnetic wave is time-harmonic

$$\begin{aligned} \vec{E}(\vec{r},t) &= \vec{E}(\vec{r})e^{-i\omega t}, \\ \vec{B}(\vec{r},t) &= \vec{B}(\vec{r})e^{-i\omega t}. \end{aligned} \tag{2.5}$$

Note that even if the electromagnetic wave is not monochromatic, it can be decomposed into monochromatic waves through a Fourier series expansion. Defining $k = \omega\sqrt{\mu\varepsilon}$, the Maxwell's equations are reduced to

$$\begin{aligned} &\vec{\nabla}^2\vec{E} + k^2\vec{E} = 0, \\ &\vec{\nabla}\cdot\vec{E} = 0, \\ &\vec{B} = -\frac{i}{\omega}\vec{\nabla}\times\vec{E}, \end{aligned} \tag{2.6}$$

or equivalently,

$$\begin{aligned} &\vec{\nabla}^2\vec{B} + k^2\vec{B} = 0, \\ &\vec{\nabla}\cdot\vec{B} = 0, \\ &\vec{E} = \frac{i}{\omega\mu\varepsilon}\vec{\nabla}\times\vec{B}. \end{aligned} \tag{2.7}$$

A propagating wave in matter must satisfy

$$\vec{\nabla}\cdot\vec{D} = \varepsilon(\omega)\vec{k}\cdot\vec{E} = \rho = 0. \tag{2.8}$$

The solution yields either $\vec{k} \perp \vec{E}$ or $\varepsilon(\omega) = 0$. The two results correspond to transverse and longitudinal electric waves, respectively. For the transverse plasmon mode,

$$\omega = \frac{kc}{\sqrt{\varepsilon(\omega)}}. \tag{2.9}$$

The asympototic line of this curve represents the dispersion of light.

At the interface between different materials with dielectric constant ε_1 and ε_2, Maxwell's equations have to satisfy the boundary conditions

$$\begin{aligned} \hat{n} \times (\vec{E}_2 - \vec{E}_1) &= 0, \\ \hat{n} \times (\vec{H}_2 - \vec{H}_1) &= \vec{\alpha}, \\ \hat{n} \cdot (\vec{D}_2 - \vec{D}_1) &= \sigma, \\ \hat{n} \cdot (\vec{B}_2 - \vec{B}_1) &= 0, \end{aligned} \tag{2.10}$$

where $\hat{n}$ is the unit vector of surface normal, σ is surface free charge density and $\vec{\alpha}$ is surface induced current density.

The solutions can be classified into s-polarized (from "senkrecht", German for perpendicular) and p-polarized (from "parallel") electromagnetic modes, depending on whether $\vec{E}$ is perpendicular or parallel to the plane of incidence. For a surface charge density wave (*i.e.*, surface plasmon), there must be an $\vec{E}$ component perpendicular to the surface. Therefore, only p-polarized electromagnetic waves are allowed. The solution of Equation (2.10) is

$$\varepsilon_1 + \varepsilon_2 = 0. \tag{2.11}$$

If the interface is between metal (ε_1) and vacuum ($\varepsilon_2 = 1$), then the condition for surface plasmon is

$$\varepsilon_1 = -1. \tag{2.12}$$

2.1.2 Local dielectric function: Drude-Lorentz model

To explain electrical conduction in a metal, Drude [21] proposed a microscopic model in which "free electrons"are colliding with the much heavier positively charged ions. The interaction between electrons and ions is instantaneous. Long-range interactions between electrons and ions are neglected. The average time between electron-ion collisions is the time τ. The electron equation of motion under an external field E is

$$m\ddot{x} + \frac{m}{\tau}\dot{x} = eE, \tag{2.13}$$

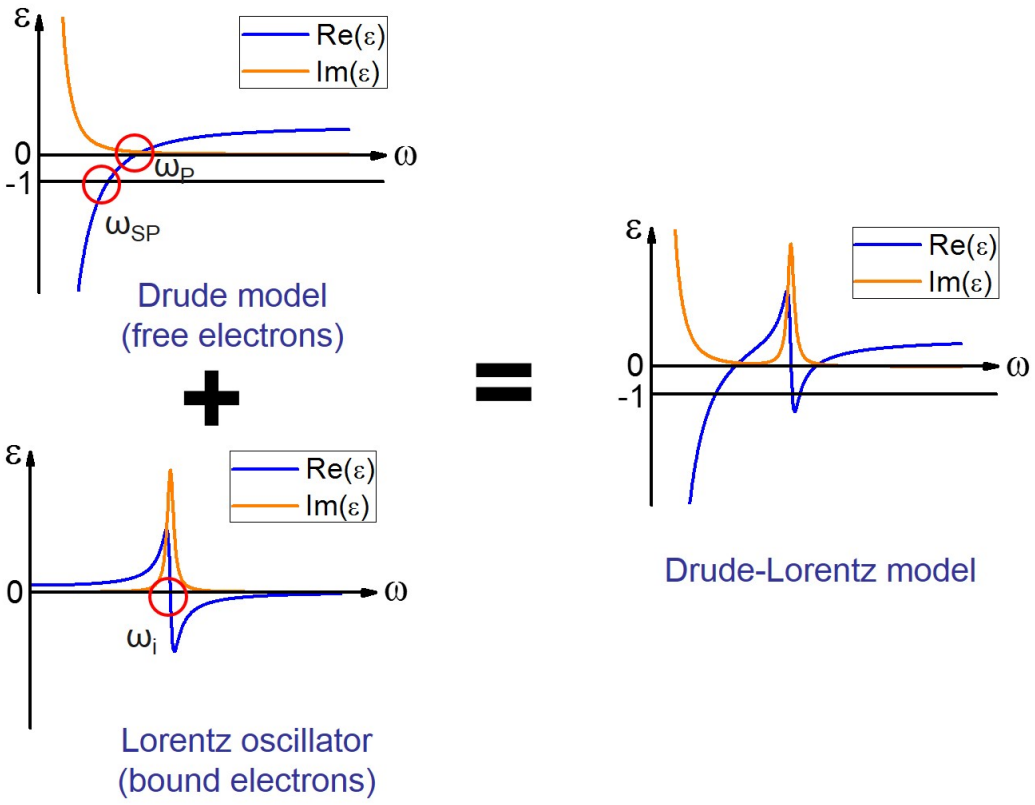


Figure 2.1: Dielectric function of Drude-Lorentz model. It can be viewed as the sum of intraband (Drude) and interband (Lorentz) contributions. See Equations (2.15) and (2.19).

where x is the electron's displacement from its equilibrium position. The second term represents friction. The total polarization density is defined as the sum of all electric dipole moments

$$P = (\varepsilon - 1)\varepsilon_0 E = enx, \tag{2.14}$$

where n is the electron density.

After inserting a time-harmonic electric field $E(t) = E_0 e^{-i\omega t}$, we arrive at the (complex) Drude dielectric function

$$\varepsilon(\omega) = 1 - \frac{\omega_p^2}{\omega^2 + i\omega\gamma}, \tag{2.15}$$

in which

$$\omega_p^2 = \frac{4\pi e^2 n}{m^* \varepsilon_0}. \tag{2.16}$$

γ is a measure of the damping and equals $1/\tau$, n is charge carrier density, and m^* is effective electron mass. The condition $\varepsilon(\omega) = 0$ and $\varepsilon(\omega) = -1$ yield the bulk and surface plasmon frequency, respectively

$$\begin{aligned} \omega &= \omega_p, \\ \omega &= \frac{\omega_p}{\sqrt{2}}. \end{aligned} \tag{2.17}$$

The extended Drude-Lorentz oscillator model includes electrons bound to the positive ion cores. A bound electron can be viewed as a classical oscillator with eigenfrequency ω_i. In quantum mechanics, the eigenfrequency corresponds to the transition energy between discrete levels (in atoms) or energy bands (*i.e.*, interband transitions in crystalline solids)

$$m\ddot{x} + \frac{m}{\tau}\dot{x} + m\omega_i^2 x = eE. \tag{2.18}$$

The corresponding complex local dielectric function is rewritten as

$$\varepsilon = 1 - \sum_i \frac{f_i(\omega^2 - \omega_i^2)}{(\omega^2 - \omega_i^2)^2 + \omega^2\gamma_i^2} + \imath \sum_i \frac{f_i\gamma_i\omega}{(\omega^2 - \omega_i^2)^2 + \omega^2\gamma_i^2}, \tag{2.19}$$

where f_i is the fraction of bound electrons with eigenfrequency ω_i. Figure 2.1 shows the real and imaginary parts of the Drude and Drude-Lorentz dielectric functions. The latter can be viewed as the sum of intraband (Drude) and interband (Lorentz) excitations.

2.1.3 Non-local effects: hydrodynamic model

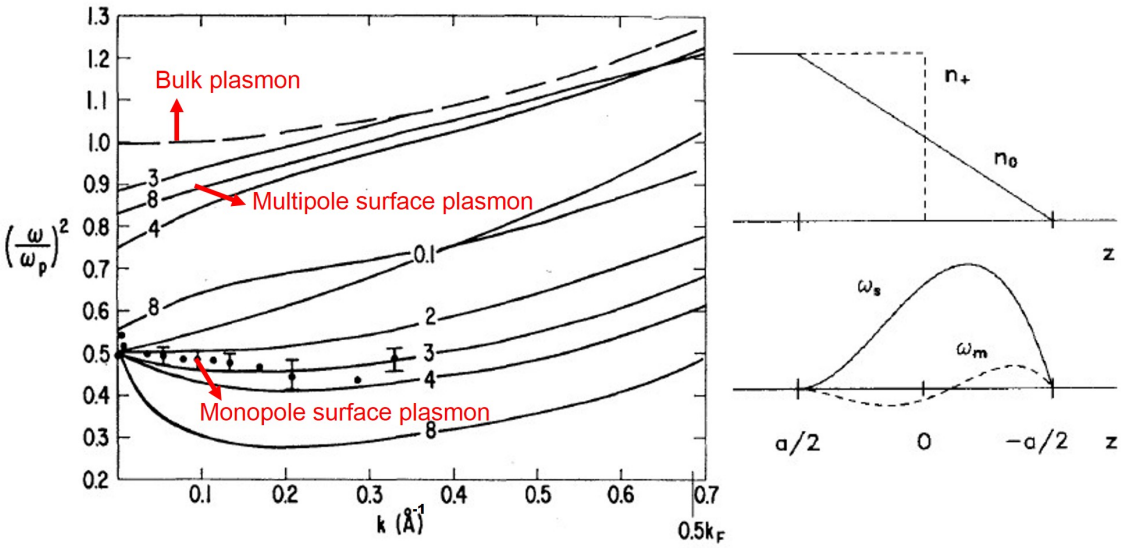


Figure 2.2: Bennett[10] calculated the plasmon dispersions (left panel) for non-abrupt electronic density profile (right panel). The numbers on the curves in the left panel correspond to the values of $a(\mathring{A})$ in the right panel. The points and error bars are from experimental result [45]. Note the mode between bulk plasmon and ordinary surface plasmon originates from the diffuseness of the surface charge density profile. It's called multipole surface plasmon due to its dipole-like distribution of the induced charge density.

The classical Drude-Lorentz model qualitatively describes the nature of both surface and bulk plasmons but it neglects several important features of the dynamical surface response. First, it is based on the local dielectric properties of the bulk. Secondly, it assumes an abrupt charge density profile at the surface. The momentum dispersion of the plasmon modes, which so far has been entirely overlooked, turns out

to be very important. Even though the frequency of the surface plasmon in the long-wavelength limit only depends on the bulk electron density (see Equations 2.16 and 2.17), its momentum dispersion is primarily determined by the electronic properties of the surface.

To address the first problem, a non-local extension of the Drude-Lorentz model is constructed by modeling the collective plasmon excitations as wave-like excitations of a hydrodynamic system, and incorporating the corresponding momentum dispersion, $\omega(\vec{q})$, into the bulk dielectric function. For the bulk plasmon, we have [43]

$$\omega^2 = \omega_p^2 + \beta^2 q^2, \tag{2.20}$$

where β represents the diffusibility or the propagation velocity of hydrodynamic disturbances in the system. Entering this formula into the Drude-Lorentz dielectric function and chosing $\varepsilon = -1$, we obtain the wave vector dependence (dispersion) of the surface plasmon frequency. However, this dispersion does not reflect the real surface electronic properties because the surface charge density oscillation intimately depends on the ground state charge density distribution near the surface, which deviates significantly from that of an abruptly truncated bulk density.

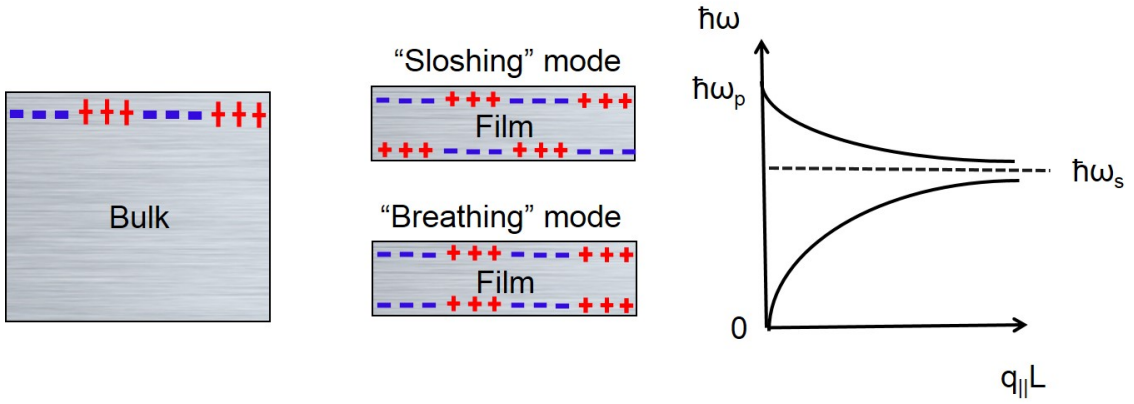
In order to address the second problem with the local model, Bennett [10] and Schwartz *et al.* [79] considered various non-abrupt charge density profiles and calculated the surface response within the hydrodynamic model. A simple physical interpretation for Bennett's result was explained by Eguiluz *et al.* [22]. It turns out that the ground state density profile has a great impact on the surface electronic excitations. In particular, two novel features emerged from Bennett's calculation: the surface plasmon exhibits negative dispersion in the long wavelength limit (in contradiction to the prediction based on the bulk dielectric function). In addition, a higher frequency surface mode, the so called multipole surface plasmon, appears (see Figure 2.2). The negative initial dispersion of the ordinary surface plasmon is due to the fact that the centroid of induced surface charge density is located outside

of the surface [89]. The existence of multipole plasmon is due to the softness and compressibility of electrons in the tail region [90]. The main difference between the ordinary surface plasmon and multipole plasmon is the profile of the induced charge density normal to the surface, as shown in Figure 2.2. The former mode has monopole character while the latter has a dipolar distribution. Both surface modes have a dipolar shape parallel to the surface.

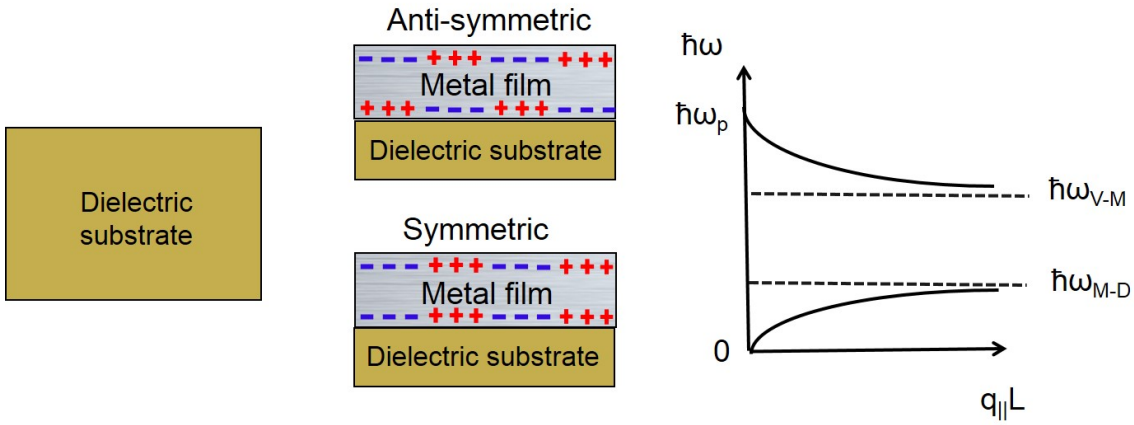
The hydrodynamic model successfully describes key features of the plasmon because the hydrodynamic system (*i.e.*, liquid) and electron gas have common characteristics. A major difference between an electron "liquid"and a real "metal"is compressibility. Electrons in a metal are not easily compressible not only because of Coulomb repulsion but also because of the Pauli exclusion principle. This effect is referred to as exchange-correlation. Electron tends to avoid each other and move as if they are screened by a "hole"[67]. The radius of the "hole"is called the Debye length (or Thomas-Fermi screening length) and its typical value for metal is a fraction of an $\mathring{A}$. Therefore, the exchange-correlation is a short-range electron-electron interaction. To properly address this issue, we need to go beyond hydrodynamics and use quantum mechanics.

2.1.4 Plasmons in thin films

The driving force of collective charge density oscillations (plasmons) is the long-range Coulomb interaction. In a slab geometry, surface plasmons at both interfaces can interfere with each other through this long-range Coulomb interaction. The coupling strength is determined by distance (*i.e.*, slab thickness) and plasmon wavelength. The latter is a measure of how fast the induced potential decays into the slab. For example, the strongest coupling happens in very thin films and in the long wavelength limit. According to the hydrodynamic model [77], the hybridized surface modes in



(a)



(b)

Figure 2.3: (a) The "breathing"(or symmetric) and "sloshing"(or antisymmetric) plasmon modes are split for small $q_{\|}$, which is due to the coupling between the top and bottom interfaces of the free standing slab. (b) The coupling between surface and interface plasmon modes is affected by the dielectric substrate. The symmetric and antisymmetric modes do not merge at surface plasmon energy. Instead, the symmetric mode saturates at interface plasmon energy.

thin films have the following dispersion relation for small q

$$\omega_{\pm} = \frac{\omega_p}{\sqrt{2}}(1 \pm e^{-qL})^{1/2}, \tag{2.21}$$

where L is the slab thickness. The value of the product qL is a measure of the coupling strength. The low-energy mode ω_- is called the "breathing mode"because the induced charge distribution is symmetric with respect to the slab's midplane; the high-energy

mode ω_+ is called the "sloshing mode"because the induced charge distribution is antisymmetric. In very thin slabs, the lower branch should be observable at short wavelengths. Figure 2.3a shows the hybridized plasmon modes in the free standing slab. In practice, thin films are deposited onto a substrate. The dielectric substrate has an impact on the coupling, see Figure 2.3b. Imagine a slab with dielectric function ε_1 sandwiched between materials with ε_0 and ε_2. The allowed p-polarized surface waves have to satisfy [74]

$$(\varepsilon_1 q_{z0} + \varepsilon_0 q_{z1})(\varepsilon_2 q_{z1} + \varepsilon_1 q_{z2}) + (\varepsilon_1 q_{z0} - \varepsilon_0 q_{z1})(\varepsilon_2 q_{z1} - \varepsilon_1 q_{z2}) e^{2iq_{z1}L} = 0, \tag{2.22}$$

where q_{zi} and $q_{\|}$ are the components of the wave vector $\sqrt{\varepsilon_i}\omega/c$, with

$$q_{\|}^2 + q_{zi}^2 = \varepsilon_i(\omega/c)^2. \tag{2.23}$$

Because the complex dielectric function ε_1 depends on ω, the plasmon dispersions $\omega(q)$ can be extracted from this local model.

2.2 Density functional theory: jellium model

* The surface dielectric response of a system depends on its ground state electronic structure, and particularly on the electronic charge density profile at the surface. Even though the classical and hydrodynamic results qualitatively match early experimental observations, the treatment of the ground state and excited state properties of the metal is oversimplified. Moreover, the coupling between the collective modes and electron-hole pair excitations in the metal is missing. As a suitable quantum mechanical successor, DFT, and its extension to TDDFT, have become the most common tools for calculating the ground state electronic structure and electronic

*Unless otherwise specified, the formulas in this section are adopted from Chapter 2 of "Electronic Excitations at Metal Surfaces", A. Liebsch, ISBN 0-306-45545-5, Plenum Press, New York 1997.

excitations of the system. The density functional theory, sometimes called an *"ab initio"* or "first-principles"method, starts with the Schrödinger equation.

2.2.1 Ground state properties

The cornerstone of density functional theory is the Hohenberg-Kohn theorem [29], which consists of two statements: first, the ground state properties of a many-electron system are uniquely determined by an electron density $n(\vec{r})$ that depends on only 3 spatial coordinates; secondly, giving the defined energy functional (below), the correct ground state electron density minimizes this energy functional

$$E[n] = T[n] + \int d^3r' n(\vec{r}) V_{ion}(\vec{r}) + \frac{1}{2}\int d^3r \int d^3r' \frac{n(\vec{r})n(\vec{r'})}{|\vec{r} - \vec{r'}|} + E_{xc}[n]. \tag{2.24}$$

The first term is the kinetic energy of a hypothetical non-interacting electron system that has the same electron density as the interacting system under consideration.

The second term represents the potential energy due to the Coulomb interaction between electrons and ions. The third term comes from the average electron-electron interaction. The last term is the exchange-correlation energy, which is due to the fact that the electrons avoid each other (because of Pauli principle and Coulomb repulsion). After "dumping"the many-body effects into the "black box"of exchange-correlation energy, $E_{xc}[n]$, a Schrödinger-like equation can be written for the system

$$[-\frac{1}{2}\nabla^2 + V_{eff}(\vec{r})]\psi_{\vec{k}}(\vec{r}) = \varepsilon_{\vec{k}}\psi_{\vec{k}}(\vec{r}), \tag{2.25}$$

$$V_{eff}(\vec{r}) = V_{ion}(\vec{r}) + \int d^3r' \frac{n(\vec{r'})}{|\vec{r} - \vec{r'}|} + V_{xc}(\vec{r}), \tag{2.26}$$

$$V_{xc}[n(\vec{r})] = \frac{\delta E_{xc}[n]}{\delta n(\vec{r})}. \tag{2.27}$$

Note functions $\psi_{\vec{k}}$ and energies $\varepsilon_{\vec{k}}$ are used as auxiliary parameters in order to construct the charge density.

The electron charge density is then given by

$$n(\vec{r}) = \sum_{\vec{k}} f_{\vec{k}} |\psi_{\vec{k}}(\vec{r})|^2, \tag{2.28}$$

in which $f_{\vec{k}}$ are Fermi-Dirac occupation factors. If the density varies slowly, $E_{xc}[n]$ can be expanded as

$$E_{xc}[n] = \int d^3r \left\{ \varepsilon_{xc}[n(\vec{r})] n(\vec{r}) + \varepsilon_{xc}^{(2)}[n(\vec{r})] |\nabla n(\vec{r})|^2 + ... \right\}, \tag{2.29}$$

where $\varepsilon_{xc}(n)$ is the average exchange-correlation energy per electron of a homogeneous electron gas. The second term is associated with the spatial gradient of the density. In the local density approximation (LDA), the second term is ignored (note in the generalized gradient approximation, or GGA, the gradient is kept). The exchange-correlation contribution to the effective potential is then given by

$$V_{xc}[n(\vec{r})] = \frac{\partial n \varepsilon_{xc}(n)}{\partial n}|_{n=n(\vec{r})}. \tag{2.30}$$

There are several approximations to the exchange-correlation energy for homogeneous electron gas. One of the simplest choices is the original Wigner formula (the Perdew-Zunger parametrization [66] is much more common)

$$\varepsilon_{xc}(n) = -\frac{0.458}{r_s(n)} - \frac{0.44}{r_s(n) + 7.8}, \tag{2.31}$$

where r_s is defined as the radius of a sphere containing one electron. r_s is determined by the density of the electron gas, *i.e.*

$$n = \frac{3}{4\pi r_s^3} = \frac{k_F^3}{3\pi^2}. \tag{2.32}$$

k_F is the Fermi wave vector. The exchange-correlation potential is then given by

$$V_{xc}(n) = -\frac{0.611}{r_s(n)} - \frac{0.587}{(r_s + 7.8)^2}(r_s + 5.85). \tag{2.33}$$

For simple metals, the ionic potentials are rather weak, and in the simplest treatment, the lattice of ionic charges is replaced by a positively charged uniform background. This is the jellium model. At the surface, the positive background charge is a simple step function. The ground state electronic charge density profile exhibits an exponential tail into the vacuum and damped Friedel oscillations towards the interior of the metal (see Figure 2.4). Friedel oscillations embody the static screening response

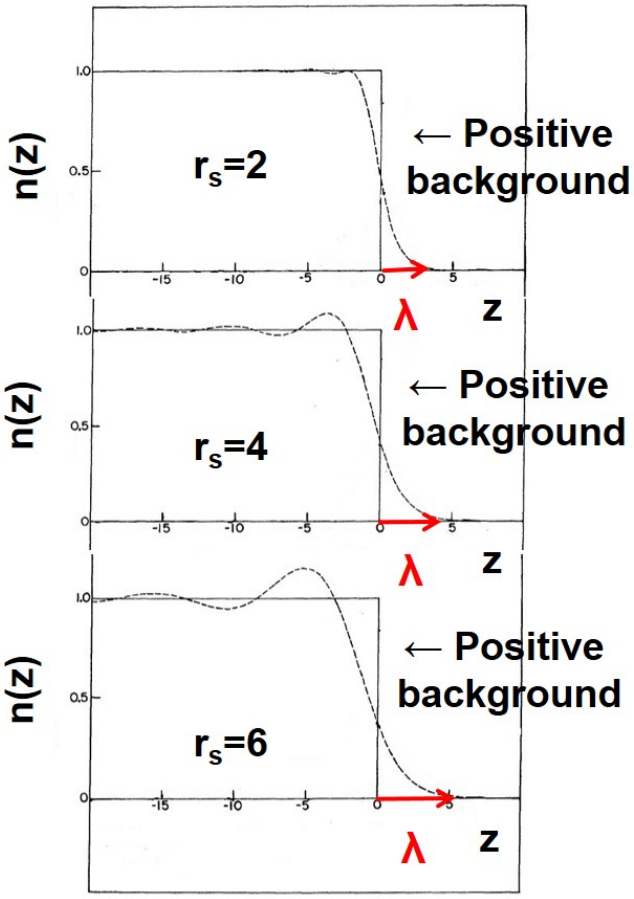


Figure 2.4: The ground state electronic charge density profiles near the jellium edge for different r_s values [47]. Distances are in atomic units. Electronic charge densities are normalized to the bulk values.

of a quantum mechanical system to the abrupt termination of the crystal potential at the surface. The period of these damped oscillations is determined by the Fermi wavelength. The charge density profile at surface is given by [47]

$$n(z) = \bar{n}[1 + \frac{a\cos(2k_F z + \alpha)}{z^2} + ...], \tag{2.34}$$

where the constants a and α are determined by the shape of surface potential. The location of the "surface"is [54]

$$z_{\|} = \int dz z \frac{d}{dz} n(z) / \int dz \frac{d}{dz} n(z) = \int dz [\frac{n(z)}{\bar{n}} - \theta(-z)]. \tag{2.35}$$

Now, the effective one-electron potential becomes

$$V_{eff}(z) = \phi(z) + V_{xc}(z). \tag{2.36}$$

The electrostatic potential ϕ satisfies the Poisson equation

$$\begin{aligned} \frac{d^2}{dz^2}\phi(z) &= -4\pi[n(z) - n_+(z)], \\ \phi(z) &= -2\pi \int_{-\infty}^{\infty} dz' |z - z'| [n(z') - n_+(z')]. \end{aligned} \tag{2.37}$$

Because of the finite energy barrier at surface, the effective potential decreases exponentially into the vacuum. The vacuum spilling of electrons gives rise to a dipolar charge distribution and leads to a difference in electrostatic potentials across the surface

$$D = \phi(\infty) - \phi(-\infty) = 4\pi \int_{-\infty}^{\infty} dz z [n(z) - n_+(z)]. \tag{2.38}$$

It can be proved that the dipolar potential barrier contributes to the work function

$$\Phi = D + |V_{xc}(-\infty)| - E_F. \tag{2.39}$$

The Fermi energy $E_F = 0.5k_F^2$ is measured with respect to the one-electron potential inside the metal.

2.2.2 Time-dependent response properties

The first Hohenberg-Kohn theorem can be extended to TDDFT, in which the electronic response to a time-dependent external potential is of interest. In an inelastic scattering experiment such as REELS, a weak external potential is produced by incident electrons far from the metal. The transition rate due to this perturbation can be calculated from Fermi's golden rule [†]

$$w(\omega) = 2\pi \sum_{\vec{k},\vec{k'}} f_{\vec{k}}(1 - f_{\vec{k'}})| < \vec{k'}|\phi_{ext}|\vec{k} > |^2 \delta(\varepsilon_{\vec{k'}} - \varepsilon_{\vec{k}} - \omega), \tag{2.40}$$

where $f_{\vec{k}}$ is the Fermi-Dirac distribution function. $\varepsilon_{\vec{k}}$ and $|\vec{k} > \leftrightarrow \psi_{\vec{k}}(\vec{r})$ are the LDA single particle energies and wave functions from ground-state calculation, respectively.

The surface electron density induced by external potential is given by

$$n_1(\vec{r}, \omega) = \int d^3r' \chi(\vec{r}, \vec{r'}, \omega)\phi_{ext}(\vec{r'}, \omega), \tag{2.41}$$

where χ is the linear many-body density-density response function. Alternatively, $n_1(\vec{r}, \omega)$ can be calculated from the self-consistent potential ϕ_{scf}

$$\begin{aligned} n_1(\vec{r}, \omega) &= \int d^3r' \chi_1(\vec{r}, \vec{r'}, \omega)\phi_{scf}(\vec{r'}, \omega), \\ \phi_{scf}(\vec{r}, \omega) &= \phi_{ext}(\vec{r}, \omega) + \phi_{ind}(\vec{r}, \omega). \end{aligned} \tag{2.42}$$

χ_1 is the independent-electron response function

$$\chi_1(\vec{r}, \vec{r'}, \omega) = \sum_{\vec{k},\vec{k'}} (f_{\vec{k}} - f_{\vec{k'}}) \frac{\psi^*_{\vec{k}}(\vec{r})\psi_{\vec{k}}(\vec{r'})\psi_{\vec{k'}}(\vec{r})\psi^*_{\vec{k'}}(\vec{r'})}{\omega + \varepsilon_{\vec{k}} - \varepsilon_{\vec{k'}} + i\delta}, \tag{2.43}$$

[†]Strictly speaking, the Fermi golden rule is relevant to linear response theory and does not belong in the discussion of TDDFT.

where δ is a positive infinitesimal. The main mission of TDDFT is to construct the effective potential $\phi_{scf}(\vec{r},\omega)$. The induced potential is a sum of electrostatic (Hartree) and exchange-correlation terms

$$\phi_{ind}(\vec{r},\omega) = \phi_{est}(\vec{r},\omega) + \phi_{xc}(\vec{r},\omega) \equiv \int d^3r' K(\vec{r},t,\vec{r'},t') n_1(\vec{r'},\omega), \tag{2.44}$$

where

$$\begin{aligned} K(\vec{r},t,\vec{r'},t') &= \frac{1}{|\vec{r}-\vec{r'}|} + \phi_{xc}(\vec{r},t,\vec{r'},t'), \\ \phi_{xc}(\vec{r},t,\vec{r'},t') &\equiv \frac{\delta V_{xc}(\vec{r},t)}{\delta n(\vec{r'},t')}. \end{aligned} \tag{2.45}$$

Using LDA and adiabatic approximations, ϕ_{xc} is approximated by Taylor expansion

$$\phi_{xc}(\vec{r},\omega) = \frac{\partial V_{xc}[n]}{\partial n}|_{n_0(\vec{r})} n_1(\vec{r},\omega). \tag{2.46}$$

In general, the exchange-correlation term reduces the strength of Coulomb interaction. TDLDA without exchange-correlation contribution in induced potential is equivalent to the random-phase-approximation (RPA).

With ϕ_{scf} being constructed, the transition rate is given by [54]

$$w(\omega) = -2\mathrm{Im}\int d^3r \int d^3r' \phi^*_{ext}(\vec{r},\omega)\chi_1(\vec{r},\vec{r'},\omega)\phi_{scf}(\vec{r'},\omega) = -2\mathrm{Im}\int d^3r \phi^*_{ext} n_1(\vec{r},\omega). \tag{2.47}$$

Therefore, the surface electronic excitation can be evaluated from the induced surface charge density. To fully describe the surface excitation spectra, assume the incident electron is far from metal and the external potential has to satisfy the Laplace equation, $\nabla^2\phi_{ext} = 0$. The solution is in the form of

$$\phi_{ext}(\vec{r},\omega) = -\frac{2\pi}{q} e^{i\vec{q_\parallel}\cdot\vec{r_\parallel}} e^{qz}. \tag{2.48}$$

The induced charge density is

$$n_1(\vec{r},\omega) = e^{i\vec{q_\parallel}\cdot\vec{r_\parallel}} n_1(z,q,\omega). \tag{2.49}$$

Plugging this into $w(\omega)$

$$w(q,\omega) = \frac{4\pi}{q}\mathrm{Im}\int dz e^{qz} n_1(z,q,\omega) = \frac{4\pi}{q}\mathrm{Im}g(q,\omega), \tag{2.50}$$

where $g(q,\omega)$ is the surface response function. The imaginary part, $\mathrm{Im}g(q,\omega)$, is called surface loss function. It is the quantity directly comparable to the inelastic electron scattering spectra. $g(q,\omega)$ determines the amplitude of the induced potential in the vacuum and it is equivalent to the reflection coefficient $r_p(q,\omega)$ of p-polarized light in the non-retarded optical limit ($\omega/c \ll q \ll 1$).

2.2.3 d-function formalism

The surface response function reveals the connection between the induced surface charge density and the optical reflection in the long wavelength limit. In an attempt to incorporate the quantum mechanical details of the surface into the classical Fresnel formulas, Feibelman [24] developed the d-function formalism. Here, the reflection coefficient of p-polarized light for a semi-infinite surface is

$$r(q_\parallel,\omega) = \frac{[\varepsilon(\omega)-1][1+q_\parallel d(\omega)]}{\varepsilon(\omega)+1-[\varepsilon(\omega)-1]q_\parallel d(\omega)}, \tag{2.51}$$

where

$$d(\omega) = \frac{\int dz z n_1(z,0,\omega)}{\int dz n_1(z,0,\omega)} \tag{2.52}$$

is a complex function which reflects the surface dielectric property. The real part of $d(\omega)$ is associated with the centroid of the charge density induced by uniform electronic field normal to the surface. The imaginary part of $d(\omega)$ represents the energy absorption at the surface. In the classical optical limit ($q_\parallel d = 0$), the reflection

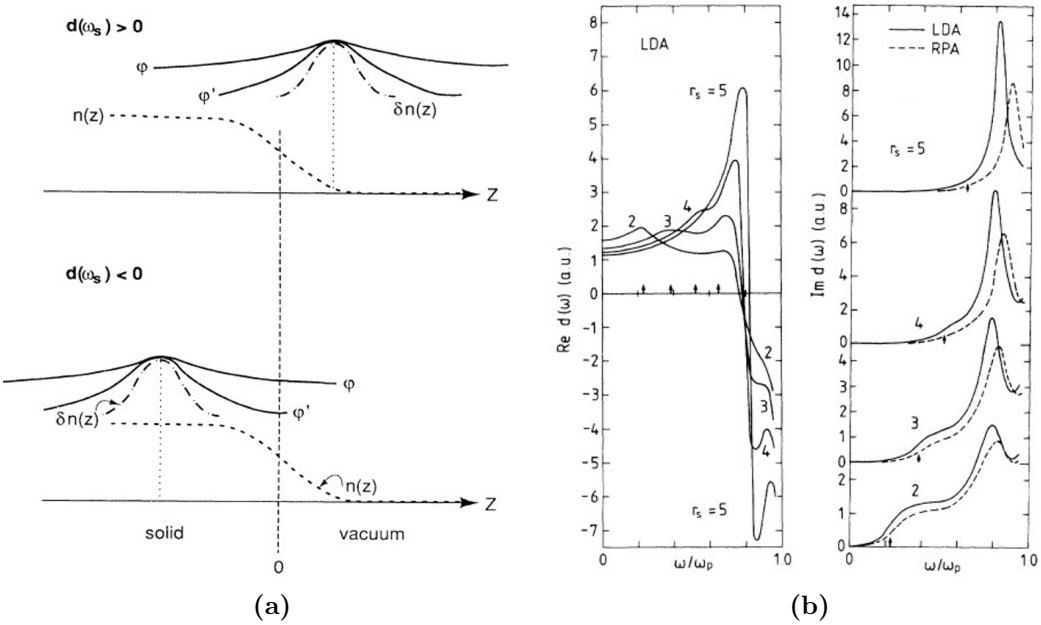
for p-polarized light is [25]

$$r(\omega) = \frac{\varepsilon(\omega) - 1}{\varepsilon(\omega) + 1}. \tag{2.53}$$

It has been shown that the real part of $d(\omega)$ determines the momentum dispersion of the surface plasmon energy at small $q_{\|}$ [89]

$$\omega_s(q_{\|}) = \omega_s[1 - \frac{q_{\|}}{2}\mathrm{Re}d(\omega_s) + ...]. \tag{2.54}$$

This was explained by Tsuei *et al.* [89] (see Figure 2.5a). The r_s dependent d-function based on jellium model is shown in Figure 2.5b.



(a) **(b)**

Figure 2.5: (a) The relationship between induced charge centroid and negative initial dispersion of surface plasmon. Surface plasmon energy is a function of average electronic density that "feels"the induced potential φ. When the centroid of induced charge density is located outside the jellium edge, the average electronic density $n_{av} = \int dzn(z)\varphi(z)/\int dz\varphi(z)$ which "feels"the induced potential decreases if the wavelength of induced potential decreases (from φ to φ'), thus gives rise to the negative initial dispersion coefficient for surface plasmon in jellium system [89]. (b) The real (left) and imaginary (right) components of d-function for different r_s [54]

.

2.2.4 Plasmons in thin films

[‡]The plasmon response of a thin jellium slab has recently been studied with TDDFT [101, 102, 5, 51]. The theoretical and computational procedures are similar to those of a semi-infinite jellium medium. However, the ground state electronic structure of the slab is different. The ionic charge distribution is given by

$$n_{ion} = \begin{cases} n_0, |z| \leqslant L/2, \\ 0, |z| > L/2. \end{cases} \tag{2.55}$$

Because of the translational symmetry parallel to a perfectly flat surface, the wavefunctions can be decomposed into two-dimensional plane waves for electron motion parallel to the surface and one-dimensional quantized states for motion in the perpendicular direction. The eigenenergies are a combination of the parallel and perpendicular kinetic energies

$$\begin{aligned} \Psi_{n,\vec{k_\parallel}} &= e^{i\vec{k_\parallel}\cdot\vec{r_\parallel}}\psi_n(z), \\ E_{n,\vec{k_\parallel}} &= \varepsilon_n + \frac{1}{2}|\vec{k_\parallel}|^2. \end{aligned} \tag{2.56}$$

ε_n and $\psi_n(z)$ satisfy the one-dimensional Kohn-Sham equation

$$[-\frac{1}{2}\frac{d^2}{dz^2} + V_{eff}(z)]\psi_n(z) = \varepsilon_n\psi_n(z). \tag{2.57}$$

The effective potential is given in a similar way as for the semi-infinite system

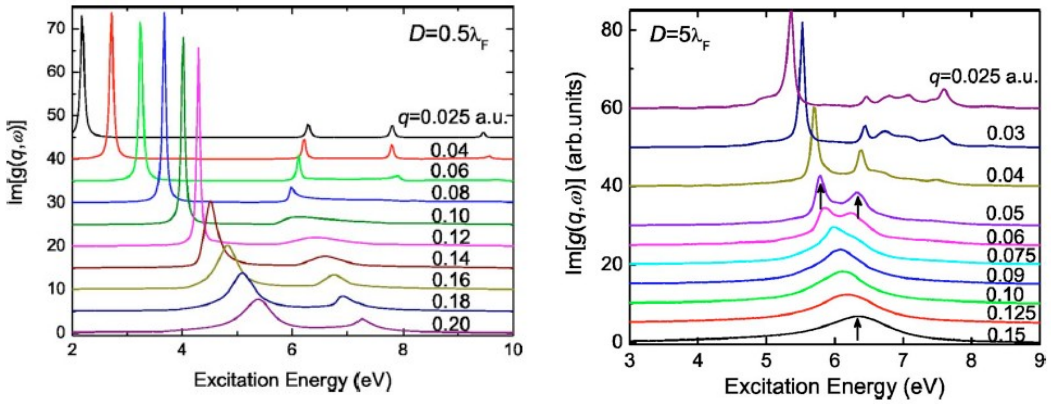
$$V_{eff}(z) = \phi(z) + V_{xc}(z). \tag{2.58}$$

[‡]Unless otherwise specified, the formulas in this subsection are adopted from [101, 102].

The Fermi energy, however, is usually different in a thin film system. It is calibrated to ensure charge neutrality in the system

$$n(z) = 2 \sum_{E_{n,\vec{k}_\parallel} < E_F} |\Psi_{n,\vec{k}_\parallel}(\vec{r})|^2 = \frac{1}{\pi} \sum_{\varepsilon_n < E_F} (E_F - \varepsilon_n)|\psi_n(z)|^2, \int_{-\infty}^{\infty} n(z)dz = n_0 L. \quad (2.59)$$

The remainder of the surface response calculation follows that of a semi-infinite



(a) **(b)**

Figure 2.6: Calculated surface response of (a) a thinner jellium slab ($L = 0.5\lambda_F$) and (b) a thicker jellium slab ($L = 5\lambda_F$) with $r_s = 3$ [101]. The results are qualitatively consistent with classical model except the negative initial dispersion of the surface plasmon (due to the non-local effect) and the extra features in the energy range of 7-8 eV (due to the interaction between the multipole plasmon and antisymmetric mode). Note most of the spectral weight is on the symmetric mode.

system. The main results of the free-standing slab calculation are shown in Figures 2.6a and 2.6b. At large qL, there is only one mode around the surface plasmon energy of the semi-infinite system. For intermediate qL, the mode splits into two branches due to the coupling between the two surface modes. For small q, additional structures appear at high energy due to the hybridization between the multipole plasmon and antisymmetric surface plasmon modes. The induced charge density profiles across the film at different q reflect this hybridization (see Figure 2.7). The multipole mode extends deeper into the slab and couples more strongly with the antisymmetric mode. The symmetric mode is more localized and has little interaction with the multipole

mode. When qL becomes even smaller, the antisymmetric plasmon mode is replaced by intersubband transitions between quantum well states, while the symmetric mode involves intraband excitations with reduced phase space. Both modes acquire single particle character. The enhanced intensity of the symmetric mode indicates it is still collective in nature, however.

As a consequence of the hybridization between the two surface modes and the induced charge density fluctuations across the whole film, the $d(\omega)$ function is not well defined for free-standing thin films.

In reality, it is impossible to grow free-standing metal films that are only several atomic layers thick. The most common method to grow high quality single crystal metal films is molecular beam epitaxy (MBE). Here, the metal vapor is deposited onto a single crystal semiconductor (*e.g.*, Si, Ge) or insulator (*e.g.*, $LaAlO_3$) substrate. For very thin metal films, the influence of the substrate on the dielectric response of the film cannot be neglected. On the other hand, full quantum-mechanical calculations of the substrate-metal overlayer system are also unavailable. First, the atomic structure

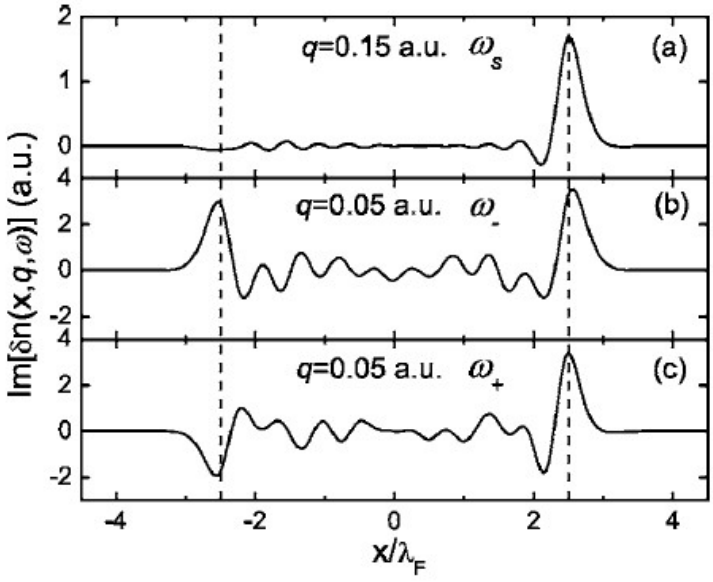


Figure 2.7: Induced charge density at the frequencies of the symmetric and antisymmetric plasmon modes. Dashed lines indicate the jellium edges [101].

or reconstruction during the early stages of film growth is often very complicated. Secondly, the calculations require very large supercells containing many atoms, which is computationally very demanding. Often, the dielectric function of the substrate is incorporated into the TDDFT result of a jellium slab, given by the following explanation.

The dielectric functions of the metal and the substrate are $\varepsilon_1(\omega)$ and $\varepsilon_2(\omega)$, respectively. The surface response function for the dielectric-metal interface is given by [25]

$$g_\varepsilon(q,\omega) = \frac{\varepsilon_{eff} - 1}{\varepsilon_{eff} + 1}, \tag{2.60}$$

where $\varepsilon_{eff}(q,\omega)$ was given by Gadzuk [26],

$$\varepsilon_{eff}(q,\omega) = \varepsilon_1 \frac{\varepsilon_1 + \varepsilon_2 - (\varepsilon_1 - \varepsilon_2)e^{-2qL}}{\varepsilon_1 + \varepsilon_2 + (\varepsilon_1 - \varepsilon_2)e^{-2qL}}. \tag{2.61}$$

The total surface response is a combination of $\mathrm{Im}g_\varepsilon(q,\omega)$ and the quantum mechanical jellium contribution $\mathrm{Im}g_e(q,\omega)$

$$\begin{aligned}
\mathrm{Im}g_\varepsilon(q,\omega) &= \mathrm{Im}\frac{(\varepsilon_1 - 1)(\varepsilon_1 + \varepsilon_2) - (\varepsilon_1 + 1)(\varepsilon_1 - \varepsilon_2)e^{-2qL}}{(\varepsilon_1 + 1)(\varepsilon_1 + \varepsilon_2) - (\varepsilon_1 - 1)(\varepsilon_1 - \varepsilon_2)e^{-2qL}}, \\
\mathrm{Im}g_e(q,\omega) &= -\frac{q}{2\pi}\mathrm{Im}\iint dz dz' \phi^*_{eff}(z,q,\omega)\chi_0(z,z',q,\omega)\phi_{eff}(z',q,\omega) \\
&= -\frac{q}{2\pi}\mathrm{Im}\int dz \phi^*_{eff}(z,q,\omega)\delta n(z,q,\omega), \\
\mathrm{Im}g(q,\omega) &= \mathrm{Im}g_\varepsilon(q,\omega) + \mathrm{Im}g_e(q,\omega).
\end{aligned} \tag{2.62}$$

The surface response of free-standing and substrate supported jellium slabs for $r_s = 3$ are shown in Figure 2.8 [102]. It is clear that the symmetric mode, which is polarized toward the metal-dielectric interface, is strongly damped in the presence of a dielectric substrate.

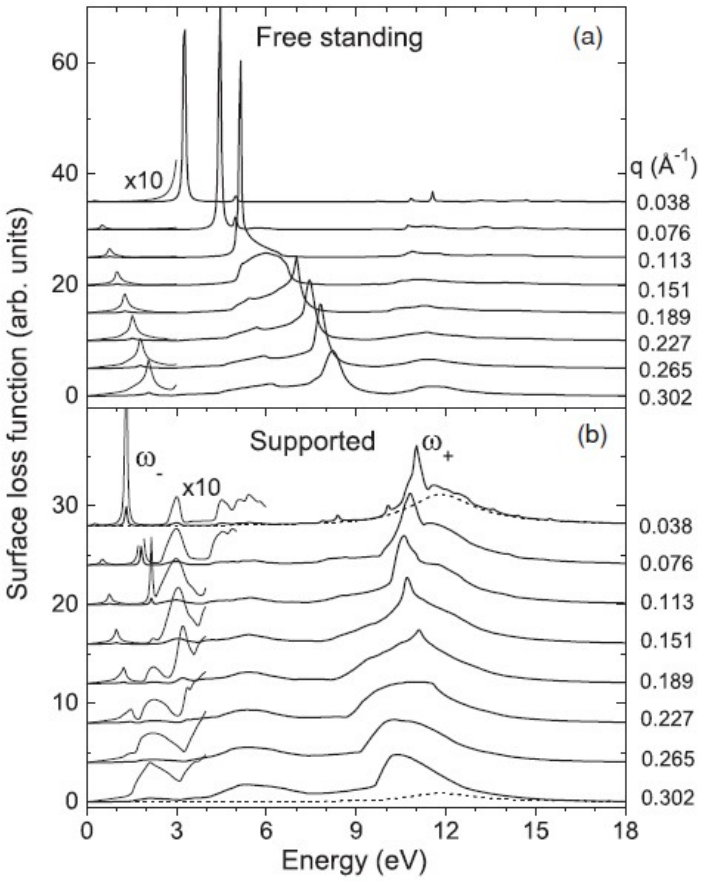


Figure 2.8: The surface response functions for free-standing and substrate-supported jellium films [102]. The symmetric mode is strongly damped in the presence of a dielectric substrate.

2.3 Density functional theory: beyond the jellium model

[§]While the jellium model works well for simple metal systems, it has several drawbacks. First, it does not take real band structure and interband excitations into consideration, which, as we discussed for the classical picture, modulate the dielectric function. Secondly, it fails to reproduce the localized surface electronic states, which

[§]This section is based on the discussion with Dr. A. Eguiluz and R. Van Wesep, as well as Chapter 2 of "Planewaves, Pseudopotentials and the LAPW Method", D. Singh and L. Nordström, Springer Verlag, 2006. Unless otherwise specified, the formulas are from [80].

play an important role in the dielectric and optical properties. Calculations of the plasmon response should be based on the complete *ab initio* band structure.

2.3.1 Ground-state properties

Inclusion of crystal potential into Schrödinger equation can be realized through different methods, depending on the choice of basis set. Pseudopotentials use plane waves and augmented plane wave (APW) methods use space partitioning methods (as explained below). In principle, plane waves form a "complete"basis set, and are used in many band structure calculations. The drawback of plane wave calculations is that they don't converge easily due to the rapid oscillations of the atomic wave functions close to the nuclei. To address this issue, the pseudopotential and APW methods take different approaches. The pseudopotential approach replaces the Hamiltonian near the atoms with a smoother pseudo-Hamiltonian and reproduces the same valence energy spectrum even though the core states are removed. On the other hand, the APW method modifies the plane waves and the resulting augmented plane waves are made orthogonal to the core states. Since the use of a plane wave basis set is common to both methods, a brief introduction to plane wave band structure calculations is given as follows. According to Bloch's theorem, the single particle wavefunction in a periodic crystal lattice is given by

$$\varphi_{\vec{k}}(\vec{r}+\vec{R_L}) = e^{i\vec{k}\cdot\vec{R_L}}\varphi_k(r), \tag{2.63}$$

where $\vec{R_L}$ is a real space lattice vector. The general solution of $\varphi_{\vec{k}}$ is

$$\varphi_{\vec{k}}(\vec{r}) = e^{i\vec{k}\cdot\vec{r}}\sum_{\vec{G}} c_{\vec{G}}(\vec{k})e^{i\vec{G}\cdot\vec{r}} = e^{i\vec{k}\cdot\vec{r}}w(\vec{k},\vec{r}), \tag{2.64}$$

where $\vec{G}$ are the reciprocal lattice vectors. The plane waves are diagonal in the momentum $\vec{p}$ and higher powers of $\vec{p}$. Therefore, they are eigenfunctions of the kinetic energy operator $(\vec{p}^2/2m)$. The plane wave functions are the solution for

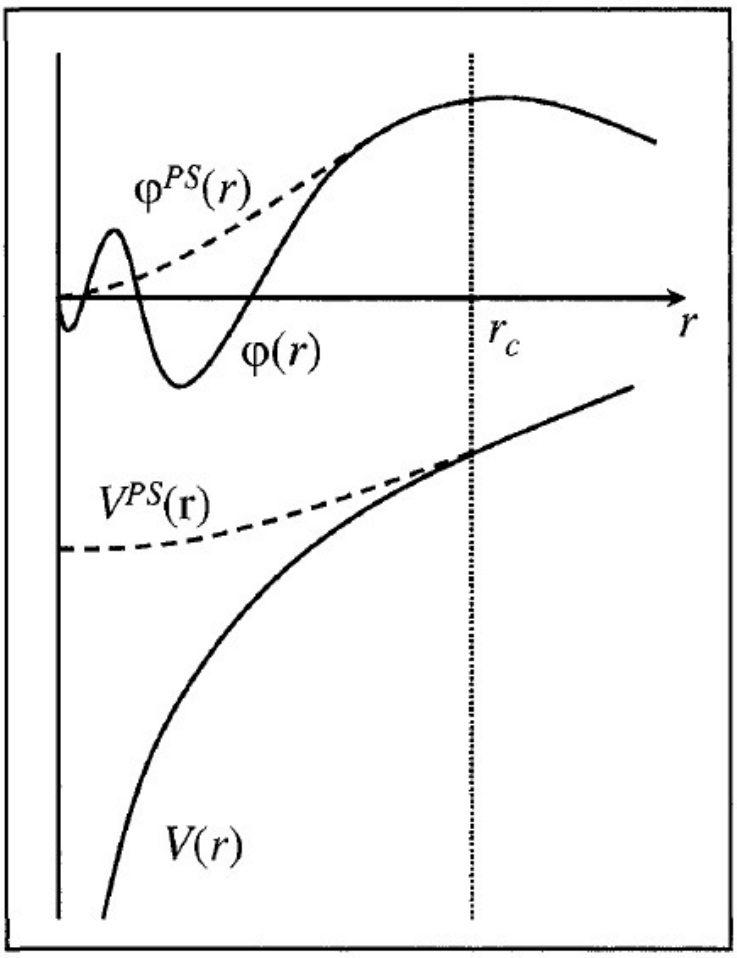


Figure 2.9: Illustration of the pseudopotential construction [80].

the empty lattice approximation (with constant potential, which could be set to 0). The band energies are $(\vec{k}+\vec{G})^2$ (in Rydberg units), and the wave functions are proportional to $e^{i(\vec{k}+\vec{G})\cdot\vec{r}}$. If a weak periodic potential $\triangle V(\vec{r})$ is added to the Shrödinger equation, the wave functions will be a mixture of pure plane wave states. However, it only affects the lowest few bands. Assuming the strongly bound core electrons are "fixed"and less likely to be perturbed by the valence electrons, the strong core potential (including the interaction between core electrons and valence electrons) can be replaced by pseudopotentials so that the ground state wavefunctions reproduce the all-electron wavefunctions outside of the selected core radius. This also removes the core states and the fluctuations in the valence wavefunctions due

to orbital orthogonalization, see Figure 2.9. The principle of the pseudopotential method is simple, but the construction of a pseudopotential is very complicated. A detailed review of the pseudopotential method is available elsewhere [80].

Another competing approach to this crystal potential problem is the APW method, *e.g.*, LAPW. One great thing about the LAPW method is that the number of basis functions per atom is more or less the same throughout the periodic table. One of the most advanced LAPW packages (Full Potential-LAPW) is being developed by a group at the Max Planck Institut in Halle, Germany (http://elk.sourceforge.net). The implementation is led by K. Dewhurst and S. Sharma *et al.* In the APW method, unit cells are divided into atomic spheres and interstitial regions (see Figure 2.10). Two different basis sets are assigned accordingly

$$\varphi(\vec{r}) = \begin{cases} \Omega^{-1/2} \sum_{\vec{G}} c_{\vec{G}} e^{i(\vec{G}+\vec{k})\cdot\vec{r}} & r \in I \\ \sum_{lm} A_{lm}^{K} u_l(r,\varepsilon) Y_{lm}(\hat{r}) & r \in S, \end{cases} \tag{2.65}$$

where φ is a wavefunction, Ω is the cell volume, and $u_l(r,\varepsilon)$ are the numerical solutions of the radial Schrödinger equation. $c_{\vec{G}}$ are expansion coefficients. A_{lm}^{K} are

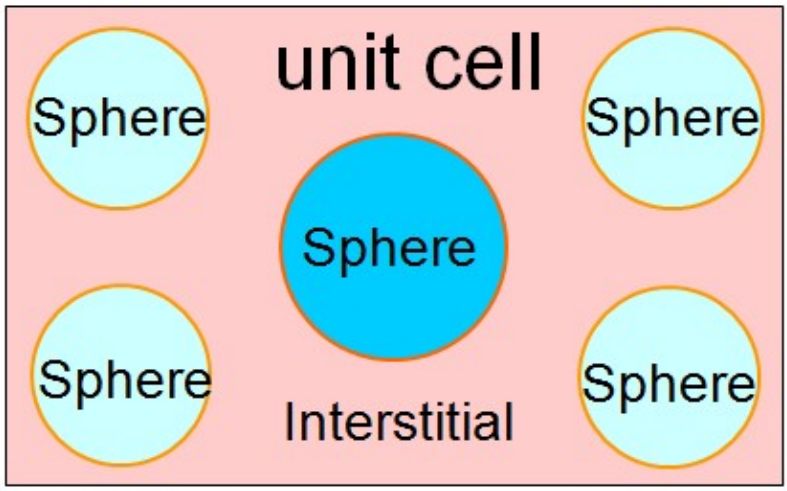


Figure 2.10: Illustration of the partitioning in LAPW method. The unit cell is divided into atomic spheres and interstitial region.

the coefficients for matching the plane wave solutions in the interstitial regions to the atomic-like wavefunctions inside the spheres. Because $u_l(r,\varepsilon)$ depend on energy, this is a non-linear eigenvalue problem which is computationally demanding. To solve this problem, Andersen [6] suggested a method for linearizing the energy dependence. This is the so called LAPW method

$$\Phi_{k_n} = \sum_{lm}[A_{lm}(k_n)u_l(E_l,r) + B_{lm}(k_n)\dot{u}_l(E_l,r)]Y_{lm}(\hat{r}). \tag{2.66}$$

Here, u_l is expanded at E_l and $\dot{u}_l = \partial u/\partial\varepsilon$ has been added. A_{lm}^K and B_{lm}^K are the coefficients for matching plane waves in both value and slope. The additional constraints require more plane waves than APW. In the FP-LAPW scheme, a local coordinate system (LM) is used inside the atomic sphere. The potentials are given as

$$V(r) = \begin{cases} \sum_K V_K e^{i\vec{K}\cdot\vec{r}} & r \in I \\ \sum_{LM} V_{LM}(r)Y_{LM}(\hat{r}) & r \in S, \end{cases} . \tag{2.67}$$

Solving the Schrödinger equation yields the eigenenergies of different states. The nitty-gritties are beyond the scope of the thesis. Details of the implementation of LAPW are available elsewhere [80]. In our studies for the ground state calculation of non-jellium system, the GGA-PBE type exchange-correlation energy was used [66].

2.3.2 Time-dependent response properties

Once the ground state is prepared, the Kohn-Sham density response function can be converted into a matrix equation in $\vec{G}$-space of reciprocal lattice vectors via Fourier transformation [44]

$$\chi_{\vec{G}\vec{G}'}(\vec{q},\omega) = \chi^{KS}_{\vec{G}\vec{G}'}(\vec{q},\omega) + \sum_{\vec{G}_1\vec{G}_2} \chi^{KS}_{\vec{G}\vec{G}_1}(\vec{q},\omega)[v_{\vec{G}_1+\vec{q}}\delta_{\vec{G}_1\vec{G}_2} + f^{xc}_{\vec{G}_1\vec{G}_2}(\vec{q},\omega)]\chi_{\vec{G}_2\vec{G}'}(\vec{q},\omega), \tag{2.68}$$

where $\vec{q}$ is any vector within the first Brillouin zone and $v_{\vec{G}+\vec{q}} = \frac{4\pi}{|\vec{G}+\vec{q}|^2}$ correspond to the expansion coefficients of the bare Coulomb interaction. The Kohn-Sham density-response matrix is [44]

$$\begin{aligned}\chi^{KS}_{\vec{G}\vec{G}'}(\vec{q},\omega) = \frac{1}{N_k\Omega}\sum_{k}^{BZ}\sum_{jj'}\frac{f_{j\vec{k}} - f_{j'\vec{k}+\vec{q}}}{\varepsilon_{j\vec{k}} - \varepsilon_{j'\vec{k}+\vec{q}} + \omega + i\delta}\times \\ \times\left\langle \Psi_{j\vec{k}}|e^{i(\vec{G}+\vec{q})\cdot\vec{r}}|\Psi_{j'\vec{k}+\vec{q}}\right\rangle\left\langle \Psi_{j'\vec{k}+\vec{q}}|e^{-i(\vec{G}'+\vec{q})\cdot\vec{r}}|\Psi_{j\vec{k}}\right\rangle .\end{aligned} \tag{2.69}$$

Here we skip the theoretical details but define several important physical quantities that will be used for the phenomenological model in Chapter 5. They are complex functions, given by [¶]

$$\begin{aligned}\chi_{\vec{q}-\vec{G}_q,\vec{q}-\vec{G}_q} &= \left\{[\mathbb{I} - \chi^{KS}(v(\vec{q}) + f_{xc})]^{-1}\chi^{KS}\right\}_{\vec{q}-\vec{G}_q,\vec{q}-\vec{G}_q}, \\ \chi_{scalar} &= \frac{\chi^{KS}_{\vec{q}-\vec{G}_q,\vec{q}-\vec{G}_q}}{1 - \chi^{KS}_{\vec{q}-\vec{G}_q,\vec{q}-\vec{G}_q}[v(\vec{q}) + f_{xc}]_{\vec{q}-\vec{G}_q,\vec{q}-\vec{G}_q}}, \\ \varepsilon_{eff} &= \frac{1}{1 + v(\vec{q})_{\vec{q}-\vec{G}_q,\vec{q}-\vec{G}_q}\chi_{\vec{q}-\vec{G}_q,\vec{q}-\vec{G}_q}}, \\ \varepsilon_{eff-scalar} &= \frac{1}{1 + v(\vec{q})_{\vec{q}-\vec{G}_q,\vec{q}-\vec{G}_q}\chi_{scalar}}.\end{aligned} \tag{2.70}$$

For RPA in TDDFT frame, $f_{xc} = 0$.

It is instructive to make a comparison between the jellium model and advanced methods that include the crystal potential. In periodic systems, the eigenstates are Bloch states as opposed to the plane waves in jellium. For periodic systems, all crystal momenta are physically equivalent to those inside the first Brillouin zone. They are unrestricted in the case of a jellium system. Whenever there is a need to sum over all the eigenstates in the response function calculation, all bands in the first Brillouin Zone (BZ) need to be included. Also, in jellium, quantities like χ and ε are scalars. In a periodic system, they consist of matrices defined for each point inside the 1^{st} BZ and for each frequency, with indices corresponding to reciprocal lattice vectors.

[¶]R. Van Wesep, private communication.

Another difference is that in jellium, the Hartree energy exactly cancels the uniform positive background potential, whereas in a periodic system, it doesn't. The potential has to be included self-consistently.

2.3.3 Plasmons in thin films

To the best of our knowledge, there are only very few theoretical studies focusing on the dielectric response of ultrathin films within the LAPW framework [98]. The main difficulties are on the computational side. First, adding more layers to the unit cell makes the problem harder to solve. Secondly, for a periodic slab calculation, additional empty space is needed to separate the slabs. The latter increases the dimension of the unit cell in the normal direction, which in turn increases the density of $k-$points along the corresponding direction in reciprocal space. Since the APW basis set and dimensions of the ε-matrices scale with the number of reciprocal lattice points, this makes everything much harder. Besides, even though the occupied states converge quickly with the magnitude of the vacuum gap separating the slabs, the unoccupied states above the Fermi level don't converge so well. Difficulties also come from the response function calculation. The result in the optical limit is not reliable, because small momentum transfers can induce transitions between the k-point replicas associated with the periodic slab geometry. The latter is, of course, unphysical.

2.4 Inelastic electron scattering

[‖]The energy loss of fast electrons passing through a medium with dielectric constant ε can be characterized by the power loss [78]Electronic excitations at metal surfaces can be observed by inelastic electron scattering, such as REELS. In this section, the connection between the loss spectra and dielectric function will be made.

$$dw/dt = \vec{E} \cdot d\vec{D}/dt, \tag{2.71}$$

[‖]This section is based on [32, 54].

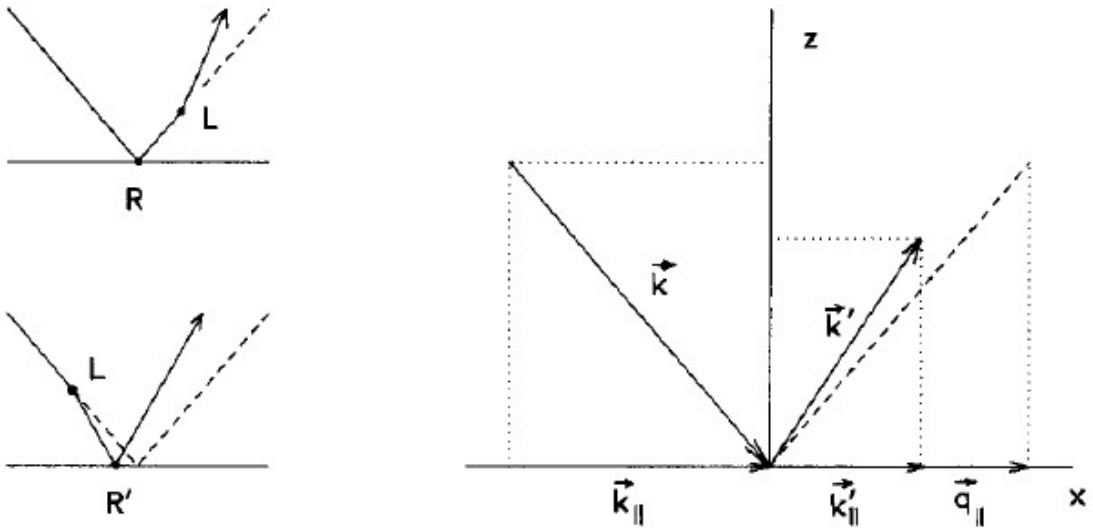


Figure 2.11: Illustration of the inelastic scattering process: loss after (left top) or before (left bottom) elastic scattering. Wave vector diagram for incident and scattered electrons is shown on the right. [54]

where

$$\nabla \cdot \vec{D} = -\rho = -e\delta(\vec{r} - \vec{v}_{el} \cdot t). \tag{2.72}$$

The energy loss per unit volume is then given by [78]

$$\begin{aligned} w = \mathrm{Re}\left\{\int_{-\infty}^{\infty} \vec{E} \cdot \dot{\vec{D}} dt\right\} &= \mathrm{Re}\left\{2i\pi \int_{-\infty}^{\infty} \omega E(\omega) D^*(\omega) d\omega\right\} \\ &= -2\pi \int_{-\infty}^{\infty} \omega \mathrm{Im}\left\{\frac{1}{\varepsilon(\omega)}\right\} \frac{|D(\omega)|^2}{\varepsilon_0} d\omega, \end{aligned} \tag{2.73}$$

where $-\mathrm{Im}\left\{\frac{1}{\varepsilon(\omega)}\right\}$ is the intrinsic loss function of the material. The other contributions constitute the kinematic prefactor. In the case of REELS, the electric field associated with the electrons travelling near the surface is screened by a factor of $1/[\varepsilon(\omega) + 1]$ instead of $1/[\varepsilon(\omega)]$. As a consequence, the surface loss function is $-\mathrm{Im}\left\{\frac{1}{\varepsilon(\omega)+1}\right\}$. The pole-like structures at $\varepsilon(\omega) = 0$ and $\varepsilon(\omega) = -1$ correspond to bulk and surface plasmons, respectively.

The loss functions provide a qualitative picture of the inelastic electron scattering. A more sophisticated description of this process requires an exact expression for the kinematic prefactor and knowledge of the $q_{\parallel}$-dependent electron energy loss probability. In general, the REEL spectrum is a combination of elastic reflection due to Bragg diffraction (interaction between the incident electron beam and crystal potential) and small-angle inelastic scattering, due to the excitation of electron-hole pairs and collective modes. For the latter, the energy loss happens either before or after elastic scattering. The long-range Coulomb field of the incident electrons interacts with the dipolar field from the induced surface charges. This process is called dipole scattering. The induced dipole field decays exponentially with increasing $q_{\parallel}$. Therefore, the cross section for dipole scattering is largest at angles close to the specular direction. Inelastic scattering events within the surface region are categorized as impact scattering. The angular distributions of the scattering intensity are different from those of dipole scattering. However, the frequencies of the surface modes should be the same. With the energy E (E') and polar angle θ (θ') of the incident (scattered) beam given, the scattering efficiency S per unit solid angle $d\Omega$ and unit energy $d\hbar\omega$ is given by [32, 54]

$$\frac{d^2S}{d\Omega d\hbar\omega} = \frac{m^2e^2k'v_{\perp}^2}{2\pi^2\hbar^5 k\cos\theta}\frac{|v_{\perp}q(R+R') + i(R-R')(\omega - \vec{v_{\parallel}}\cdot\vec{q_{\parallel}})|^2}{[v_{\perp}^2q^2 + (\omega - v_{\parallel}\cdot\vec{q_{\parallel}})^2]^2}\frac{P(\vec{q_{\parallel}},\omega)}{q^2}, \tag{2.74}$$

where k (k') is the magnitude of the wave vector of the incident (scattered) electrons and $v_{\perp}$ ($v_{\parallel}$) is the normal (parallel) velocity of the incident electron (see Figure 2.11). q is the magnitude of $\vec{q_{\parallel}}$. R (R') is the elastic scattering amplitude for specular angle, after (before) the reflection. Note that energy and parallel momentum conservations apply

$$\begin{aligned} E &= E' + \hbar\omega, \\ \vec{k_{\parallel}} &= \vec{k'_{\parallel}} + \vec{q_{\parallel}}. \end{aligned} \tag{2.75}$$

$P(\vec{q_\parallel},\omega)$ [32, 54] is the quantity that includes the intrinsic energy losses.

$$\begin{aligned} P(\vec{q_\parallel},\omega) &= -\frac{q^2}{4\pi^2}\mathrm{Im}\int d^3r \int d^2r' \phi^*_{ext}(\vec{r},\omega)\chi(\vec{r},\vec{r'},\omega)\phi_{ext}(\vec{r'},\omega) \\ &= -\frac{q^2}{4\pi^2}\mathrm{Im}\int d^3r \int d^2r' \phi^*_{ext}(\vec{r},\omega)\chi_1(\vec{r},\vec{r'},\omega)\phi_{scf}(\vec{r'},\omega) \\ &= \frac{q}{2\pi}\mathrm{Im}g(q,\omega) \\ &= \frac{q^2}{8\pi^2}w(q,\omega). \end{aligned} \tag{2.76}$$

Note that $\mathrm{Im}g(q,\omega)$ is equivalent to the surface loss function.

Chapter 3

Experimental Techniques

3.1 Ultrahigh vacuum system

*Ultrahigh vacuum or UHV (10^{-8} Pa or below, see the conversion factors for pressure units in Table 3.1) is always desirable and necessary for surface science because of two reasons. First, to avoid surface contamination and, second, to prevent interference from gas phase scattering in surface spectroscopy. The number of molecules reaching the sample surface is proportional to the pressure, *e.g.*, it only takes 1 second to fully cover the sample surface at 10^{-5} Pa. On the other hand, most techniques for surface studies are electron or ion-based. The average distance of a travelling particle between successive collisions, or mean free path, becomes shorter as the gas density (pressure) increases. To achieve UHV, a wide range of pumps and gauges are used. A schematic drawing of the UHV chamber in use is provided in Figure 3.1. The pressure in a vacuum system is limited by the chamber volume, outgassing, diffusion and permeation during the pump-down procedure. Generally speaking, there are two broad categories of vacuum pumps: gas-transfer pumps and entrapment pumps. Gas transfer pumps remove the gas molecules from the system and expel them by

*Technical details of UHV and electron spectroscopy are based on "Materials Science of Thin Films"(M. Ohring, Academic Press, 2002) and "Electron Spectroscopy for Surface Analysis"(H. Ibach, Springer Verlag, 1977.), respectively.

Table 3.1: Conversion factors between different pressure units

Pressure units	Pascal	bar	mbar	Torr (mm Hg)	atm
Pascal	1	10^{-5}	10^{-2}	$7.5006 \cdot 10^{-3}$	$9.8692 \cdot 10^{-6}$
bar	10^{5}	1	10^{3}	750.06	0.98692
mbar	10^{2}	10^{-3}	1	0.75006	$9.8692 \cdot 10^{-4}$
Torr (mm Hg)	$1.3332 \cdot 10^{2}$	$1.3332 \cdot 10^{-3}$	1.3332	1	$1.3158 \cdot 10^{-3}$
atm	$1.0133 \cdot 10^{5}$	1.0133	1013.3	760	1

compression. Depending on the working mechanisms and pressure ranges, the gas trasfer pumps could be further divided into positive displacement (*e.g.*, dry scroll pump) and kinetic vacuum pumps (*e.g.*, turbomolecular pump). Entrapment pumps condense or bind molecules on the inner surface of the pump and release the gas when warmed up. Ion pumps and titanium sublimation pumps (TSP) belong to this category.

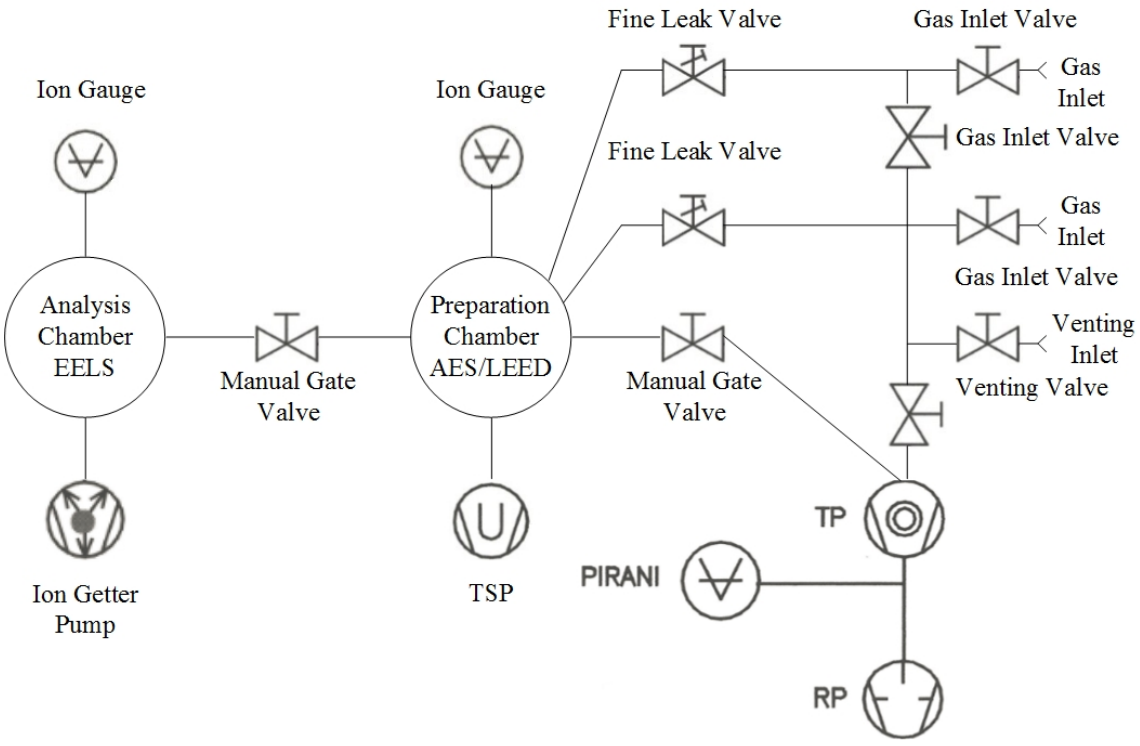


Figure 3.1: Schematic diagram of the UHV chamber.

Monitoring the vacuum environment is another important aspect of UHV maintainance. Most vacuum gauges record the pressure indirectly by measuring thermal conductivity (*e.g.*, pirany gauge), or ionization current (*e.g.*, hot-cathode gauge), etc. The former type of gauge works at $\sim 10^{-4}$ torr to 1 atm. In this regime, the rate of heat transfer through a gas is linearly proportional to the pressure. In a pirany gauge, for instance, the resistance of a hot metal filament heated reflects the gas pressure. The latter type of gauge covers $\sim 10^{-5}$ to $\sim 10^{-12}$ mbar range. Here, the gas molecules are usually ionized in a tube consisting of filament and a positively biased grid. The ion current collected is a measure of the gas density. Because different molecules have different sensitivity, the reading of the gauge relies on the presumed gas composition and thus may differ from the real gas pressure.

Further analysis of individual gaseous species involves mass spectrometry with a residual gas analyzer (RGA). In a typical RGA, a quadrupole mass analyzer is used. Residual gases are ionized and oscillating electric fields are applied to the four cylindrical rods so that only the ions with selected mass-to-charge ratio can pass through without colliding with the rods. RGAs are often used for leak testing where they detect He gas that may penetrate the chamber through the vacuum leak.

There are several techniques for growing ultrathin films and they are generally classified as physical (PVD) or chemical vapor deposition (CVD). For PVD, source material is evaporated and deposited directly onto the substrate surface. In CVD, the source material is usually bound to a volatile precursor gas and transported onto the substrate where the precursor molecules decompose and precursor fragments re-evaporate. Each method has its own merits and the choice often reflects a compromise between desired film quality and fabrication cost. For the purpose of demonstrating quantum size effects in thin films, the film has to have high purity, very few defects, and needs to be single crystalline and atomically flat. MBE is by far the best method to serve this purpose. A single crystal substrate with specific surface orientation is first prepared in UHV. The Si(111) and Ge(111) surfaces used in our studies were cleaned by thermal annealing or by Ar-ion sputtering, followed by annealing. The

early stages of heteroepitaxy are characterized by the nucleation of vapor atoms or molecules on the surface. The island density saturates quickly and the islands continue to grow laterally until they coalesce into a continuous film.

Subsequent film formation usually falls into three basic growth modes: island or Volmer-Weber growth, layer-by-layer or Frank-Van der Merwe growth, and layer plus island or Stranski-Krastanov growth. The growth mode depends on the Gibbs free energy of the film and substrate surfaces, and that of the film-substrate interface. The thin film material usually differs from the substrate. The structure of the film is often described in terms of a 2D Bravais lattice with 2D primitive lattice vectors. The primitive lattice vectors of the film can often be expressed as a linear combination of the primitive lattice vectors of the substrate surface. For instance, if the primitive translation vectors of the 2D substrate surface are $\vec{a_1}$ and $\vec{a_2}$, the adsorbate's lattice vectors $\vec{b_1}$ and $\vec{b_2}$ are defined as

$$\begin{aligned} \vec{b_1} &= M_{11}\vec{a_1} + M_{12}\vec{a_2}, \\ \vec{b_2} &= M_{21}\vec{a_1} + M_{22}\vec{a_2}, \end{aligned} \tag{3.1}$$

where M_{ij} $(i, j = 1, 2)$ denote the transformation-matrix elements. For example, the $Si(111)-(7\times7)$ surface reconstruction has unit cell parameters that are 7 times larger than those of the (hypothetical) bulk truncated Si(111) surface. The transformation matrix reads

$$M = \begin{vmatrix} 7 & 0 \\ 0 & 7 \end{vmatrix} \tag{3.2}$$

When the transformation matrix is not diagonal, the unit cell of the film is rotated with respect to the substrate. For instance, the transformation matrix for the Pb/Ge (111) $(\sqrt{3} \times \sqrt{3})R30^\circ$ surface is

$$M = \begin{vmatrix} 1 & 1 \\ 2 & -1 \end{vmatrix} \tag{3.3}$$

where R represents the rotation. To monitor the surface crystallography and film growth rate, a joint low energy electron diffraction (LEED) and Auger electron spectroscopy (AES) study was performed.

3.2 Low energy electron diffraction and Auger electron spectroscopy

The UHV chamber is equipped with a 4-grid retarding field LEED/AES system with a built-in electron gun. A schematic diagram of the LEED/AES optics is presented in Figure 3.2. The first grid is grounded so that the back scattered electrons from the surface travel in a field-free region. The fourth grid is grounded in order to shield the collector screen from the negative bias applied to the second and third grids (two retarding grids are used to reduce field inhomogeneities). This negative retarding potential serves to prevent inelastically backscattered electrons from reaching the LEED screen. The latter is held at + 5 keV so that elastically scattered (i.e., Bragg

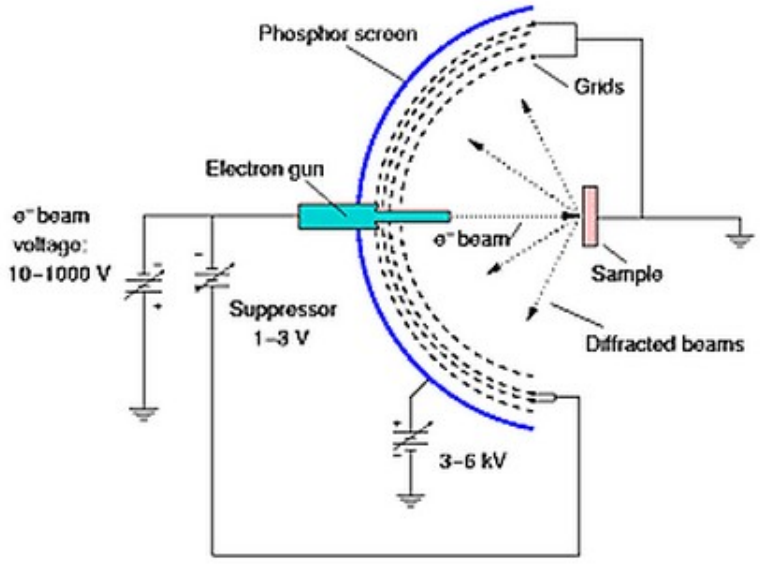


Figure 3.2: Schematic diagram of 4-grid LEED-AES optics (produced by the Surface Science Laboratory at Universidad Autónoma de Madrid).

diffracted) electrons are accelerated toward the collector screen, where they illuminate the phoshor coating of the screen, revealing a diffraction pattern. In LEED, the beam energy is typically in the 30 to 500 eV energy range. This range corresponds to the minimum in the mean free path curve, see Figure 3.3, so that the backscattered electrons originate from the outermost surface layers. The resulting LEED pattern on the collector screen is a direct image of the surface reciprocal lattice. The same electron optics and retarding potential analyzer are utilized for AES. An Auger transition is a physical process in which an atom is ionized by x-rays or a high energy electron beam, leaving behind a deep core hole (E_A). The core hole is subsequently filled with an electron from a higher energy level (E_B). The energy released in this intra atomic decay process is often sufficient to ionize a shallow core level (E_C). The outgoing Auger electron is then measured in AES (see Figure 3.4). The kinetic energy

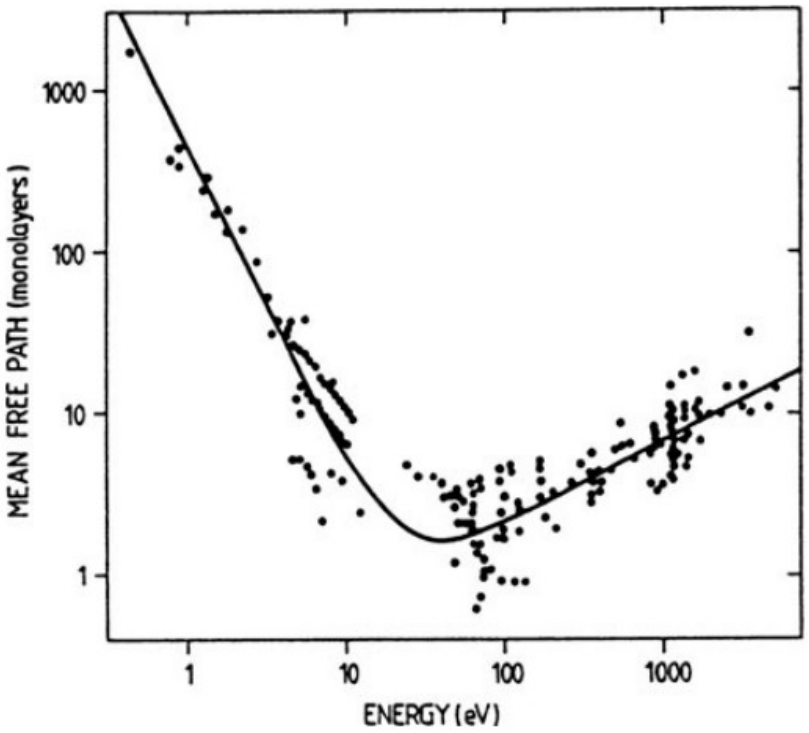


Figure 3.3: Theoretical and experimental values of the inelastic mean free path as a function of electron's kinetic energy. [56]

of the Auger electron is given by

$$KE = (E_B - E_A) - (E_C - E_B) - \phi, \tag{3.4}$$

where ϕ is the work function of the spectrometer. Note that the kinetic energy is independent of the energy of the incident photon or electron beam. Consequently, it is element specific as it only dependent on element-specific core level binding energies. Therefore, the Auger spectrum is a chemical fingerprint of the surface. Auger transitions are usually denoted by the shell symbols (see Table 3.2). In the

Table 3.2: Shell notation for Auger transitions

Energy level	1s	2s	2p	3s	3p	3d	4s
Shell symbol	K	L_1	L_{23}	M_1	M_{23}	M_{45}	N_1

Auger mode of a four grid LEED/AES system, the measured current is an integration of all electrons with energies above the retarding potential on the second and third grid: $I(E) \propto \int_E^\infty N(E)dE$. $N(E)$ is the number of detected electrons which have kinetic energy E. The derivative of the current versus retarding potential provides

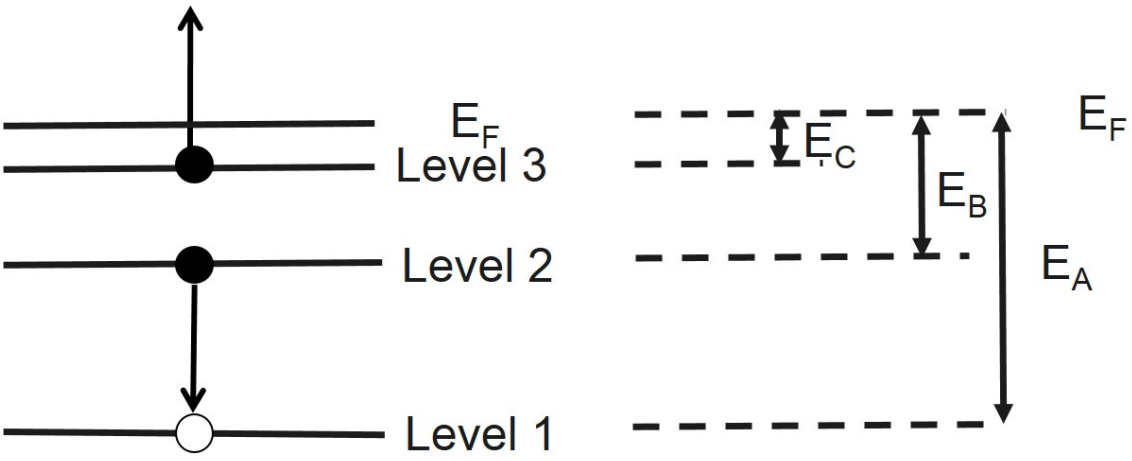


Figure 3.4: Schematic diagram of Auger transition process.

the energy spectrum $N(E) \propto dI(E)/dE$. In a typical spectrum (Figure 3.5), Auger-peaks are dwarfed by a huge background of secondary electrons. To extract a useful Auger signal, a small AC modulation voltage $\triangle E = K\sin\omega t$ is added on top of the beam voltage and retarding potential. The collected current is then given by [31]

$$\begin{aligned} I(E+\triangle E) &\approx I(E) + I'(E)\triangle E + \frac{I''(E)}{2}\triangle E^2 + \frac{I'''(E)}{3!}\triangle E^3 + ... \\ &\approx I_0 + I'(E)\sin\omega t - \frac{1}{4}I''(E)K^2\cos 2\omega t + ... \end{aligned} \tag{3.5}$$

A lock-in amplifier is used to detect the electronic signal from the Auger electrons while filtering out secondary electrons. The Lock-in signal at frequency 2ω corresponds to $dN(E)/dE$. By monitoring the intensity of the Auger electrons originating from the substrate and thin film material as a function of deposition time, it is often possible to calibrate the deposition rate.

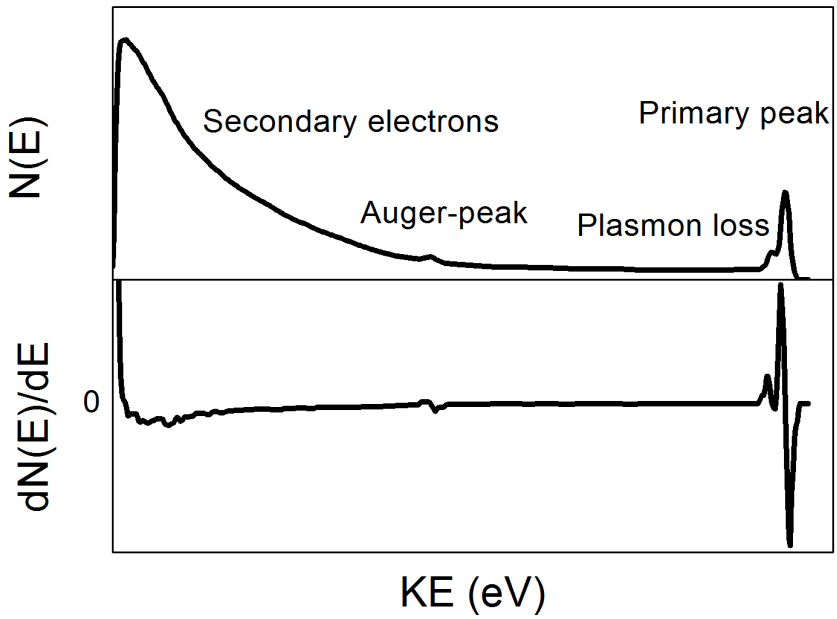


Figure 3.5: Direct Auger spectrum (upper panel) and differential Auger spectrum (lower panel).

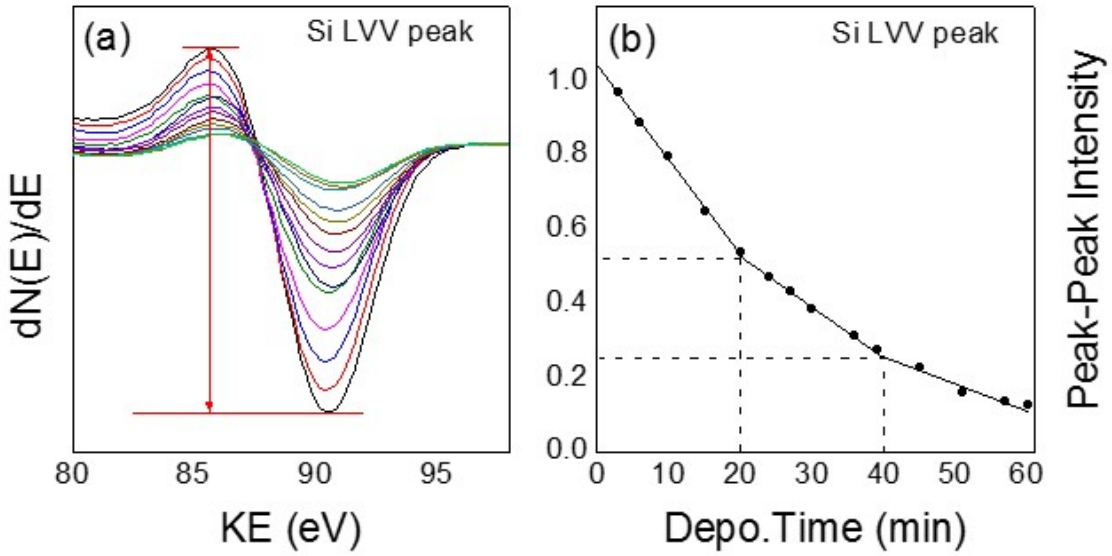


Figure 3.6: (a) Attenuation of the differential Si LVV Auger spectra as a function of deposition time. (b) Characteristic linear segment plot used to determine the Mg deposition rate.

3.3 Deposition rate calibration with Auger electron spectroscopy

The deposition rate of Mg was calibrated by measuring the attenuation of the Si LVV peak-to-peak Auger signal as a function of deposition time, using the combined retarding field LEED/AES system. The Si(111)-7 $\times$ 7 substrate was maintained at 200 K during the thickness calibration, to minimize silicide formation at the interface [2, 61, 62]. Differential Auger spectra were collected as a function of deposition time. The Mg film was flashed off each time after collecting the spectrum, and the Si LVV Auger peak was measured again. This way, the attentuation was measured without rotating the sample between the evaporation and measurement positions inside the vacuum chamber. The use of peak-to-peak intensities in the differential spectra requires that the LVV lineshape is independent of the Mg coverage. The raw data, displayed in Figure 3.6(a), show that this is indeed the case. For layer-by-layer

growth mode, the exponential attenuation of the Si LVV intensity is given by [7]

$$I_{Si} \propto [(1-x)e^{-nd/\lambda} + xe^{-(n+1)d/\lambda}], \tag{3.6}$$

where d ($\approx$ 2.6 Å) is the thickness of a single atomic Mg(0001) layer; λ is the apparent escape depth of the Auger electrons, which needs to be corrected for the wide acceptance angle of the retarding field analyzer (about 60°); x is the area fraction of the Mg film covered with $(n+1)$ layers, and $1-x$ is the area fraction covered by n layers. Accordingly, the initial Si LVV intensity decreases linearly with deposition time until the first atomic layer is completed. Beyond this point, the LVV intensity continues to decrease linearly, but with a reduced slope (given by $e^{-2d/\lambda}$), until the second layer is also completed, and so on. Our deposition rate calibration is shown in Figure 3.6(b). The Si LVV Auger signal clearly decays in equally long linear segments as a function of deposition time, thus confirming layer-by-layer growth. From the kink positions, we determined a deposition rate of 0.05 ± 0.005 ML/min. The fitted value of λ = 3.76 Å corresponds to a mean free path (ξ) of 5.78 Å, which is determined from

$$e^{-\frac{d}{\lambda}} = \frac{2}{3}\int_0^{\frac{\pi}{3}} e^{-\frac{d}{\xi\cos\theta}} \tan\theta \; d(\tan\theta), \tag{3.7}$$

where θ is the angle between the trajectory of the escaped electron and the surface normal of sample.

The deposition rate of the Pb source was calibrated by measuring the increase of the 94 eV Pb NOO Auger signal on Ge(111) as a function of deposition time at room temperature. At room temperature, Pb grows according to the Stranski-Krastanov mechanism in which 3D islands nucleate right after the first monolayer is completed [27, 48]. The in-plane lattice mismatch between Pb(111) and Ge(111) is 13% (Pb(111):4.92$\mathring{A}$ versus Ge(111):5.65$\mathring{A}$). However, a 30° in-plane rotation of a Pb(111) layer with respect to the Ge(111) substrate reduces the lattice mismatch to less than 1% and gives rise to a $(\sqrt{3} \times \sqrt{3})R30°$ periodicity [84]. There are in fact three different reconstructions with the same periodicity, namely the γ, α and

β phases at 1/6, 1/3 and 4/3 ML, respectively. Here, the coverages are expressed in terms of the atomic density in the Ge(111) plane. The 4/3 ML phase consists of a 1% compressed closed-packed Pb(111) plane that is rotated 30° with respect to the (111) plane of Ge, see Figure 3.7. The Pb NOO Auger intensity is expected to increase linearly until this layer is completed. Since additional deposition results in 3D islands that only cover a relatively small fraction of the total surface area (as compared to 2D film growth), we expect to see a clear kink in the Auger intensity when plotted as a function of deposition time. This is indeed the case, as is shown in Figure 3.8. The kink corresponds to the completion of the slightly compressed Pb(111) layer, which in turn provides a very accurate calibration of the deposition rate.

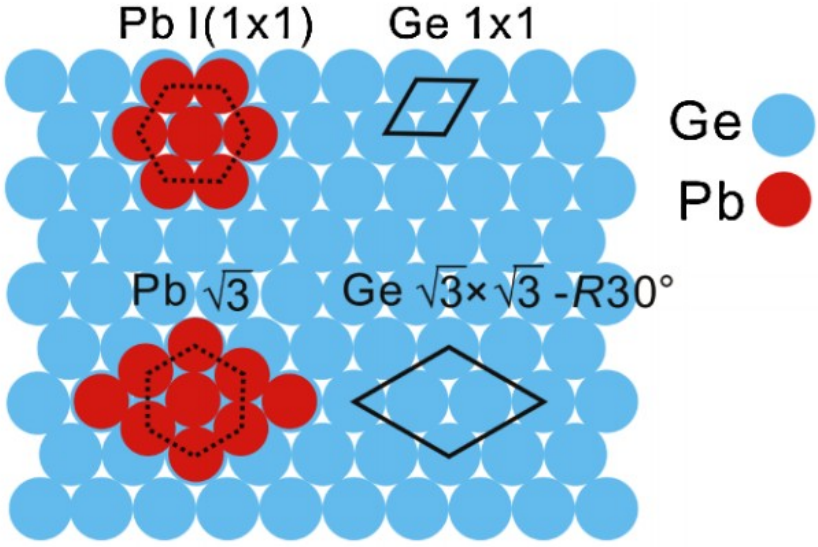


Figure 3.7: The surface reconstruction of Pb on Ge(111) substrate at 4/3 ML coverage [84]. Note in the lower unit cell, there are 4 Pb atoms in the overlayer *vs.* 3 Ge atoms in the substrate. The surface atomic density of Pb(111) is about 4/3 times of Ge(111).

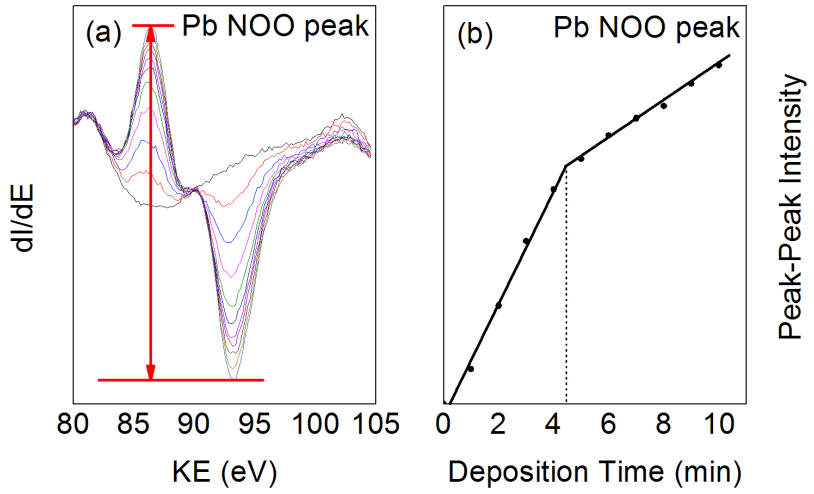


Figure 3.8: (a)Intensification of Pb Auger NOO signal at 94 eV. (b) The "kink" that marks the completion of first monolayer.

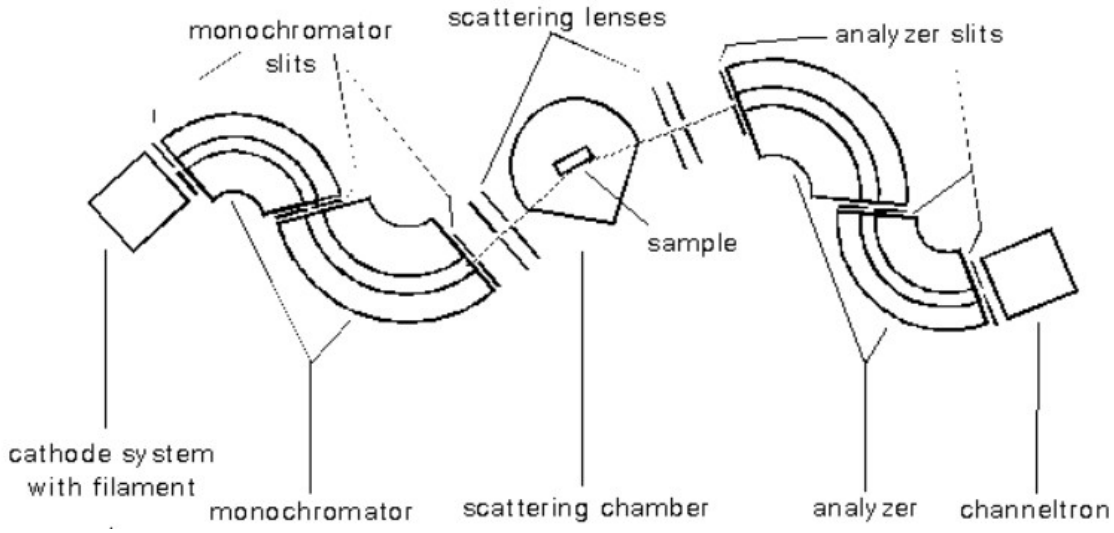


Figure 3.9: Schematic diagram of the HREEL spectrometer with double-pass 127° monochromator and kinetic energy analyzer.

3.4 High resolution electron energy loss spectroscopy

Electron energy loss spectrometers are the main tool for studying plasmons excited by a beam of electrons. They are generally divided into two classes: transmission EELS and reflection EELS. While transmission EELS is frequently used to study the bulk properties, the reflection mode is much more sensitive to the surface. Some electrons interacting with the sample lose their energy to various surface excitations such as molecular-adsorbate vibrations, phonons, and plasmons. The scattered electrons are counted after passing through an electron energy analyzer. By plotting the electron count rate as a function of the loss energy, we obatin an EELS spectrum. At zero-loss energy, there is a large elastic peak. Typical energy losses associated with phonon, molecular vibration, and plasmon excitations are at $\sim 10meV$, $\sim 100meV$, and $\sim 10eV$, respectively. The absence of molecular vibrations usually indicates that the surface is clean. As discussed in the final section of Chapter 2, the reflection EELS spectrum is a convolution of the surface loss function and kinematic prefactor in the dipole scattering limit. The parallel momentum transfer in the scattering process $\hbar q_{\|}$ can be calculated from the scattering angle, according to $\hbar q_{\|}=\sqrt{2mE_i}\sin\theta_{in} - \sqrt{2m(E_i - E_{loss})}\sin\theta_{sc}$, where θ_{in} and θ_{sc} are the angles of the incident and scattered electron beams relative to the surface normal. E_i and E_{loss} are the incident beam energy (in our case 30 eV and 50 eV were used) and loss energy, respectively, and m is the free electron mass. The formula is derived assuming conservation of energy and parallel momentum.

A HREELS system consists of several components: an electron gun, monochromator, scattering chamber, lenses, aperture, analyzer and detector; see Figure 3.9. The main parts for the monochromator and kinetic energy analyzer are the 127° double-pass cylindrical deflector analyzers (CDA). The calibration equation for the pass energy E_0 is [31]

$$E_0 = e\triangle V/2ln(R_2/R_1), \tag{3.8}$$

where $\triangle V$ is the potential difference between the electrodes of the CDA. R_2 and R_1 are the radii of the outer and inner electrodes, respectively. The best resolution is given by [31]

$$\triangle E_B/E_0 = A\triangle S + B\alpha^n + C\beta^2, \tag{3.9}$$

where $\triangle E_B$ is called the base resolution. $\triangle S$ is the aperture, or slit width, at the analyzer entrance and exit (for unequal widths, $\triangle S$ is replaced by $(\triangle S_1 + \triangle S_2)/2$). α and β are the semiangular apertures, respectively, while A, B, C and n are instrument-dependent constants. For our CDA

$$\begin{aligned} A &= 2/R_0, \\ B &= 4/3, \\ C &= 1, \\ n &= 2, \end{aligned} \tag{3.10}$$

where R_0 is the radius of curvature of the central trajectory [31]. According to the equation for the base resolution, the absolute energy resolution $\triangle E$ is proportional to E_0. Therefore, pre-retardation of the electron beam greatly improves the absolute energy resolution. Pre-retardation is accomplished by special electron optics at the entrance, which keep the electron beam focused during deceleration. A detailed discussion of the optimization and transmission function is available in Ref. [31].

Chapter 4

Quantum Oscillations in the Surface Excitations of Ultrathin Mg(0001) Films

In this chapter, we present the first experimental observations of quantum-size-effect oscillations in the collective plasmon response of ultrathin metal films. Specifically, we observe thickness-dependent oscillatory variations in the linear dispersion coefficient of the monopole surface plasmon mode of Mg(0001) films, grown epitaxially on Si(111). The spectral intensities of the photoemission threshold excitation and multipole surface plasmon mode follow a similar quantum oscillatory pattern. These oscillatory features in the plasmon response closely follow the previously reported oscillatory trend in the thickness-dependent chemical reactivity of the films [1, 13], a remarkable coincidence since chemical reactivity is usually determined by single particle quantum levels, while plasmon physics involves the collective screening response of the entire electron gas. These observations can be reconciled by considering the thickness-dependent variations of the ground state charge spilling, associated with the periodic Fermi level crossings of the 2D subband system, as discussed in Chapter 1. Because the charge spilling can be controlled by adjusting

the film thickness and its boundary conditions, these insights are expected to be significant in the design of quantum-sized plasmonic devices.

4.1 Experimental Procedures

Atomically-smooth crystalline Mg(0001) films were grown on a Si(111)-(7×7) substrate in ultrahigh vacuum. The films were deposited at 120 K and post-annealed to room temperature (RT) to achieve an atomically smooth film morphology [2, 61, 62]. Up to 2.5 ML may be incorporated into an interfacial $Mg_2Si(111)$ template layer [62]. The deposition rate of Mg was calibrated by measuring the attenuation of the Si

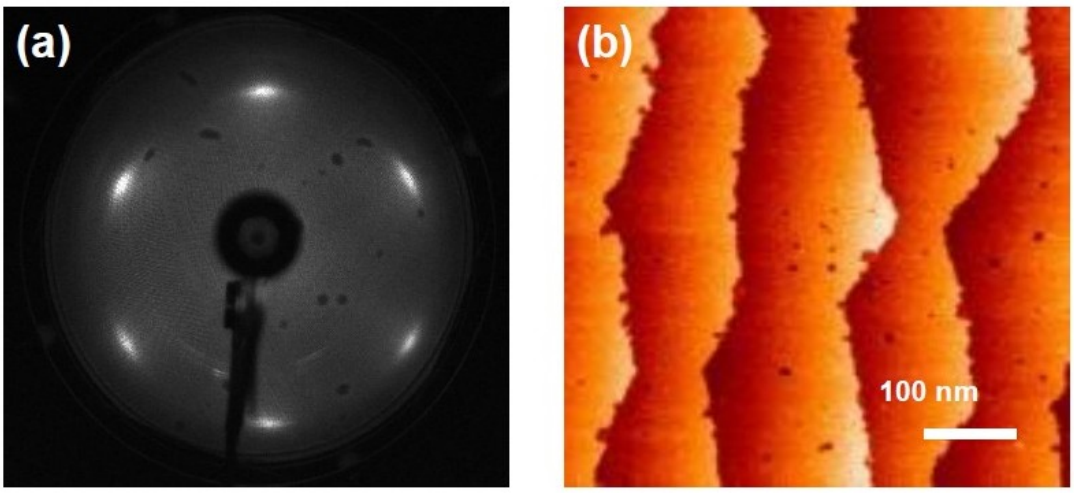


Figure 4.1: (a) LEED pattern and (b) STM image of a 6 ML Mg film after annealing to 200 K.

LVV peak-to-peak Auger signal as a function of the deposition time, using a combined retarding field LEED/AES system (see Chapter 3).

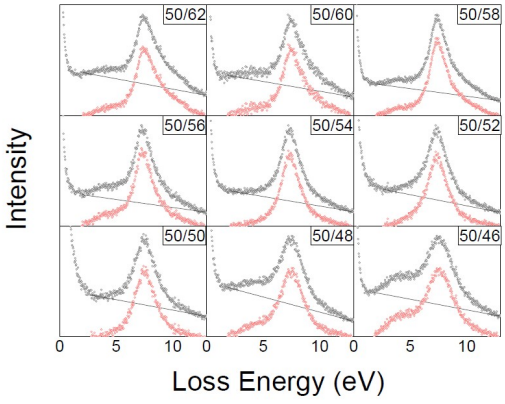
To conduct our plasmon studies on atomically smooth films, we deposited Mg onto a Si(111)-7×7 substrate at 120 K and slowly warmed the sample to room temperature in about 10 hours. All data were acquired at room temperature. LEED indicated the growth of a crystalline Mg(0001) film, as shown in Figure 4.1(a), while the absence of vibrational excitations from typical molecular adsorbates in HREELS indicated that

the surface remained clean. Complementary scanning tunneling microscopy images (Figure 4.1(b)), recorded in a different vacuum chamber on films grown using the same procedure, confirm the atomic-smoothness of the Mg films [61]. By tracing the evolution of the LEED pattern and EEL spectra over time, we found that there is a critical film thickness ($\sim$ 3 ML) above which the film could survive for more than two days at room temperature. Thinner films ultimately transform into a thin $Mg_2Si(111)$ interfacial layer at this temperature partly because of the in-plane lattice mismatch (Mg(0001): 3.21$\AA$ *vs.* Si(111):3.84$\AA$). A detailed discussion of the silicide formation is available elsewhere [62].

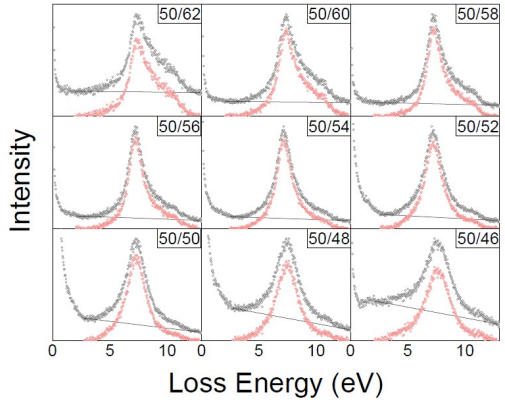
A LK2000 HREELS system was used to collect the energy-loss spectra as a function of scattering angle. The momentum transfer $\hbar q_{\parallel}$ can be calculated from the scattering angle, according to $\hbar q_{\parallel}=\sqrt{2mE_i}\sin\theta_{in} - \sqrt{2m(E_i - E_{loss})}\sin\theta_{sc}$, where θ_{in} and θ_{sc} are the angles of the incident and scattered electron beams, respectively, relative to the sample normal. E_i and E_{loss} are the incident beam energy (30 eV) and loss energy, respectively, and m is the free electron mass. Spectra were recorded at RT with an overall instrumental resolution of 30 meV.

4.2 Plasmon excitations in ultrathin Mg(0001) films

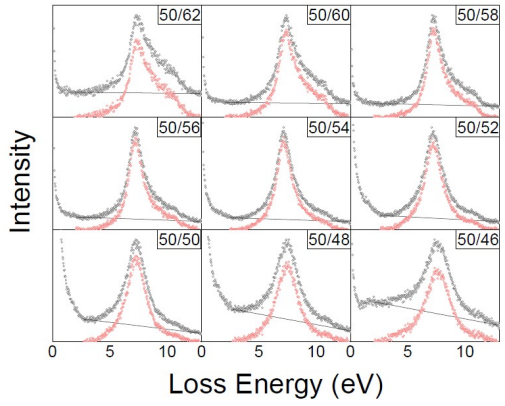
A casual inspection of the raw EELS data (Figures 4.2) shows that the lineshape exhibits subtle variations as a function of scattering angle and thickness. Figure 4.3 shows selected EEL spectra obtained from a nominally 4.5 ML thick Mg film for different scattering angles and a fixed incident angle of 50°. The tails near 0 eV belong to the elastic peak. Each spectrum is composed of multiple contributions, including a main peak at 7.2-7.5 eV, a shoulder at 4-5 eV, and a tail at 9-11 eV, respectively. The most prominent spectral feature at 7.2-7.5 eV loss energy corresponds to the (monopole) surface plasmon (SP) mode. The highest loss-energy contribution around



(a)



(b)



(c)

Figure 4.2: Spectra of (a) 4.5 ML, (b) 7.5 ML and (c) 12 ML Mg films before (black circle) and after (red circle) linear background subtraction. Incident/scattering angle is represented by "θ_{in}/θ_{sc}".

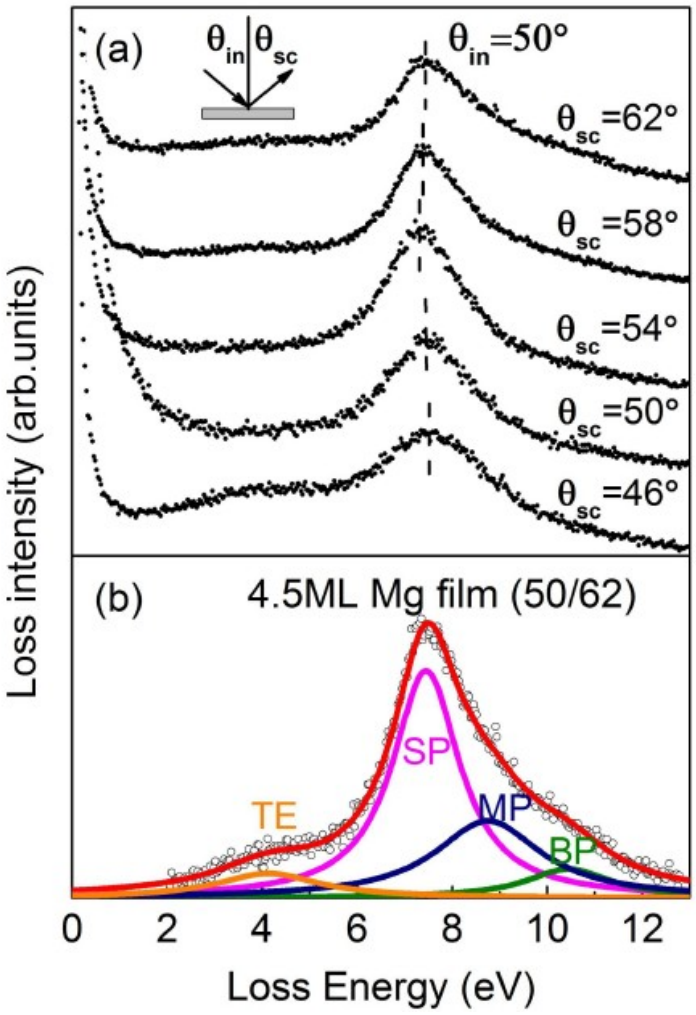


Figure 4.3: (a) EEL spectra of a nominally 4.5 ML thick Mg film at different scattering angles and 50° incident angle. The apparent broadening of the elastic tail at 50° scattering angle is due to the fact that the scattering is specular in this particular geometry. (b) Fitting of the 4.5 ML Mg film spectrum at one specific scattering angle (corresponding to $q_{\|} \approx 0$ for the surface plasmon), after subtraction of a linear background. Components TE, SP, MP and BP correspond to threshold excitation, monopole surface plasmon, multipole surface plasmon, and bulk plasmon, respectively.

10.4 eV is the bulk plasmon (BP). The energies of the SP ($\hbar\omega_s$) and BP ($\hbar\omega_p$) of the Mg film are close to those of a semi-infinite system [82]. The spectral intensity near 9 eV, in-between the SP and BP peaks, is attributed to the multipole surface plasmon (MP). This mode appears at a loss energy of about 0.8 ω_p, and has been observed

in EEL spectra of a Mg(0001) single crystal [82], and in alkali metal films [90]. The small but non-negligible contribution at 4-5 eV is attributed to the *photoemission threshold excitation* (TE), a single particle excitation that is strongly enhanced by collective interactions [52, 39]. All spectra in this study were fitted with these four components, reflecting the fact that the loss spectra are qualitatively similar to that of the bulk Mg(0001) surface. This is quite remarkable, considering the fact that the single particle spectra of these films are strongly quantized [2].

Because the peaks strongly overlap, a reliable fitting procedure is necessary to determine the energies and intensities of the various excitations as a function of thickness and parallel momentum. After subtracting a linear background from the raw data, the following procedure was employed for the consistent fitting, starting from the thick film (15 ML):

(1) We began by fitting the spectrum with θ_{in}=50°/θ_{sc}=62° , where the four contributions (TE, SP, MP, and BP) are easily recognizable by eye. Fitting parameters included peak energy, linewidth, and intensity for each peak, and a baseline. We used Lorentzian lineshapes for all four peaks. All parameters were relaxed, and the least-squares fittings were iterated until the optimized values were determined.

(2) For fitting the θ_{sc}=60° spectrum, we used the optimized fitting parameters determined from the θ_{sc}=62° spectrum as initial trial parameters. First, the parameters for the SP and BP peaks were optimized while those for the TE and MP peaks were kept fixed. The rationale of this first step is that the SP is the main contribution to the loss spectrum. Then, the TE intensity and all parameters (energy, linewidth and intensity) for the MP as well as the baseline were relaxed for optimization, while the other parameters were fixed. In the next round, the parameters of the SP and BP, as well as the intensities of the TE and MP were all relaxed for optimization while the energies and linewidths of the MP and TE remained fixed. We kept the energy and the linewidth of the TE fixed to the values determined from the fitting of the θ_{sc}=62° spectrum. It was necessary to keep consistency in

deducing the thickness dependence of the other parameters because the TE was rather broad. At the final stage, all the parameters except for the energies and linewidths of the SP and BP were relaxed for the optimization. The results were little affected by the variations of the energies and linewidths of the TE and MP.

(3) The spectrum for the next closest scattering angle was fitted by using the fitting parameters determined from the previous angle spectrum as initial trial parameters (*i.e.*, the θ_{sc}=60° parameters were used for fitting the θ_{sc}=58° spectrum, then the θ_{sc}=58° for θ_{sc}=56°, and so on). The same procedures as (2) were followed.

Once the fitting procedure for 15 ML was completed, the same procedure [steps (1)-(3)] was employed for the other films (in an order of decreasing thickness: 12 ML, 9 ML, 7.5 ML, 6 ML, 4.5 ML). In order to fit θ_{sc}=62° spectrum of the given thickness, the parameters optimized for the thicker film in the previous stage were used as trial fitting parameters in step (1). In Figure 4.4, the fitted spectra of 4.5 ML, 7.5 ML, and 12 ML Mg films at $\theta_{in}/\theta_{sc} = 50°/62°$ ($q_{\|} \approx 0$ for the surface plasmon) are displayed and compared. The non-monotonic changes in the intensities of TE and MP are observable. The energy dispersions of all four peaks (TE, SP, MP, BP) determined from the fitting are shown in Figure 4.5. Note the bulk plasmon (BP) intensity is relatively low but overall it shows positive dispersion. The multipole plasmon (MP), however, exhibits negative dispersion for small $q_{\|}$. For ultrathin alkali metal films, the negative dispersion of the MP mode was attributed to the anti-crossing behavior of the various plasmon modes. Specifically, Liebsch has shown that in ultrathin alkali metal films on Al, the MP exhibits negative dispersion due to its interaction with the "bulk"mode of the film [53]. The downward dispersing MP mode in the alkali films eventually morphs into the ordinary monopole surface plasmon with positive dispersion at large $q_{\|}$. Note, however, that in contrast to the alkali case we observe both modes (SP and MP) in the limit of $q_{\|} \to 0$. Moreover, in the thick film limit, the dispersion of the MP is positive for the alkali metals [52, 90] whereas it remains negative in the case of Mg. This qualitatively different behavior is not understood and most likely requires explanation beyond the simple jellium model. Figure 4.6 provides

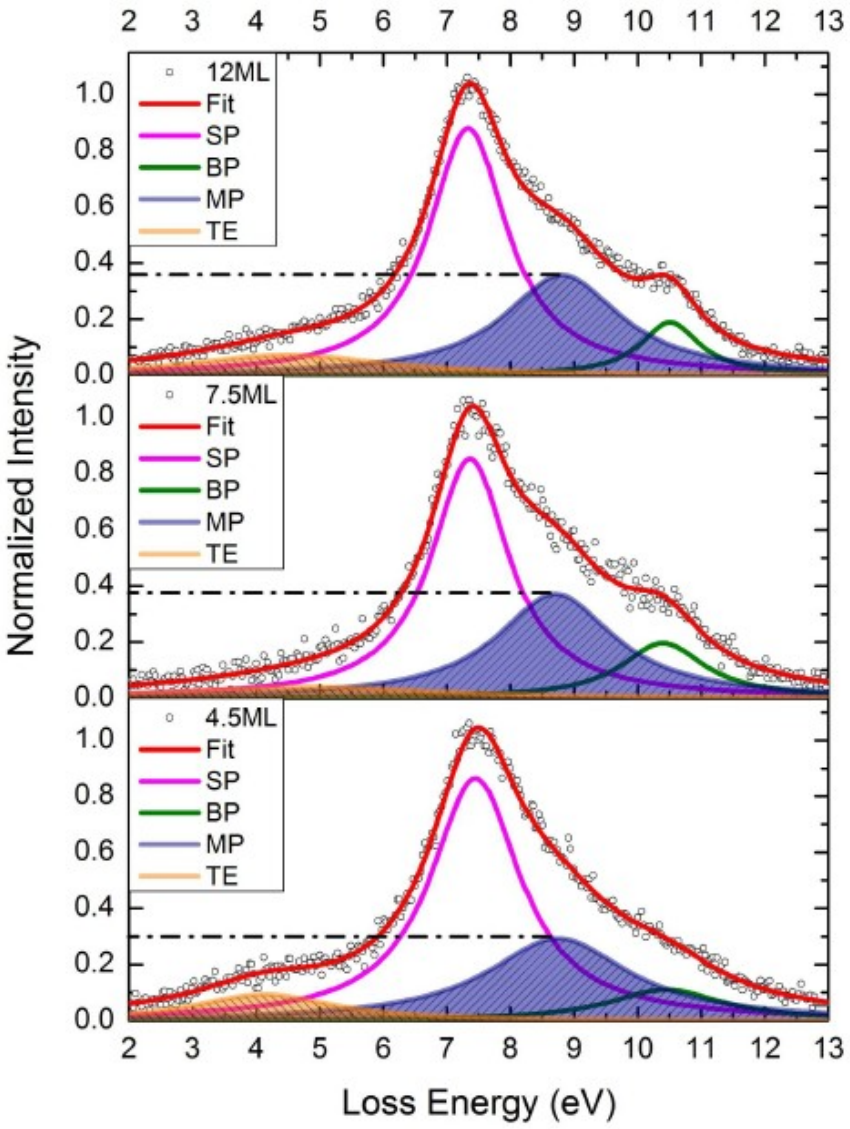


Figure 4.4: Fitted spectra of 4.5 ML, 7.5 ML and 12 ML Mg films at $\theta_{in}/\theta_{sc} = 50°/62°$.

a more detailed look of the SP dispersion, $\omega_s(q_{\|})$ for selected film thicknesses. As the film thickness decreases, the SP energy near $q_{\|} = 0$ increases monotonically. This monotonic blue shift with decreasing film thickness has also been observed for, *e.g.*, Al and Ag on Si(111) [102, 100]. This can be attributed to the interaction between the SP, localized at the vacuum/Mg interface, and the interface plasmon. As the film becomes thinner this interaction increases, pushing the SP to higher energy. This is a

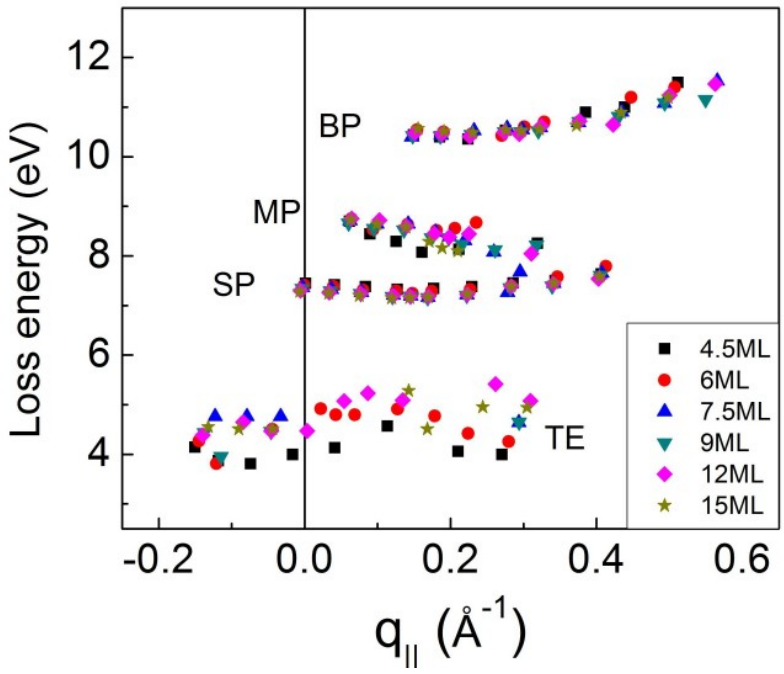


Figure 4.5: Loss energies of 4 components as a function of $q_{\|}$.

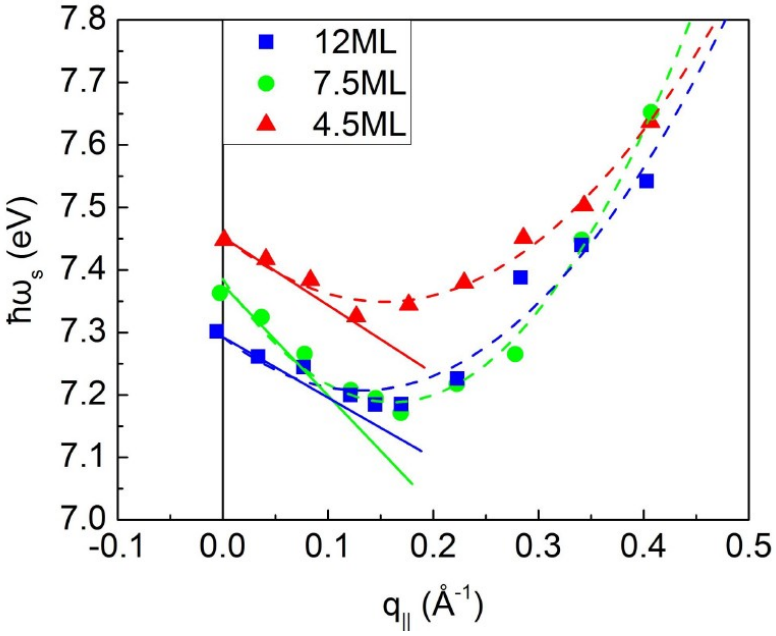


Figure 4.6: Dispersions of monopole surface plasmons in 4.5 ML, 7.5 ML and 12 ML Mg films. Dashed lines are the result of polynomial fitting. The initial dispersion slopes are indicated by solid lines.

classical confinement effect and can be captured with classical electrodynamics, *i.e.*, without invoking quantum size effects [102].

The SP dispersion of the films is negative for small $q_{\|}$. Similar dispersions have been observed for a number of metal surfaces [89, 82, 18]. This behavior is rooted in the non-local dynamical response of the surface region which, in the jellium approximation, can be represented by the complex d-function [24] as discussed in Chapter 2. In the limit of small $q_{\|}$, the monopole SP disperses according to $\omega_s(q_{\|}) = \omega_s[1\text{-}q_{\|}\mathrm{Re}[d(\omega_s)/2]]$ [25, 89]. Here, $\mathrm{Re}[d(\omega)]$ is the real part of the d-function, and corresponds to the location of the centroid of the *induced* charge density at frequency ω, measured relative to the positive background edge. The negative dispersion ($\mathrm{Re}[d(\omega_s)] > 0$) indicates that the induced charges are located outside the metal. The most remarkable result is the non-monotonic thickness dependence of $\mathrm{Re}[d(\omega_s)]$, which was determined by fitting the measured SP energies with a second-order polynomial function in $q_{\|}$. The results for $\mathrm{Re}[d(\omega_s)]$ are shown in Fig. 4.7(a). $\mathrm{Re}[d(\omega)]$ increases up to 7.5 ML and decreases again up to 12 ML. This non-monotonic variation cannot be attributed to a classical confinement. Instead, it is directly related to the *quantum* confinement effect. The surface plasmon linewidth of a Mg single crystal as a function of $q_{\|}$ is displayed in Figure 4.8(a) [82] while the corresponding results for Mg films are shown in Figure 4.8(b). An initial negative dispersion (up to 0.1 Å) is observable in both figures. However, we notice that the linewidth shifts to higher value in thinner films. This blue shift in surface plasmon linewidth may be due to the enhanced surface scattering in the thin films.

Similar thickness-dependent variations are also present in the intensities of the MP and TE peaks. Figures 4.7(b) and (c) show the intensities of the MP and TE peaks determined by the four-component fitting of the spectra. The MP intensity grows as the thickness increases from 4.5 ML to 7.5 ML. Beyond 9 ML, the intensity decreases reaching a minimum at 12 ML and then increases again. This non-monotonic variation

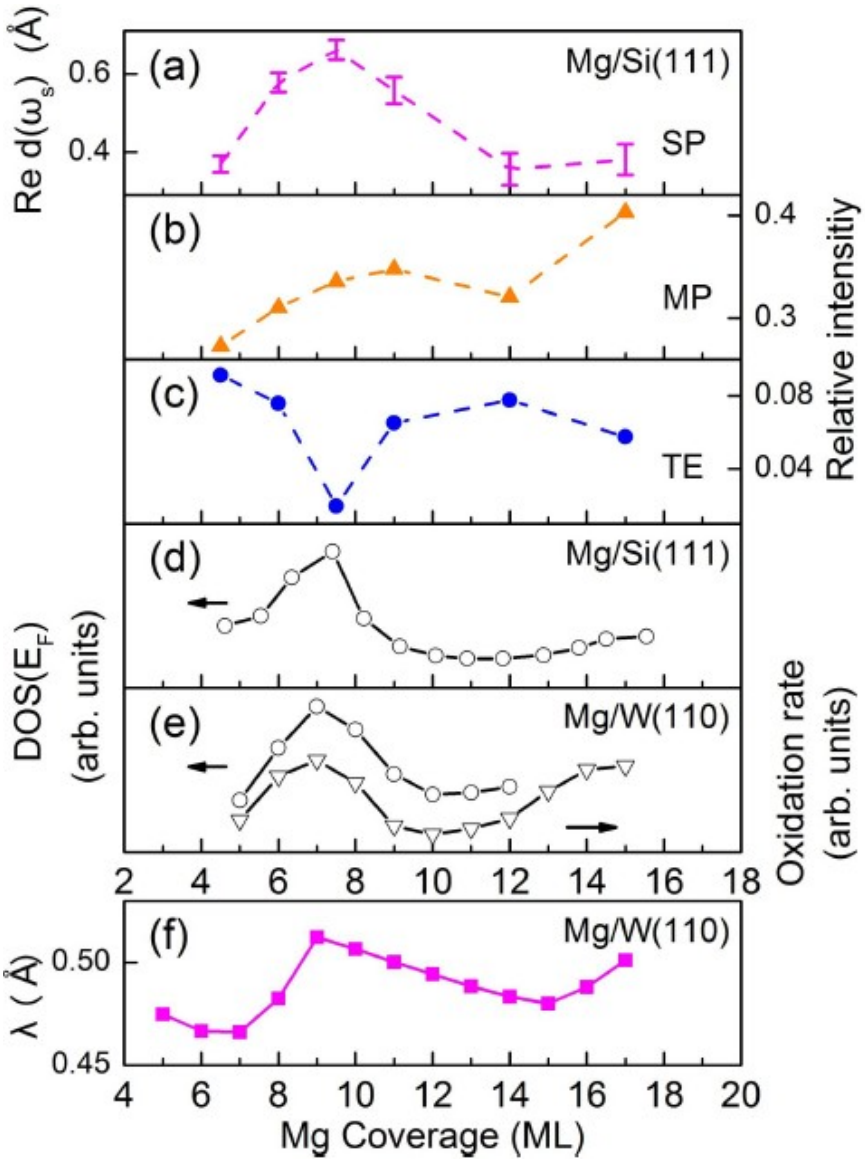


Figure 4.7: Thickness dependence of (a) the real part of $d(\omega_s)$; (b) the multipole mode intensity; and (c) the threshold excitation intensity. The intensities of the spectra in (b) and (c) are normalized by the total loss intensity; (d) Photoemission intensity at E_F in normal emission, or DOS(E_F), from Ref. [1]; (e) DOS(E_F) and initial oxidation rate of ultrathin Mg(0001) films on W(110) from Ref. [3]; (f) Charge spilling parameter λ from first-principles calculations for Mg(0001) on W(110) [13].

of the MP intensity follows that of Re$[d(\omega_s)]$. In contrast, the TE intensity anti-correlates with the MP intensity: as the MP intensity increases, the TE intensity diminishes, and vice versa.

For comparison, the thickness dependence of the normal-emission photoelectron intensity near the Fermi level E_F (which is proportional to the Density of States at Γ) of Mg(0001) films on Si(111) [1] and on W(110) [3] are reproduced in Figures. 4.7(d) and (e), respectively. Also shown in panel (e) is the initial oxidation rate of the films, as measured with core level photoemission during controlled oxygen exposure experiments [3]. Notice the remarkable coincidence of the oscillatory thickness dependences of the different quantities in the three studies.

The excellent correlation of the thickness-dependences of the surface electronic excitations in EELS in Figure 4.7(a)-(c), the DOS(E_F) in panels (d) and (e), and the surface reactivity in panel (e), suggests the existence of a common origin governing these oscillatory phenomena. The oscillations in the DOS(E_F) and surface reactivity of Mg(0001) films on W(110) have been explained by the quantum size effect [13]. Specifically, as the film thickness L increases, additional quantum well subbands drop below E_F. The charge spilling of the 2D subband system reaches a maximum when

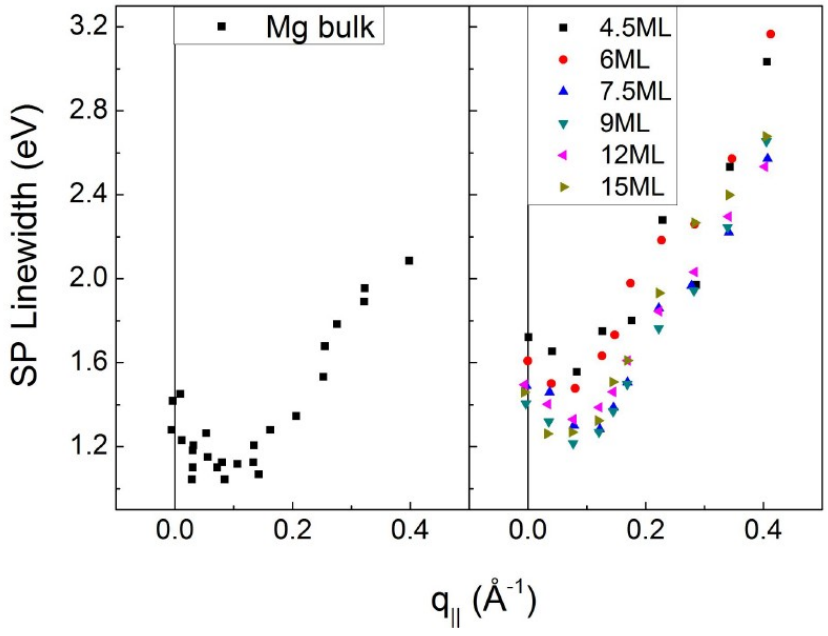


Figure 4.8: Surface plasmon linewidths as a function of $q_{\|}$ for Mg single crystal [82] (left panel) and films (right panel).

the bottom of a subband drops below E_F. In the case of Mg(0001), this happens at 8 ML intervals (Figure 4.7(d))[3, 13]. The oscillatory charge spilling leads to oscillations in the oxidation rate as the electron transfer rate between the oxygen molecule and metal depends exponentially on λ [13]. The thickness dependence of the charge spilling parameter λ, calculated from first-principles [13], is shown in Figure 4.7(f). Here, the oscillations of λ and of the theoretical DOS (not shown) are phase shifted by 2 ML, relative to those in panels (a)-(e). The 2 ML phase shift between theory and experiment was attributed to epitaxial strain in the latter [13]. Because EELS is also sensitive to the charge density profile at the surface, we hypothesize that quantum confinement effects on the charge spilling are responsible for the non-monotonic variations of the SP dispersion coefficient as well as the intensity variations of the MP and TE.

4.3 Phenomenological model

In order to test this hypothesis, we calculated the EEL spectra using the complex d-function of semi-infinite jellium [52] which employs TDLDA. We emphasize that the jellium model quite adequately descibes the plasmon features of simple metal surfaces such as Mg(0001). Here, we specifically consider the role of charge spilling. Changing the thickness L of the film periodically changes the charge penetration length λ, due to the quantum size effect [13]. The effect can be understood as follows. As the thickness L of the film increases, more and more 2D subbands sink below the Fermi level. In the simple square well model, the vacuum decay length of the n^{th} subband is given by

$$\lambda_n \sim 1/\sqrt{V_0 - \frac{\hbar^2 n^2 \pi^2}{2mL^2}}, \tag{4.1}$$

where V_0 is the surface barrier. Hence λ exhibits a maximum when the bottom of the band appears at E_F. As the thickness increases, λ decreases until a new subband drops below E_F. For Mg(0001), this happens once every 8 ML [2, 3, 13]. The

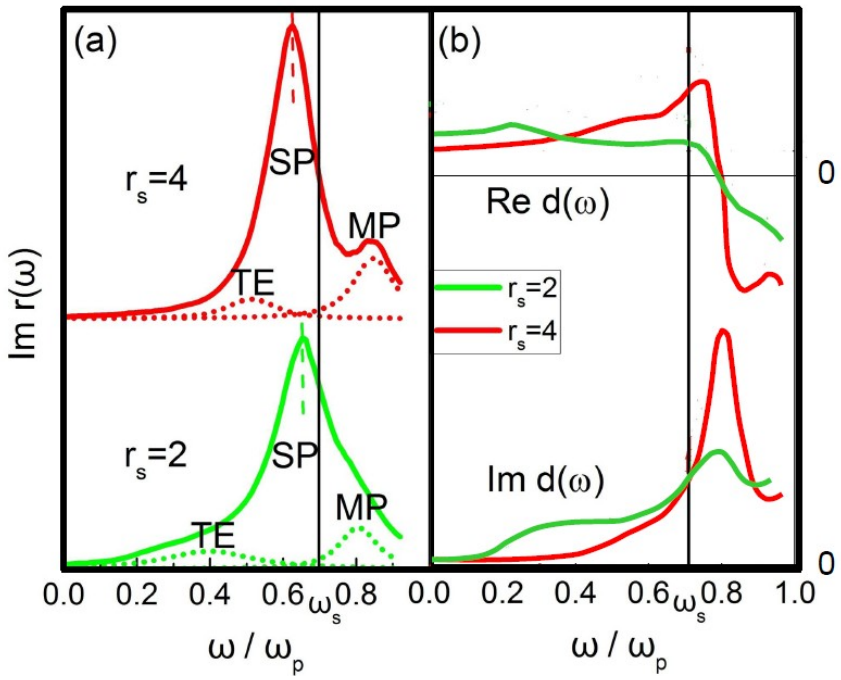


Figure 4.9: (a) Imaginary parts of calculated surface reflection coefficients for r_s=2 (green) and r_s=4 (red) with $q_{\|} = 0.12\mathring{A}^{-1}$ and $\gamma = 0.1\omega_p$. The TE and MP contributions, determined via a least-squares fit of the calculated loss spectra, are indicated by the dotted lines. Note the relative redshift of the SP peak for r_s=4, consistent with Figure 4.6; (b) Real and imaginary parts of surface dielectric *d*-functions for r_s=2 (green) and r_s=4 (red), adopted from [52]. Vertical lines mark the SP energy of bulk Mg, $\omega_s = \omega_p/\sqrt{2}$.

thickness-dependent oscillation of λ can be mimicked by an oscillation of r_s. For films with a thickness corresponding to the minimum decay length λ_{min}, we assume a jellium ground state with $r_s = 2$ (*i.e.*, high electron density). For films with a thickness corresponding to the maximum decay length λ_{max}, we choose the jellium ground state with $r_s = 4$, *i.e.*, low electron density. The Lang-Kohn charge density profiles for these values of r_s [46] are similar to those computed *ab-initio* by Binggeli and Alterelli as a function of the film thickness [13]. Of course, the electron density in the interior of the film doesn't change. We only assume that charge density profile at the surface can be modeled this way. Therefore, in the calculation of the surface loss spectrum for the different values of r_s, all energies will have to be scaled relative to the corresponding values of ω_p. Again, the underlying assumption is that the

quantum size effects on the loss spectra are dominated by the quantum size effects on the surface charge density profile and can thus adequately be described using the d-function formalism. The EELS signal is then taken to be approximately proportional to the imaginary part of $r(\omega, q_{\parallel})$, the non-retarded (${q_{\parallel}}^2 \gg \omega^2\varepsilon/c^2$) reflection coefficient for p-polarized light, given by [24, 41]

$$r(\omega, q_{\parallel}) = \frac{[\varepsilon(\omega) - 1][1 + q_{\parallel} d(\omega)]}{\varepsilon(\omega) + 1 - [\varepsilon(\omega) - 1] q_{\parallel} d(\omega)}. \tag{4.2}$$

This expression is valid for $q_{\parallel} d(\omega) \ll 1$ and $q_{\parallel} L \gg 1$. Here, the complex bulk dielectric constant $\varepsilon(\omega)$ is given by

$$\varepsilon(\omega) = 1 - \frac{\omega_p^2}{\omega(\omega + i\gamma)}, \tag{4.3}$$

where γ is the damping parameter. Figure 4.9(a) shows the surface loss functions calculated from Equation (4.2) for two different charge spillings (λ_{min} with $r_s = 2$ and λ_{max} with $r_s = 4$) with $q_{\parallel} = 0.12 \mathring{A}^{-1}$ and $\gamma = 0.1\ \omega_p$. The values of $d(\omega)$ used in Equation (4.2) and shown in Fig. 4.9(b) were adopted from [52]. Notice that the MP in Im$[d(\omega)]$ as a resonance near $0.8\ \omega_p$, while the SP does not appear in Im$d(\omega)]$ [52].

The calculated loss spectra (Figure 4.9(a)) reproduce the experimental trend in Figure 4.7 quite well. The experimental spectra are obtained for a specific scattering angle, while the calculated spectra are obtained for a specific momentum transfer. The anti-correlation between the TE and MP intensities is independent of $q_{\parallel}$. Note that the singularity in $d(\omega)$ at ω_p [40] is suppressed in the calculated surface loss function because $\varepsilon \to 0$. Therefore the experimental EELS shows only a very weak BP contribution, somewhat enhanced by impact scattering of electrons penetrating the bulk.

Because Re$[d(\omega_s)]$ is largest for $r_s = 4$ (Figure 4.9(b)), the corresponding SP energy (say at the minimum near $q_{\parallel} = 0.12 \mathring{A}^{-1}$) is lowest for $r_s = 4$, *i.e.*, for the

largest value of λ. Notice also the slight broadening of the SP mode for $r_s = 2$. It can be shown that the SP linewidth is proportional to Im $d[\omega_s(q_\parallel)]$ [*]. The loss spectrum for $r_s = 2$ shows a relatively small MP component, which shows up more clearly for $r_s = 4$. The TE is the broad feature on the low-energy side of the SP peak near $0.4\omega_p$. It is clearly visible for $r_s = 2$, but becomes hardly recognizable for $r_s = 4$. Thus, all of the observed changes with film thickness in Figure 4.7 are qualitatively captured by the d-function: the SP dispersion by Re$[d(\omega)]$ and the anti-correlation between the TE and MP intensities by Im$[d(\omega)]$.

4.4 Conclusion

This work clearly establishes the existence of quantum-size effects on the plasmon and photoemission threshold excitations (see Figure 4.10). The bulk-like identities of the plasmon excitations (SP, MP and BP) are well maintained down to 4.5 ML (and possibly thinner if counted from the silicide interface). This is remarkable. The anticipated transition with increasing film thickness from single particle-like intersubband transitions to the increasingly collective response in the thick film limit was not observed. We conjecture that the dynamical screening response of quantum confined Mg films becomes bulk-like when the electron density in the film approaches the bulk limit. This could occur as soon as a second Mg(0001) layer is formed. *Ab-initio* quantum-mechanical calculations of the dynamical response of crystalline Mg films on Si(111), taking the atomic coordinates and band structure into consideration, may shed more light on this aspect.

[*]The spectral function is Lorentzian-like near SP frequency.

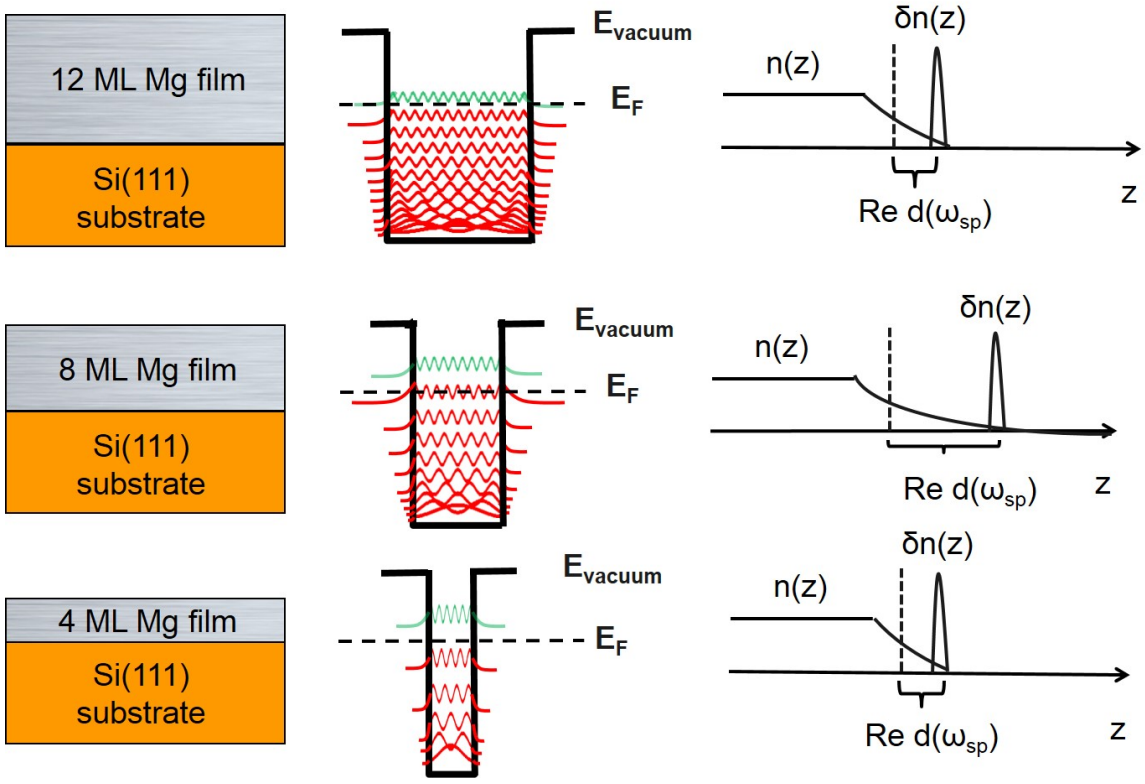


Figure 4.10: Quantum-size effects on collective plasmon excitations in ultrathin Mg(0001) films are related to the thickness-dependent charge spilling at ground state.

Chapter 5

Plasmon Excitations in Ultrathin Pb(111) Films

Epitaxial Pb(111) films have been intensively studied in the past decade because of the very strong quantum size effects in these films, which have been attributed to the nesting of the Fermi surface along the [111] growth direction [37]. Strong quantum-size effects not only facilitate epitaxial growth of high-quality crystalline Pb(111) films on Si(111) or Ge(111), but also affect the structural, chemical, and physical properties of these films, including work function and superconductivity. For an overview of these studies, we refer to a recent review article by Özer *et al.* [60]. We are especially interested in how the quantum size effect and Fermi surface nesting affect the collective excitations of these films. We begin our investigations with a study of thick Pb(111) films, which are expected to resemble the semi-infinite bulk. They provide an important benchmark for our thin film studies. We show that the EEL spectra of semi-infinite Pb(111) are very different from those of Mg(0001), exhibiting spectral features that are clearly associated with interband transitions. We pay special attention to a 2 eV excitation, which in the case of bulk Pb(111) can be attributed to an interband transition that is possibly enhanced by collective interactions. Surprisingly, the 2 eV excitation shifts to very low energy in the

ultrathin film regime. This shift could not be captured by density function theory slab calculations of the ground state band structure and RPA response. The dispersion of the low energy excitation is qualitatively consistent with that of a symmetric classical slab plasmon, resulting from the coupling between the surface plasmon and interface plasmon. Model calculations using the dielectric constant from RPA indicate that this mode saturates at 2 eV in the limit of large $q_{\|}L$. The observation of the symmetric plasmon branch in dense metallic systems is highly unusual and indicates that the coupling between the surface and interface modes remains strong up to fairly large values of $q_{\|}L$. The latter is consistent with the almost one-dimensional nature of the static screening response (Friedel oscillations) in Pb(111) films, which in turn is related to Fermi surface nesting. [37]. This fundamental new insight may be important in plasmonics where photon coupling to the symmetric branch offers distinct advantages for tuning the resonance energy and propagation length of the surface plasmon polariton.

5.1 Plasmon excitations in bulk Pb(111)

The growth rate of Pb films was calibrated by AES and the surface structure was monitored with LEED, as discussed in Chapter 3. The surface electronic excitations of Pb films were measured with REELS for a wide range of film thicknesses. The spectra of the Pb(111) films no longer change beyond 40 ML, indicating that the spectra of the 40 ML film represent those of semi-infinite Pb(111). Overall, the lineshapes and intensities of the energy loss spectra vary noticeably with detection angle, but the peak positions hardly disperse. The bulk plasmon (13 eV) was not observed.

In 40 ML (and 160 ML) thick Pb(111) films, three loss features can be observed. They are located at 2 eV, 7 eV, and 10 eV, respectively (see Figure 5.1). Interestingly, the loss intensities recorded along the Γ-K and Γ-M direction are quite different. To understand the origins of these energy losses, we performed TDDFT calculations within the framework of an LAPW ground state calculation as implemented in the

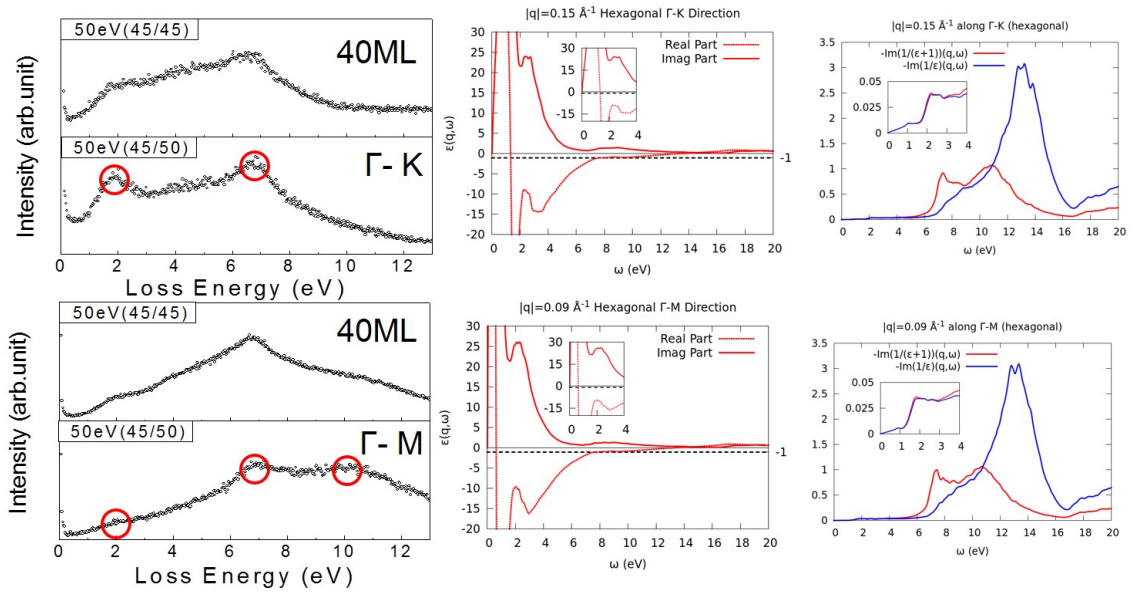


Figure 5.1: The HREEL spectra, dielectric functions and loss functions for thick Pb(111) films along Γ-K (upper panels) and Γ-M (lower panels) directions. Distinct energy loss features at 2, 7, and 10 eV are circled in red [unpublished, A. Teng, R. Van Wesep *et al.*]. The loss intensities recorded along the Γ-K and Γ-M direction are quite different. This is not captured by TDDFT calculations within the framework of LAPW. The middle panel shows two features near 2 eV and 8 eV in the imaginary part of the dielectric function. Those are "absorption bands"associated with interband transitions. Note the relatively strong intensity of the 2 eV excitation in EELS is not reproduced in the RPA response calculation.

Elk platform. The middle panel of Figure 5.1 shows two features near 2 eV and 8 eV in the imaginary part of the dielectric function. Those two "absorption bands"are associated with interband transitions. Because the imaginary and real parts of the dielectric function are connected by the Kramers-Kronig relations, the real part of dielectric function bends toward -1 and thus exhibits resonances in the surface loss function at about 7 and 10 eV, as shown in the right panel of Figure 5.1. Interestingly, the relatively strong intensity of the 2 eV excitation in EELS is not reproduced in the RPA response.

The momentum dispersion of the 2 eV excitation is shown in the left panel of Figure 5.2. Here, we have chosen a larger incident angle (with respect to surface normal) and a lower beam energy to obtain better energy resolution and better surface

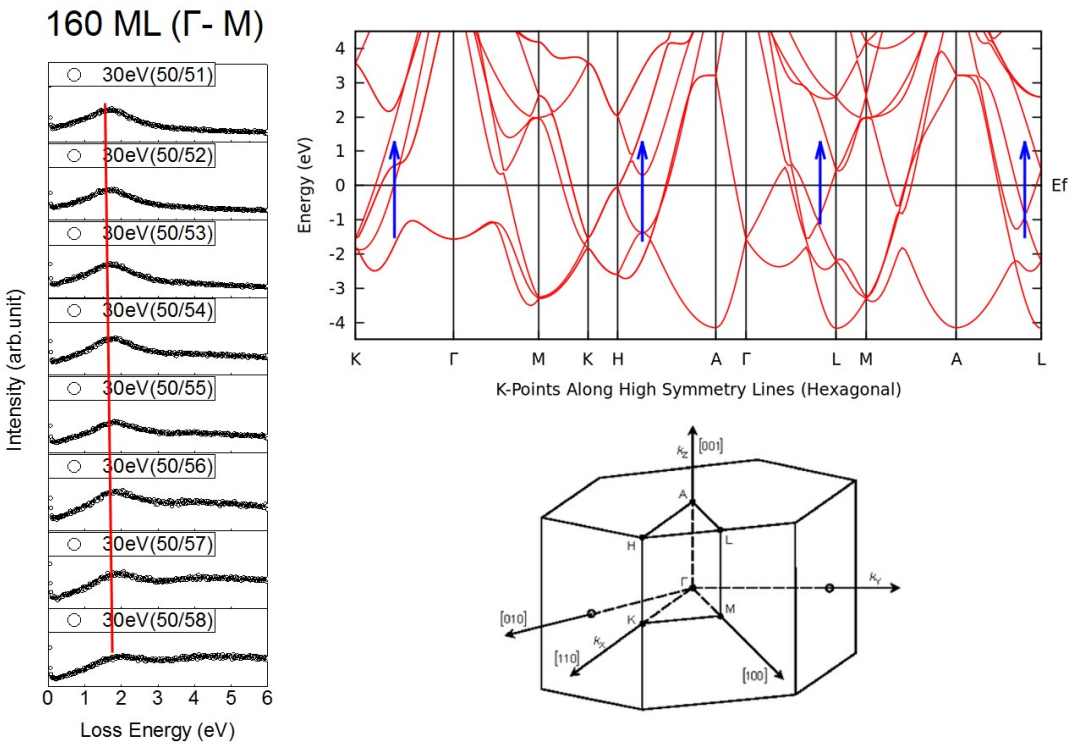


Figure 5.2: The HREEL spectra of the 2 eV peak (left panel); The calculated band structure of bulk Pb(111) (right panel).[unpublished, A. Teng, R. Van Wesep *et al.*] The arrows mark the regions in momentum space where the energy separation between the initial and final state bands amounts to roughly 2 eV.

sensitivity. Note that the loss peak hardly disperses, suggesting that if the excitation were due to interband transitions, one must be able to identify regions in momentum space where the energy separation between the initial and final state bands amounts to roughly 2 eV (many k-points are needed to account for the relatively strong oscillator strength of the 2 eV excitation in EELS). In other words, one must look for parallel sectors in the band structure. Figure 5.2 shows the band structure of bulk Pb in a hexagonal setting, calculated using the LAPW code. Vertical arrows indicate transitions between parallel bands that could contribute to the 2 eV excitation in bulk Pb. However, it is unlikely that these interband transitions fully account for the strong EELS feature at 2 eV because they are swamped by the collective excitations

in the RPA response. This signals an important discrepancy between RPA and the measured loss spectra.

5.2 Plasmon excitations in ultrathin Pb(111) films

In ultrathin Pb(111) films, the loss features at 7 eV and 10 eV persist down to 5 ML. This is consistent with TDDFT results for free standing slabs in which the peak positions do not show appreciable thickness dependence. However, the low energy (2 eV) excitation shifts to 0.3 eV and exhibits positive linear momentum dispersion for the 8 ML film (see Figure 5.3). This excitation can no longer be traced in thinner films, as it begins to merge with the elastic peak. The "softening"of the low energy excitation is remarkable, as this continuous redshift of the 2 eV excitation with diminishing film thickness rules out an interpretation in terms of interband transitions. Our DFT and TDDFT slab calculations do not caputure this redshift (Figures 5.4). A close look at the HREEL spectra of a 10 ML Pb(111) film, recorded along the Γ-K direction, furthermore indicates the emergence of a new loss feture between 3 eV and 4 eV, which becomes the dominant loss feature at larger $q_{\|}$ (Figure 5.5). In Figure 5.6, we compiled all of our data concerning this low energy feature into a single plot, where we plot the loss energies as a function of $q_{\|}L$. While the plot is quite noisy due to the difficulty in extracting the precise peak positions when lineshapes are changing rapidly, the data seem to collapse onto a single curve, except for the thickest films. This strongly suggests that the redshifting loss feature in these films represents the symmetric plasmon branch, resulting from the coupling between the surface and interface plasmons. In the following section, we use a phenomenological model to test this scenario of interface plasmon coupling, using the loss function of a thin metal slab, sandwiched between two dielectric media [26, 74].

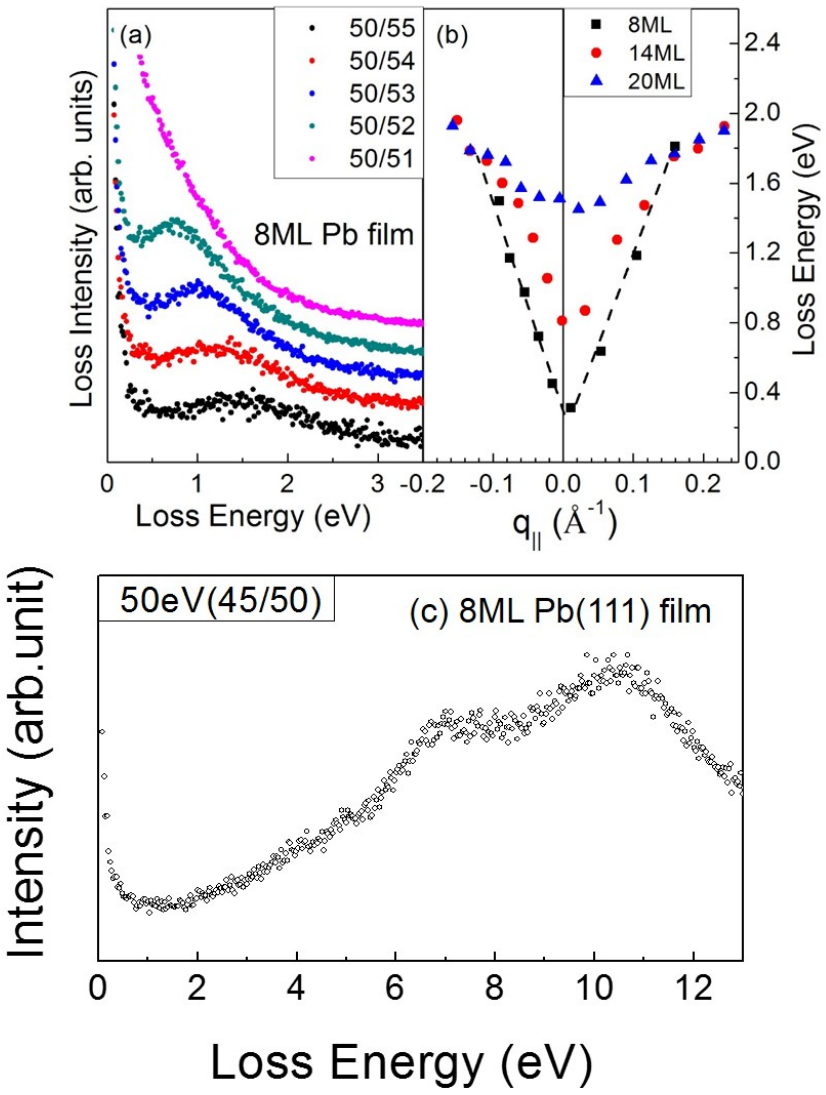


Figure 5.3: (a) Dispersion of the low energy excitation in 8 ML Pb(111) film; (b) Dispersion of the low energy excitation as a function of film thickness; (c) Survey spectrum of 8 ML Pb(111) film. The low energy (2 eV) excitation shifts to 0.3 eV and exhibits positive linear momentum dispersion for the 8 ML film.

5.3 Phenomenological model

In the classical slab model [74],

$$(\varepsilon_1 q_{z0} + \varepsilon_0 q_{z1})(\varepsilon_2 q_{z1} + \varepsilon_1 q_{z2}) + (\varepsilon_1 q_{z0} - \varepsilon_0 q_{z1})(\varepsilon_2 q_{z1} - \varepsilon_1 q_{z2}) e^{2iq_{z1}L} = 0, \qquad (5.1)$$

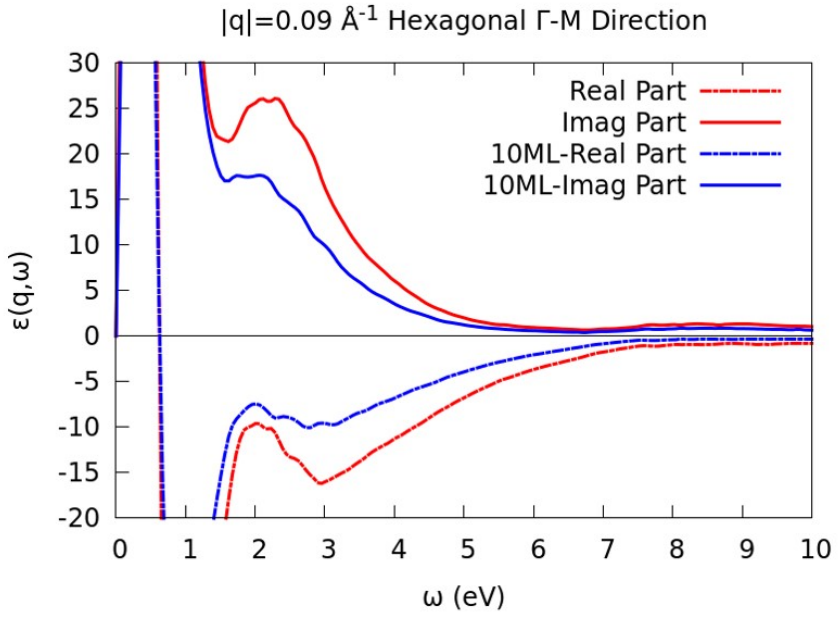


Figure 5.4: Calculated dielectric functions for Pb bulk and 10 ML Pb film.[unpublished, A. Teng, R. Van Wesep *et al.*] There is no significant shift of absorption peak in 10 ML Pb film.

where q_{zi} and $q_{\|}$ are the components of the wave vector $\sqrt{\varepsilon_i}\omega/c$, with

$$q_{\|}^2 + q_{zi}^2 = \varepsilon_i(\omega/c)^2. \tag{5.2}$$

Using $\varepsilon_0 = 1$ (vacuum), $\varepsilon_2 = 16$ (Ge), and assuming $c \to \infty$ (in non-retarded region), we obtain

$$q_{\|}^2[(\varepsilon_1+1)(16+\varepsilon_1) - (\varepsilon_1-1)(\varepsilon_1-16)e^{-2q_{\|}L}] = 0. \tag{5.3}$$

The solution of this equation produced a complex ω. To avoid this issue, we search for pole-like structures in the reflection coefficient *

$$S = \mathrm{Im}(r) = \mathrm{Im}[\frac{-(\varepsilon_1-1)(\varepsilon_1+16) + (\varepsilon_1+1)(\varepsilon_1-16)e^{-2q_{\|}L}}{(\varepsilon_1+1)(\varepsilon_1+16) - (\varepsilon_1-1)(\varepsilon_1-16)e^{-2q_{\|}L}}], \tag{5.4}$$

*K. Kempa, private communication.

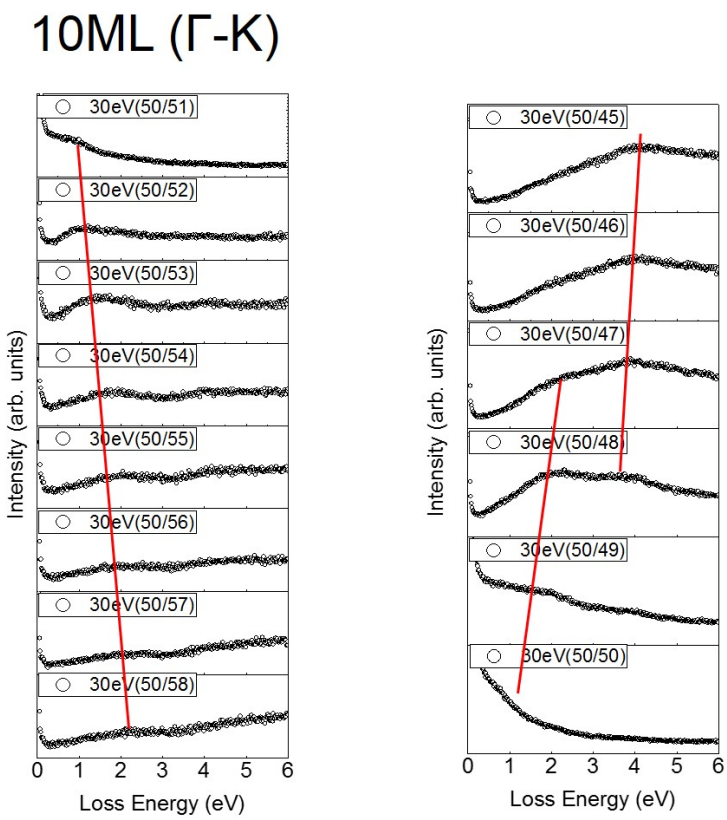


Figure 5.5: Dispersion of low energy excitations in 10 ML Pb(111) film along Γ-K direction. In the right panel, a new feature emerges at 4 eV and takes over the spectral weight at larger $q_{\|}$.

where $\varepsilon_1 = \mathrm{Re}\varepsilon_1(\omega) + \imath \mathrm{Im}\varepsilon_1(\omega)$. The dielectric function is generated from the TDDFT calculation of bulk Pb for small $q_{\|}$. The results of the modeling are shown in Figures 5.7a and 5.7b. The latter provides a magnification of the slab response in the low-energy region.

The comparison between the REELS data and the peak positions obtained from the phenomenological model is shown in Figure 5.8. Figure 5.7(b) shows a beautiful anti-crossing behavior, with the characteristic exchange of the oscillator strength [†].

As the slab plasmon (sharp peak on the low energy side of the spectrum) "walks" through the weak loss feature at 2 eV, its oscillator strength diminishes while

[†]K. Kempa, private communication.

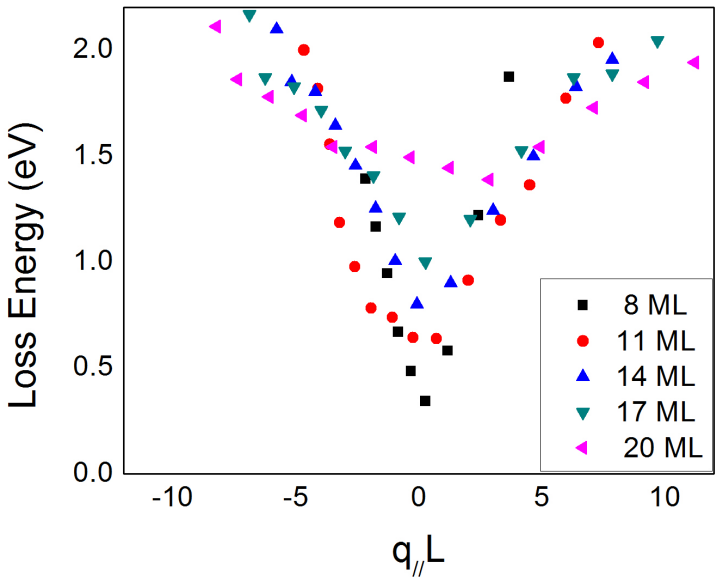
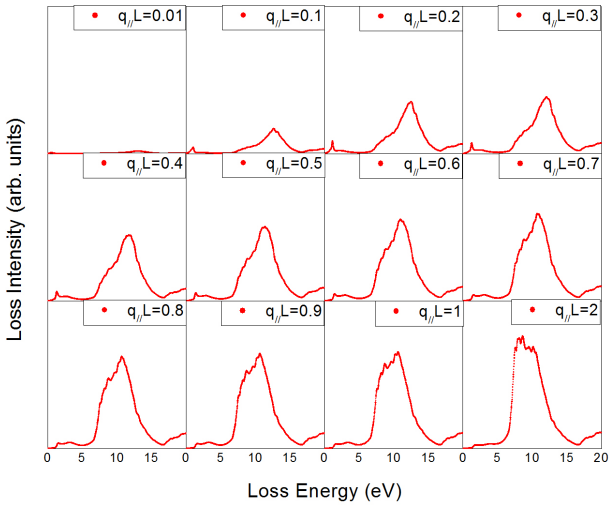


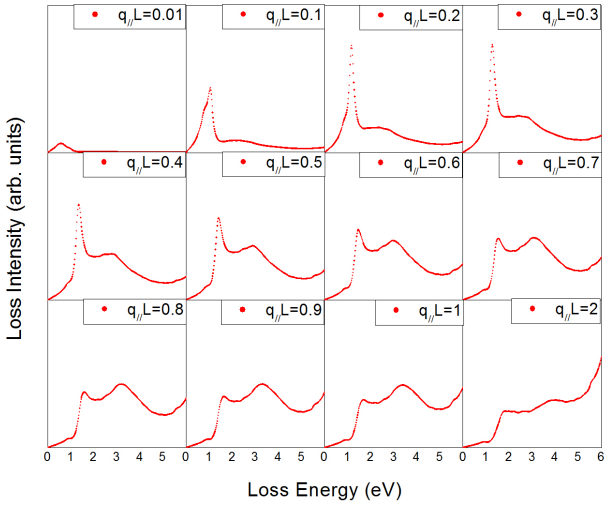
Figure 5.6: The dispersions of the low energy excitation almost collapse when plotted as a function of $q_{\|}L$.

its dispersion flattens, but the other (3 eV) peak takes over the spectral weight and acquires dispersion. This can be qualitatively understood as follows: the interband transitions appear in the dielectric function as non-dispersive Lorentzian terms near 2 eV. The real part of the Lorentzian term must cross zero between two such resonances, which means that the plasmon condition is satisfied. In situations where there are many interband transitions, there are many such plasmons, each in-between a pair of Lorentzian terms. Also, the closer the interband transitions are in energy, the less dispersive the plasmon becomes (it has "less room"to disperse) [‡]. This effect is well known in semiconductor plasmonics, as well as in metamaterials [64, 68]. On the other hand, the slab plasmon is not related to these interband transitions, and therefore it can "walk"through these interband plasmons. However, due to electron-electron interactions, they must anti-cross [64, 68]. Now, the slab plasmon has two branches (symmetric and anti-symmetric), which are hybrids of surface plasmons on opposite faces of the slab. In the case of a suspended film, both branches reach the surface

[‡]K. Kempa, private communication.



(a)



(b)

Figure 5.7: Modeled spectra of the sandwich structure: (a) 0-20 eV scale; (b) 0-6 eV scale. Note the "anticrossing"when the slab plasmon (sharp peak on the low energy side of the spectrum) "walks"through the weak loss feature at 2 eV, its oscillator strength diminishes while its dispersion flattens, but the other (3 eV) peak takes over the spectral weight and acquires dispersion.

plasmon frequency of the semi-infinite bulk for large values of $q_{\|}L$. On the other hand, in the presence of a semiconductor substrate, there is a plasmonic gap because

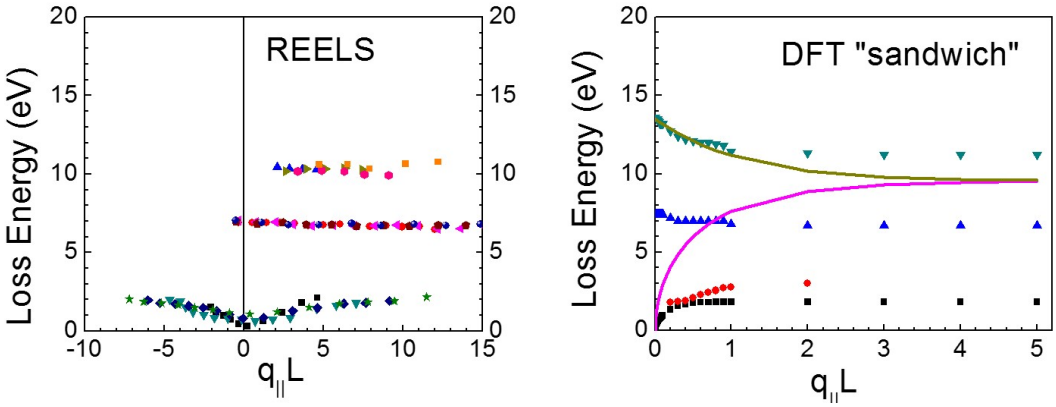


Figure 5.8: Comparison between REELS data (left panel) and the phenomenological model (right panel). The scattered data points are generated from the phenomenological model of the vacuum-metal-dielectric structure. The solid lines represent the classical symmetric and antisymmetric modes of a free standing film. The "gap opening"is due to the presence of a semiconductor substrate.

the surface plasmon on the semiconductor side of the slab (or interface plasmon), has its frequency strongly renormalized (lowered) by a factor of $\sqrt{\varepsilon_{Ge}} = 4$. Therefore, the lower branch of the slab plasmon saturates at 2-3 eV, as indicated by the simulations.

5.4 Discussion and Conclusion

The plasmon response in bulk Pb(111) is strongly affected by interband transitions. In quantum confined Pb(111) films, the low-energy feature, which in the bulk has been attributed to an interband transition, exhibits a dramatic "softening"with decreasing film thickness. This energy shift is attributed to the strong coupling between the two interface plasmons (see Figure 5.9). So far the quasi "acoustic"dispersion has only been observed for very thin slabs at very small $q_{\|}$ [20]. Perfect interfaces are also critical, which could explain why this dependency has only been observed so far in optical experiments on MBE-grown semiconductor slabs. As EELS works with large $q_{\|}$, this mode can only be observed in very thin films.

One question remains to be answered: why is the coupling between interface plasmons so much stronger in Pb(111) than in Mg(0001) or other simple metals?

One possible mechanism is Landau damping (LD) in the defect-induced spillage of the single particle continuum (SPC). The following interpretation was offered to us by Prof. Kris Kempa from Boston College.

1) The dispersion of the symmetric (lower-branch) mode is always hard to detect in "conventional"metals, in large part because it lies (in ω - $q_{\|}$ space) not far from the SPC. This proximity is important because non-perfect surfaces/interfaces break the perfect in-plane symmetry (relax the momentum conservation) thus spread-out the SPC beyond their sharply defined boundaries. The symmetric slab mode, as any acoustic-like (gapless) mode, is affected by this spillage more than the gapped anti-symmetric mode, and thus is more or less Landau damped.

2) Proximity to SPC is not the only important factor. The other is the density of available transitions for LD in SPC, which depends strongly on dimensionality. In addition, this density obviously depends on the density of states (DOS) around the Fermi surface. For the low frequency, symmetric slab mode, the LD single particle transitions occur close to E_F (from the occupied states just below E_F to empty states just above). Therefore, the available transitions for Landau damping depend on the DOS in the vicinity of E_F. In 3D, the DOS is proportional to $E^{1/2}$, thus reaching zero at the bottom of the band (far from E_F) and large at E_F. Therefore, LD (from SPC spillage) is expected to be large in 3D systems. Now, for 1D system DOS is proportional to $E^{-1/2}$, and therefore it is large at the bottom of the band (far from E_F), but small at E_F. Therefore, Landau damping is expected to be small in 1D systems.

3) For Pb(111) films it has been found that the amplitude of the Friedel oscillations along the [111] direction decreases as $1/x$, rather than the usual $1/x^2$. This indicates a 1D-like behavior of electrons in Pb [37], which has been attributed to Fermi surface nesting along [111]. Because of 1) and 2), Landau damping from SPC spillage is small in Pb(111) films, and the symmetric (lower branch) slab mode becomes visible. In contrast, by the same argument, in the "conventional"3D metals (Mg, Al, etc.),

Landau damping from SPC spillage is large, and thus it is very difficult to observe the symmetric mode.

This mechanism also explains the well known phenomenon that in the semiconductor quantum wells it has always been relatively easy to observe 2D slab plasmons, as these structures are grown via MBE, and exhibit superb interface quality (small spillage). They also involve only one or two subbands, meaning that the phase space for Landau damping is strongly reduced.

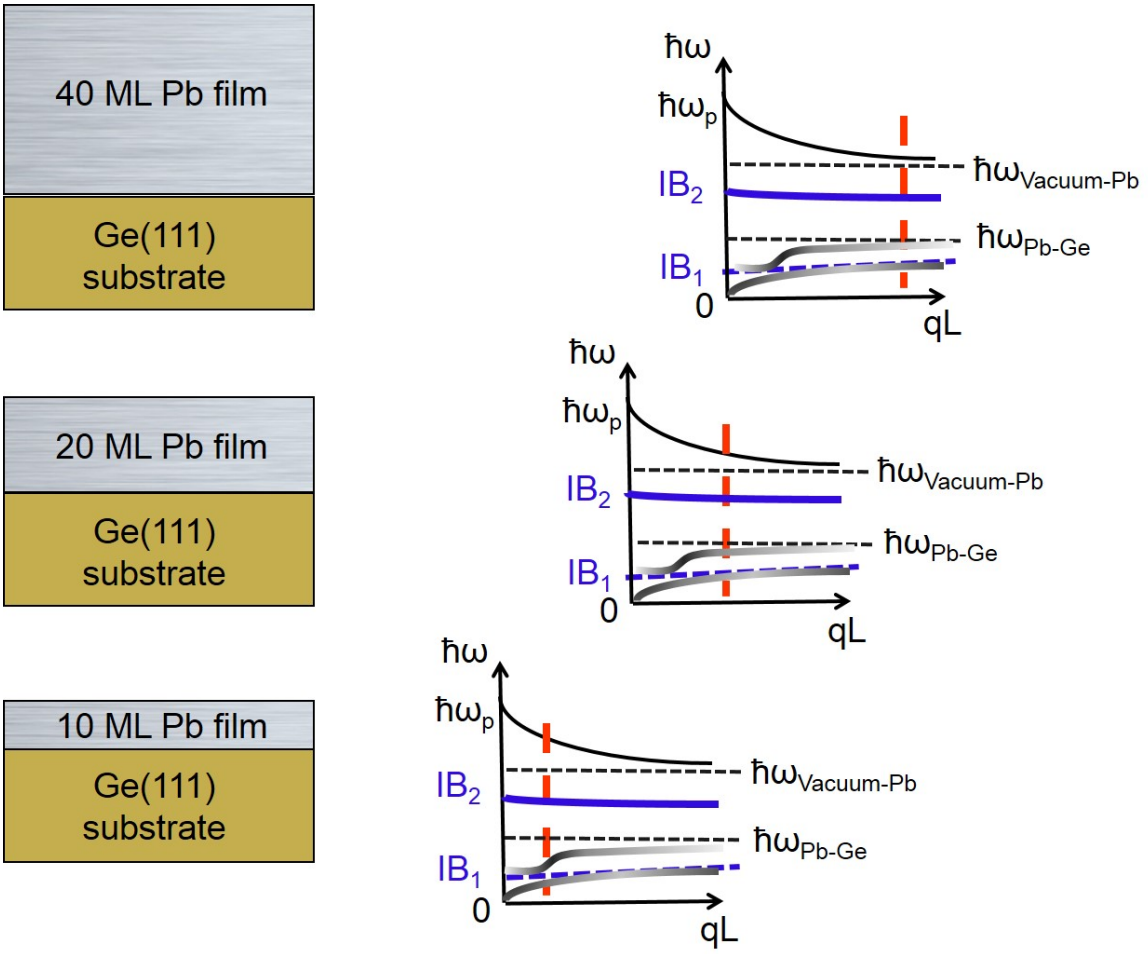


Figure 5.9: Plasmon responses of Pb(111) films are strongly affected by the interband excitations. This energy shift of the low energy excitation is attributed to the strong coupling between the two interface plasmons.

Chapter 6

Outlook: Quantum Plasmonics

Quantum plasmonics is an emerging field which focuses on light-matter interactions at the nano-scale. It includes studies of novel plasmon resonances in coupled nanostructures, *i.e.*, in nano objects that are within very close proximity of one another. This has led to the emergence of, *e.g.*, charge transfer plasmons [104, 106], quantum plasmonic tunneling, [23], and nonlocal screening in nano-particle dimers [105, 86, 85]. In order to improve the performance of plasmonic devices (*e.g.*, plasmon energy, lifetime, damping, propagation length, and Q-factor), a deep understanding of the fundamental physics involved in plasmon excitation in quantum confined systems is crucial [83, 70].

Our research identified for the first time that quantum size effects can lead to significant shifts in the energy and dispersion of the (monopole) surface plasmon of atomically-smooth metallic nano-films. Moreover, our study suggests that multipole surface plasmons can be enhanced by quantum size effects. The rationalization behind these findings is the correlation between dynamical surface screening and the ground state charge density profile at the surface. A robust multipole plasmon, which in contrast to the monopole surface plasmon, couples directly with light, could then be used in nano-photonics or detector applications [94, 93].

On the other hand, the strong coupling between the surface and interface plasmons in Pb(111) films, which is probably due to the quasi one-dimensional nature of the screening response in these films, is quite relevant for the tunability of plasmonic parameters such as the damping and propagation length. Specifically, the symmetric plasmon can be tuned over a wide range of frequencies. In conventional plasmonics this is normally done in the retarded limit (near the light line), but the problem with this is that modes close to the light line suffer from heavy radiation losses [15]. Thus, transmission lines exploiting the symmetric modes are expected to have a longer propagation distance. Similarily, resonators would have larger Q-factors [94]. Another important feature of the symmetric slab plasmon is the easy geometric (via the slab thickness L) tunability of the dispersion. The latter depends on q*L, rather than on q. This is similar to the trick employed by several groups (de Abajo group[4], Halas-Nordlander group[73], El-Sayed group [35]). In the Mie-resonance community, it has been known that it is difficult to tune the Mie resonance of simple (*e.g.* spherical) nanoparticles by changing their size, unless one works in the retarded domain, *i.e.*, close to the light line[12, 76]. However, as mentioned above, this would lead to heavy radiation losses. Note that small particles produce large q-vectors, meaning that one quickly approaches the saturated, non-retarded part of the plasmon dispersion, *i.e.* fixed frequency. To overcome this problem, researchers developed core-shell nanoparticles, which are easily tunable by the particle size and shell thickness, *e.g.*, [73]. This made naonparticle plasmonics applicable to a whole range of applications, including cancer diagnostics and treatment [19].

It would be very exciting to sandwich a Pb(111) film between graphene layers [*]. Both materials support gapless plasmons [69], and the resonance energy of the Pb may be tuned to overlap with that of graphene. Interesting cross-dimensional effects (2D vs 3D) could be observed, with strong quantum effects possibly playing an important role. In fact, it might be possible to affect the superconductivity of the Pb film where the symmetric mode plasmon would serve as the boson glue for Cooper

[*]K. Kempa, private communication.

pairing [†]. Furthermore, it would be very exciting to sandwich Pb between topological insulator films. Topological insulators support so-called spin-plasmons or collective spin-charge fluctuations. In addition to all the effects expected from a graphene-Pb sandwich, one could affect the superconductivity of Pb through the magnetic (spin) component [‡].

In conclusion, we explored the fundamental physics of plasmon oscillations in the quantum size (*i.e.*, extreme nanoscale) regime. The new insights gleaned from this study are therefore likely to open a new avenue for tuning plasmon resonances in nano-plasmonics - which in turn is finding its way into nano-photonics, nano-electronics, solar energy conversion, surface enhanced Raman scattering, single molecule detection, biological and medical applications.

[†]K. Kempa, private communication.
[‡]K. Kempa, private communication.

Bibliography

[1] Aballe, L., Barinov, A., Locatelli, A., Heun, S., and Kiskinova, M. (2004). Tuning surface reactivity via electron quantum confinement. *Phys. Rev. Lett.*, 93:196103. xiv, 59, 69, 70

[2] Aballe, L., Rogero, C., and Horn, K. (2002a). Quantum size effects in ultrathin epitaxial Mg films on Si(111). *Phys. Rev. B*, 65:125319. 9, 53, 60, 64, 71

[3] Aballe, L., Rogero, C., and Horn, K. (2002b). Quantum-size effects in ultrathin Mg films: electronic structure and collective excitations. *Surf. Sci.*, 518:141. xiv, 69, 70, 71

[4] Aizpurua, J., Hanarp, P., Sutherland, D. S., Käll, M., Bryant, G. G., and de Abajo, F. J. G. (2003). Optical properties of gold nanorings. *Phys. Rev. Lett.*, 90:057401. 90

[5] Anderson, K., Jacobsen, K. W., and Thygesen, K. S. (2012). Spatially resolved quantum plasmon modes in metallic nano-films from first-principles. *Phys. Rev. B*, 86:245129. 31

[6] Anderson, O. K. (1975). Linear methods in band theory. *Phys. Rev. B*, 12:3060. 39

[7] Argile, C. and Rhead, G. E. (1989). Adsorbed layer and thin film growth modes monitored by Auger electron spectroscopy. *Surf. Sci. Rep.*, 10:277. 54

[8] Ashcroft, N. W. and Mermin, N. D. (1976). *Solid State Physics*. Holt, Rinehart and Winston. 4

[9] Bao, X. Y., Zhang, Y. F., Wang, Y., Jia, J. F., Xue, Q. K., Xie, X. C., and Zhao, Z. X. (2005). Quantum size effects on the perpendicular upper critical field in ultrathin lead films. *Phys. Rev. Lett.*, 95:247005. 9

[10] Bennett, A. J. (1970). Influence of the electron charge distribution on surface-plasmon dispersion. *Phys. Rev. B*, 1:203. xi, 18, 19

[11] Benson, O. (2011). Assembly of hybrid photonic architectures from nanophotonic constituents. *Nature*, 480:193. x, 3

[12] Berciaud, S., Cognet, L., Tamarat, P., and Lounis, B. (2005). Observation of intrinsic size effects in the optical response of individual gold nanoparticles. *Nano Lett.*, 5:515. 90

[13] Binggeli, N. and Altarelli, M. (2006). Surface reactivity and quantum-size effects on the electronic density decay length of ultrathin metal films. *Phys. Rev. Lett.*, 96:036805. xiv, 59, 69, 70, 71, 72

[14] Bozhevolnyi, S. I., Volkov, V. S., Devaux, E., Laluet, J. Y., and Ebbesen, T. W. (2006). Channel plasmon subwavelength waveguide components including interferometers and ring resonators. *Nature*, 440:508. 4

[15] Burke, J. J., Stegeman, G. I., and Tamir, T. (1986). Surface-polariton-like waves guided by thin, lossy metal films. *Phys. Rev. B*, 33:5187. 6, 90

[16] Calvayrac, F., El-Gammal, S., Kohl, C., Reinhard, P. G., and Suraud, E. (1997). Nonlinear dynamics of nuclei and metal clusters. *Il Nuovo Cimento*, 110 A:9–10. 5

[17] Chan, T. L., Wang, C. Z., Hupalo, M., Tringides, M., and Ho, K. M. (2006). Quantum size effect on the diffusion barriers and growth morphology of Pb/Si(111). *Phys. Rev. Lett.*, 96:226102. 10

[18] Chiarello, G., Formoso, V., Santaniello, A., Colavita, E., and Papagno, L. (2000). Surface-plasmon dispersion and multipole surface plasmons in Al(111). *Phys. Rev. B*, 62:12676. 68

[19] Choi, M. R., Stanton-Maxey, K. J., Stanley, J. K., Levin, C. S., Bardhan, R., Akin, D., Badve, S., Sturgis, J., Robinson, J. P., Bashir, R., Halas, N. J., and Clare, S. E. (2007). A cellular trojan horse for delivery of therapeutic nanoparticles into tumors. *Nano Lett.*, 7:3759. 90

[20] Dionne, J. A., Sweatlock, L. A., Atwater, H. A., and Polman, A. (2005). Planar metal plasmon waveguides: frequency-dependent dispersion, propagation, localization, and loss beyond the free electron model. *Phys. Rev. B*, 72:075405. 86

[21] Drude, P. (1900). Zur Elektronentheorie dier Metalle; II. Teil. galvanomagnetische und thermomagnetische Effecte. *Annalen der Physik*, 308:369. 16

[22] Eguiluz, A. G., Ying, S., and Quinn, J. (1975). Influence of the electron density profile on surface plasmons in a hydrodynamic model. *Phys. Rev. B*, 11:2118. 19

[23] Esteban, R., Borisov, A., Nordlander, P., and Aizpurua, J. (2011). Bridging quantum and classical plasmonics with a quantum-corrected model. *Nature Communications*, 3:825. 89

[24] Feibelman, P. J. (1975). Microscopic calculation of electromagnetic fields in refraction at a jellium-vacuum interface. *Phys. Rev. B.*, 12:1319. 4, 29, 68, 73

[25] Feibelman, P. J. (1982). Surface electromagnetic fields. *Prog. Surf. Sci.*, 12:287. 30, 34, 68

[26] Gadzuk, J. W. (1970). Coupled surface-plasmon modes in metal-thin-film-vacuum sandwiches. *Phys. Rev. B*, 1:1267. 34, 80

[27] Grill, L. and Feichtinger, H. (2003). Image-potential resonances studied by selective electron scattering in thin Pb(111) films and clusters on Ge(111). *Surf. Sci.*, 537:84–94. 54

[28] Guo, Y., Zhang, Y. F., Bao, X. Y., Han, T. Z., Tang, Z., Zhang, L. X., Zhu, W. G., Wang, E. G., Niu, Q., Qiu, Z. Q., Jia, J. F., Zhao, Z. X., and Xue, Q. K. (2004). Superconductivity modulated by quantum size effects. *Science*, 306:1915. 9

[29] Hohenberg, P. and Kohn, W. (1964). Inhomogeneous electron gas. *Phys. Rev.*, 136:B864. 23

[30] Hong, H., Wei, C. M., Chou, M. Y., Wu, Z., Basile, L., Chen, H., Holt, M., and Chiang, T. C. (2003). Alternating layer and island growth of Pb on Si by spontaneous quantum phase separation. *Phys. Rev. Lett.*, 90:076104. 9

[31] Ibach, H. (1977). *Electron Spectroscopy for Surface Analysis*. Springer Verlag. 52, 57, 58

[32] Ibach, H. and Mills, D. L. (1982). *Electron Energy Loss Spectroscopy and Surface Vibrations*. Academic Press. 41, 43, 44

[33] Imbusch, A. and Niedrig, H. (1970). Temperature effect on energy loss spectrum of fast electrons in aluminium and lead foils between 3 K and 295 K. *Phys. Lett.*, 32A:375. 10

[34] Inaoka, T., Nagao, T., Hasegawa, S., Hildebrandt, T., and Henzler, M. (2002). Two-dimensional plasmon in a metallic monolayer on a semiconductor surface: Exchange-correlation effects. *Phys. Rev. B*, 66:245320. 9

[35] Jain, P. K., Lee, K. S., El-Sayed, I. H., and El-Sayed, M. A. (2006). Calculated absorption and scattering properties of gold nanoparticles of different size, shape, and composition: Applications in biological imaging and biomedicine. *J. Phys. Chem. B*, 110:7238. 90

[36] Jalochowski, M. and Bauer, E. (1988). Quantum size and surface effects in the electrical resistivity and high-energy electron reflectivity of ultrathin lead films. *Phys. Rev. B*, 38:5272. 9

[37] Jia, Y., Wu, B., Li, C., Einstein, T. L., Weitering, H. H., and Zhang, Z. (2010). Strong quantum size effects in Pb(111) thin films mediated by anomalous Friedel oscillations. *Phys. Rev. Lett.*, 105:066101. 10, 11, 76, 77, 87

[38] Kempa, K., Liebsch, A., and Schaich, W. L. (1988). Comparison of calculations of dynamical screening at jellium surface. *Phys. Rev. B*, 38:12645. 4

[39] Kempa, K. and Schaich, W. L. (1986). Calculation of corrections to Fresnel optics from density response. *Phys. Rev. B*, 34:547–557. 64

[40] Kempa, K. and Schaich, W. L. (1988). Nonlocal corrections to Fresnel optics: Model calculations from first principles for flat jellium. *Phys. Rev. B*, 37:6711. 73

[41] Kempa, K. and Schaich, W. L. (1989). Nonlocal corrections to Fresnel optics: Jellium-model calculations above the bulk-plasmon threshold. *Phys. Rev. B*, 39:13139. 73

[42] Kim, J., Qin, S., Yao, W., Niu, Q., Chou, M. Y., and Shih, C. K. (2010). Quantum size effects on the work function of metallic thin film nanostructures. *Proc. Natl. Acad. Sci.*, 107:12761. 9

[43] Kittel, C. (2004). *Introduction to Solid State Physics*. Wiley. 1, 2, 19

[44] Kozhevnikov, A. V., Eguiluz, A. G., and Schulthess, T. C. (2010). Towards first-principles electronic structure simulations of excited states and strong correlations in nano- and materials science. *Supercomputing10, Proceedings of the 2010 ACM/IEEE International Conference for High Performance Computing, Networking, Storage and Analysis*, pages 1–10. 39, 40

[45] Kunz, C. (1966). Messung charkateristischer Energieverluste von Elektronen an leichtoxydierbaren Metallen im Ultrahochvakuum. *Zeitschrift für Physik*, 196:311. xi, 18

[46] Lang, N. D. and Kohn, W. (1970). Theory of metal surfaces: Charge density and surface energy. *Phys. Rev. B*, 1:4555. 72

[47] Lang, N. D. and Kohn, W. (1971). Theory of metal surfaces: Work function. *Phys. Rev. B*, 3:1215. xii, 25, 26

[48] Li, H. and Tonner, B. P. (1988). A LEED study of the structure of epitaxial Pb/Ge(111) monolayers and ultrathin films. *Surf. Sci.*, 193:10–32. 54

[49] Li, J. and Ning, C. (2003). Interplay of collective excitations in quantum-well intersubband resonances. *Phys. Rev. Lett.*, 91:097401. 9

[50] Li, J. and Ning, C. (2004). Collective excitations in InAs quantum well intersubband transitions. *Physica E*, 22:628. 9

[51] Li, X., Teng, A., Özer, M. M., Shen, J., Weitering, H. H., and Zhang, Z. (2014). Plasmonic excitations in ultrathin metal films on dielectric substrates. *New J. Phys.*, 16:065014. 31

[52] Liebsch, A. (1987). Dynamic screening at simple-metal surfaces. *Phys. Rev. B*, 36:7378. xv, 64, 65, 71, 72, 73

[53] Liebsch, A. (1991). Electronic excitations in adsorbed alkali-metal layers. *Phys. Rev. Lett.*, 67:2858. 9, 65

[54] Liebsch, A. (1997). *Electronic Excitations at Metal Surfaces*. Plenum Press. xii, xiii, 26, 28, 30, 41, 42, 43, 44

[55] Liebsch, A., Kim, B., and Plummer, E. (2001). Collective excitations in adsorbed alkali-metal films: Critical analysis of photofield and electron-energy-loss spectra for K on Al(111). *Phys. Rev. B*, 63:125416. 9

[56] Lüth, H. (2010). *Solid Surfaces, Interfaces and Thin Films*. Springer Verlag. xiii, 50

[57] Ma, X., Jiang, P., Qi, Y., Jia, J., Yang, Y., Duan, W., Li, W. X., Bao, X., Zhang, S. B., and Xue, Q. K. (2007). Experimental observation of quantum oscillation of surface chemical reactivities. *Proc. Natl. Acad. Sci.*, 104:9204–9208. 9

[58] Nagao, T., Hildebrandt, T., Henzler, M., and Hasegawa, S. (2001). Dispersion and damping of a two-dimensional plasmon in a metallic surface-state band. *Phys. Rev. Lett.*, 86:5747. 9

[59] Ozbay, E. (2006). Plasmonics: Merging photonics and electronics at nanoscale dimensions. *Science*, 311:189. 4

[60] Özer, M., Wang, C., Zhang, Z., and Weitering, H. (2009). Quantum size effects in the growth, coarsening, and properties of ultra-thin metal films and related nanostructures. *J. Low Temp. Phys.*, 157:221. 10, 76

[61] Özer, M. M., Moon, E. J., Eguiluz, A. G., and Weitering, H. H. (2011). Plasmon response of a quantum-confined elecron gas probed by core-level photoemission. *Phys. Rev. Lett.*, 106:197601. 53, 60, 61

[62] Özer, M. M. and Weitering, H. H. (2013). Formation of atomically smooth epitaxial metal films on a chemically reactive interface: Mg on Si(111). *Phys. Rev. B*, 88:045415. 53, 60, 61

[63] Paggel, J. J., Wei, C. M., Chou, M. Y., Luh, D. A., Miller, T., and Chiang, T. C. (2002). Atomic-layer-resolved quantum oscillations in the work function: Theory and experiment for Ag/Fe(100). *Phys. Rev. B*, 66:233403. 9

[64] Pakizeh, T. (2011). Optical absorption of plasmonic nanoparticles in presence of a local interband transition. *J. Phys. Chem. C*, 115:21826. 84

[65] Parkin, S. S. P., More, N., and Roche, K. P. (1990). Oscillations in exchange coupling and magnetoresistance in metallic superlattice structures: Co/Ru, Co/Cr, and Fe/Cr. *Phys. Rev. Lett.*, 64:2304–2307. 9

[66] Perdew, J. P., Burke, K., and Ernzerhof, M. (1996). Generalized gradient approximation made simple. *Phys. Rev. Lett.*, 77:3865. 24, 39

[67] Pines, D. and Bohm, D. (1952). A collective description of electron interactions: II. collective *vs* individual particle aspects of the interactions. *Phys. Rev.*, 85:338. 1, 20

[68] Pirzadeh, Z., Pakizeh, T., Miljkovic, V., Langhammer, C., and Dmitriev, A. (2014). Plasmon-interband coupling in nickel nanoantennas. *ACS Photonics*, 1:158. 84

[69] Polini, M., Asgari, R., Borghi, G., Barlas, Y., Pereg-Barnea, T., and MacDonald, A. H. (2008). Plasmons and the spectral function of graphene. *Phys. Rev. B*, 77:181411(R). 90

[70] Politano, A. and Chiarello, G. (2014). Plasmonic modes in thin films: quo vadis? *Front. Mater.*, 1:9. 89

[71] Polman, A. and Atwater, H. A. (2005). Plasmonics: optics at the nanoscale. *Materials Today*, 8:56. 5

[72] Powell, C. J. and Swan, J. B. (1959). Electron energy loss measurement on Mg thin film. *Phys. Rev.*, 116:81. x, 2

[73] Prodan, E., Radloff, C., Halas, N. J., and Nordlander, P. (2003). A Hybridization model for the plasmon response of complex nanostructures. *Science*, 302:419. 90

[74] Raether, H. (1980). *Excitation of Plasmons and Interband Transitions by Electrons*. Springer-Verlag. 4, 22, 80, 81

[75] Raether, H. (1988). *Surface Plasmons on Smooth and Rough Surfaces and on Gratings*. Springer-Verlag. 4

[76] Ringe, E., Langille, M. R., Sohn, K., Zhang, J., Huang, J., Mirkin, C. A., Van Duyne, R. P., and Marks, L. D. (2012). Plasmon length: A universal parameter to describe size effects in gold nanoparticles. *J. Phys. Chem. Lett.*, 3:1479. 90

[77] Ritchie, R. H. (1957). Plasmon losses by fast electron in thin films. *Phys. Rev.*, 106:874. 1, 20

[78] Rizzi, A. (1997). Electron energy loss spectroscopy and its application in material science. *Fresenius J. Anal. Chem.*, 358:15. 41, 42

[79] Schwartz, C. and Schaich, W. L. (1982). Hydrodynamic models of surface plasmons. *Phys. Rev. B*, 26:7008. 19

[80] Singh, D. and Nordström, L. (2006). *Planewaves, Pseudopotentials and the LAPW Method*. Springer Verlag. xii, 35, 37, 38, 39

[81] Smith, A. R., Chao, K. J., Niu, Q., and Shih, C. K. (1996). Formation of atomically flat silver films on GaAs with a "silver mean" quasi periodicity. *Science*, 273:226. 9

[82] Sprunger, P. T., Watson, G. M., and Plummer, E. W. (1992). The normal modes at the surface of Li and Mg. *Surf. Sci.*, 269/270:551. xiv, 10, 63, 64, 68, 70

[83] Tame, M. S., McEnery, K. R., Özdemir, S. K., Lee, J., Maier, S. A., and Kim, M. S. (2013). Quantum plasmonics. *Nature Physics*, 9:329. 89

[84] Tang, S. J., Lee, C. Y., Huang, C. C., Chang, T. R., Cheng, C. M., Tsuei, K. D., Jeng, H. T., Yeh, V., and Chiang, T. C. (2011). Polarizability of a 2-dimensional electron gas. *Phys. Rev. Lett.*, 107:066802. xiii, 54, 55

[85] Teperik, T. V., Nordlander, P., Aizpurua, J., and Borisov, A. G. (2013a). Quantum effects and nonlocality in strongly coupled plasmonic nanowire dimers. *Optics Express*, 21:27306. 89

[86] Teperik, T. V., Nordlander, P., Aizpurua, J., and Borisov, A. G. (2013b). Robust subnanometric plasmon ruler by rescaling of the nonlocal optical response. *Phys. Rev. Lett.*, 110:263901. 89

[87] Tonks, L. and Langmuir, I. (1929). Oscillations in ionized gases. *Phys. Rev.*, 33:195. 1

[88] Tsuei, K. D., Heskett, D., Baddorf, A. P., and Plummer, E. W. (1991). Electron loss spectra from thin alkali films on Al(111). *J. Vac. Sci. Technol. A*, 9:1761. 9

[89] Tsuei, K. D., Plummer, E. W., and Feibelman, P. J. (1989). Surface-plasmon dispersion in simple metals. *Phys. Rev. Lett.*, 63:2256. xii, 20, 30, 68

[90] Tsuei, K. D., Plummer, E. W., Liebsch, A., Kempa, K., and Bakshi, P. (1990). Multipole plasmon modes at a metal surface. *Phys. Rev. Lett.*, 64:44. 20, 64, 65

[91] Ullrich, C. A. and Vignale, G. (2001). Theory of the linewidth of intersubband plasmons in quantum wells. *Phys. Rev. Lett.*, 87:037402. 9

[92] Wachowics, E. and Kiejna, A. (2001). Bulk and surface properties of hexagonal-close-packed Be and Mg. *J. Phys.: Condens. Matter.,*, 13:10767. xi, 6, 8

[93] Wang, W., Apell, P., and Kinaret, J. (2011a). Edge plasmons in graphene nanostructures. *Phys. Rev. B*, 84:085423. 89

[94] Wang, Y., Plummer, E. W., and Kempa, K. (2011b). Foundations of plasmonics. *Advances in Physics*, 60:799. 5, 6, 89, 90

[95] Wei, C.-M. and Chou, M.-Y. (2002). Theory of quantum size effects in thin Pb(111) films. *Phys. Rev. B*, 66:233408. 10

[96] Werner, W. S. M., Glantschnig, K., and Ambrosch-Draxl, C. (2009). Optical constants and inelastic electron-scattering data for 17 elemental metals. *J. Phys. Chem. Ref. Data*, 38:1013. 10

[97] Williams, J. B., Sherwin, M. S., Maranowski, K. D., and Gossard, A. C. (2001). Dissipation of intersubband plasmons in wide quantum wells. *Phys. Rev. Lett.*, 87:037401. 9

[98] Wolf, G. V. and Fedorov, D. V. (2001). The self-consistent response of the electron density of a crystal copper film to an external electrostatic field. *Physics of the Solid State*, 43:401. 41

[99] Yeh, V., Berbil-Bautista, L., Wang, C.-Z., Ho, K.-M., and Tringides, M. C. (2000). Role of the metal/semiconductor interface in quantum size effects: Pb/Si(111). *Phys. Rev. Lett.*, 85:5158–5161. 10

[100] Yu, Y., Jiang, Y., Tang, Z., Guo, Q., Jia, J., Xue, Q., Wu, K., and Wang, E. (2005). Thickness dependence of surface plasmon damping and dispersion in ultrathin Ag films. *Phys. Rev. B*, 72:205405. 66

[101] Yuan, Z. and Gao, S. (2006). Linear-response study of plasmon excitation in metalic thin films: Layer-dependent hybridization and dispersionl. *Phys. Rev. B*, 73:155411. xii, 31, 32, 33

[102] Yuan, Z., Jiang, Y., Gao, Y., Käll, M., and Gao, S. (2011). Symmetry-dependent screening of surface plasmons in ultrathin supported films: The case of Al/Si(111). *Phys. Rev. B*, 83:165452. xii, 31, 34, 35, 66, 68

[103] Zhang, Z. Y., Niu, Q., and Shih, C. K. (1998). "electronic growth" of metallic overlayers on semiconductor substrates. *Phys. Rev. Lett.*, 80:5381. 9

[104] Zuloaga, J., Prodan, E., and Nordlander, P. (2009). Quantum description of the plasmon resonances of a nanoparticle dimer. *Nano Lett.*, 9:887. 89

[105] Zuloaga, J., Prodan, E., and Nordlander, P. (2010). Quantum plasmonics: Optical properties and tunability of metallic nanorods. *ACS NANO*, 4:5269. 89

[106] Zuloaga, J., Prodan, E., and Nordlander, P. (2012). Quantum plasmonics: Nonlinear effects in the field enhancement of a plasmonic nanoparticle dimer. *Nano Lett.*, 12:1333. 89

Vita

Ao Teng was born in Xuzhou, Jiangsu, China on September 29, 1985, to Daohong Teng and Yuying Diao. He graduated from Xuzhou No.1 Middle School in 2004. Four years later, he received a Bachelors degree in Applied Physics from Nanjing University of Aeronautics and Astronautics, Nanjing, Jiangsu, China. He moved to The University of Tennessee in the same year and started his doctoral research in 2009. During the early stage of the program, he performed epitaxial Ru film growth and characterization under the supervision of Dr. Paul Snijders at Oak Ridge National Laboratory. Subsequently, he studied plasmons in quantum confined metal films. He expects to graduate with a Doctorate of Philosophy degree in Physics in August of 2014.